POLITECNICO DI TORINO

Master's Degree in Environmental and Land Engineering
CLIMATE CHANGE

Master's Degree Thesis

Bathymetry estimation of a shallow proglacial lake through UAV imagery and a geospatial regression method

Supervisors

Prof.ssa Stefania TAMEA

Prof. Carlo CAMPOREALE

Candidate

Valeria LONGHI

October 2023

Abstract

Proglacial areas are one of the most rapidly changing ecosystems due to glacier and permafrost degradation. To better understand these environments and their dynamics, bathymetric mapping is a necessary step in hydraulic modelling. This is essential for assessing water quality, sediment and pollutant movement, and evaluating habitats. This thesis aims to evaluate the effectiveness of a geographically weighted regression (GWR) model, which can capture a spatially heterogeneous relationship between inputs and an output, to retrieve bathymetry of a shallow proglacial lake, whose water depth is less than about 1 m, from RGB and multispectral imagery. The case study is a system of proglacial channelized streams joining in a shallow lake originating from the melting of the Rutor alpine glacier, in Valle d'Aosta. Field experiments were carried out during summer 2021 and 2023 for GNSS positioning along different sections of the streams and simultaneously for acquiring photogrammetric data with digital numbers (DN) using an uncrewed aerial vehicle (UAV). The digital cameras mounted on the UAV were RGB and multispectral sensors respectively for 2021's and 2023's survey. Water depth along the surveyed sections was retrieved from the measured points and the Digital Elevation Model (DEM) generated from the UAV imagery. After obtaining the orthomosaic of the area, spectral band ratios were computed and, through the principal component analysis (PCA), were selected as an optimal input of the GWR model. For 2021's model inputs, $\ln(DN_B/DN_R)$ and $\ln(DN_G/DN_B)$ were selected, while for 2023's one, $\ln(DN_{NIR}/DN_G)$ and $\ln(DN_G/DN_B)$. Results showed that the GWR models based on a single band ratio input led to a discrepancy between estimation and observation, especially for 2021's dataset. In contrast, considering both PCA-selected band ratios, the GWR models showed improved performances, as R^2 increased from 0.47 to 0.77 for the 2021 dataset, and from 0.90 to 0.94 for the 2023 dataset. Moreover, the 2023 bathymetry reconstruction was more accurate than the 2021 reconstruction, likely due to the larger dataset of water depth observations and the use of multispectral UAV acquisition. Multispectral data more effectively modelled the effect of spatial heterogeneous bottom types, caused by submerged vegetation and sediment.

Table of Contents

1. Introduction

In the context of global warming, mountainous regions serve as crucial climate indicators. Consequently, there is a growing urgency to characterize and comprehend the dynamics of these environments. This becomes particularly pertinent in the Alpine region, where the increase in average air temperatures has more than doubled the global average temperature rise. Rapid glacier and ice sheet retreat impact sediment supply, affecting nutrient cycling, carbon flux, and resource management.

To gain a deeper understanding of these dynamic mountain environments, bathymetric mapping assumes a pivotal role within hydraulic modelling. This process is crucial for assessing various aspects, including water quality, sediment and pollutant transport, and habitat evaluation.

Traditionally, accurate bathymetric data for river modelling have been collected through methods such as total stations, GPR, and echosounders. However, these conventional approaches can be time-consuming, costly, or unfeasible for large or inaccessible areas such as proglacial areas (Monteys et al., 2015). Bathymetric Light Detection and Ranging (LiDAR) systems offer quicker topography data collection but require specialized processing algorithms and clear water conditions. Recently, remote sensing techniques using multispectral and hyperspectral imagery have gained popularity for reconstructing water depth in coastal and inland waters. Radiance observed by remote sensors can be separated into different components, and water depth estimation relies on accurate separation (Kim et al., 2019). In rivers, where shallow water leads to significant bottom-reflected radiance conventional methods assuming a constant relationship between water depth and radiance encounter challenges due to varying bottom types. This complexity arises from diverse bed materials like sediments, vegetation, and periphyton. Global inversion models struggle in such heterogeneous environments (Su et al., 2014).

To address these limitations, a geographically weighted regression (GWR) model is proposed. This approach takes into account local factors in determining the linear regression coefficients considering the geographic context of each location. This technique captures the spatially varying response of radiance to water depth, accommodating the heterogeneity of substrates in rivers (Vinayaraj et al, 2016): GWR has shown success in mapping near-shore bathymetry from multispectral imagery, but its application in stream environments is less explored.

This thesis aims to assess the effectiveness of a GWR model in estimating the bathymetry of a network of channelized streams flowing into Marginale Lake, a shallow proglacial lake situated in the vicinity of the Rutor glacier in the Italian Alps. The water depth in this context typically reaches approximately 1 meter, and the estimation process leverages geomatic and hydrological data collected over two years (2021 and 2023).

While glaciers have been extensively studied, until now, few studies have focused on proglacial areas. However, the modelling of potential future lake' dynamics in mountain areas, once the glacier melted, holds significant importance, especially concerning natural hazards, associated risks, and the socio-economic dimensions linked to proglacial lake formation (Heckmann et al., 2019).

The thesis was conducted in collaboration with the Climate Change Glacier Lab[1]. Its structure is as follows. An initial section provides a review of the theoretical framework behind proglacial environment monitoring using geomatics and bathymetry inversion models. Then, the study site, Marginale Lake, is introduced. The following section delineates the methodology employed to retrieve the lake's bathymetry. Finally, the application of the method is illustrated. The thesis concludes with a discussion of the main findings, limitations, and suggestions for future improvements.

[1] Of DIATI department of Politecnico di Torino

2. Glacial and Proglacial Environments

2.1 Glacial Environments and Climate Change

Mountain regions are both sensitive to and disproportionally affected by recent climate change (Heckmann et al., 2019). One of the most significant and visible changes is glacier retreat. This process exposes formerly glaciated terrain to open air, triggering consequences for hydrological, geomorphic, and ecological systems. The geomorphic response to deglaciation has been categorized as paraglacial geomorphology (Heckmann et al., 2019), a branch of geomorphology concerned with the evolution of landscapes in high latitudes and altitudes. It deals with the role of water in the solid state in landscape evolution and through geotechnical and hydrological aspects related to water resource scarcity and environmental change (Dixon, 2016).

This chapter proposes a description of the features of these specific environments, starting from the glaciers from which they originate.

2.1.1 Glaciers

Glaciers are formed over many years, and even if they may appear static they are always mobile masses. Their motion is driven by gravitational forces and weight, occasionally sliding over water or sediment layers. This movement sculpts surroundings, glaciated valleys being one of the most characteristic examples. Glacier retreat yields another characteristic environment, as they leave sediment and reshape their form, leaving clear traces of their prior dimensions.

Glaciers are found across continents that have emerged from Earth's crust. In Europe, they dominate high mountain areas with favourable snow accumulation conditions. Alpine glaciers vary widely in size, spanning from small areas to extensive expanses over mountain peaks. Their size significantly influences responses to changing masses over time.

Glacier formation begins in the 'accumulation area,' where snow accumulation is greater than melt. Snow undergoes metamorphosis either through melting and refreezing, through the pressure and compaction of the overlying snow, becoming firn and then ice, increasing the overall mass of the glacier. Driven by increasing weight, the glacier flows toward the 'ablation area,' where part of its mass thaws and evaporates. An 'equilibrium line' marks the balance between melting and snowfall, separating these zones. Stable temperatures maintain glacier shape and size stability. Glacier equilibrium remains dynamic. Wind and avalanches alter snow distribution, impacting thawing or accumulation. Continuous snow mass movement leads to diverse features. Sliding forces generate crevasses, and where they intersect, seracs form. Moving ice collects debris, forming visible dark lines on its surface, known as

moraines. Melting snow forms supraglacial lakes and moulins, vertical fractures created by meltwater (Macelloni, 2022).

2.1.2 Proglacial Areas

Before describing the characteristics of proglacial environments, some clarifications about terminology are needed. Here the taxonomy proposed by Slaymaker (2009, 2011) - proglacial, periglacial and paraglacial - is adopted. “Proglacial” refers to an area, while “periglacial” refers to a process: a geomorphic process driven by frost. Finally, “paraglacial” addresses the specific morphodynamics (including their development over time) within a deglaciated landscape, encompassing spatial and temporal changes in the activity of geomorphic processes, slope instability, and the accumulation and erosion of sediment storage landforms.

Proglacial areas usually refer to areas deglaciated since the peak of the Little Ice Age (LIA) and now adjacent to the terminus of the present glacier. Comparisons with present-day glacier extents show that the distance by which many glaciers have retreated since the end of the LIA is in the order of 10^2 to 10^3 m, and the area deglaciated is in the order of 10^3 to 10^6 m^2 (Heckmann et al., 2019).

These areas are of particular interest to researchers and geographers because they provide valuable insights into the interactions between glaciers, climate, and the environment.

Proglacial environments undergo rapid and dynamic changes as glaciers retreat. As the ice melts, it exposes the land that was once covered by ice, revealing a complex landscape shaped by glacial activity. Transitional nature is a key characteristic of proglacial environments. Thus, they are considered to be in a state of transition, moving from glacial to non-glacial conditions, as Johnson (2002) noted. Alternatively, they are seen as shifting from an unstable or metastable state, which arises during deglaciation, toward establishing a new equilibrium under periglacial or non-glacial conditions, as discussed by Slaymaker (2011). In fact, the "close to the ice front" area of a glacier, known as the proglacial zone, is challenging to define accurately in the field today. Due to the rapid melting of glaciers, the position of the glacier snout can shift significantly from year to year, up to tens of meters. This continuous movement disrupts the previously established equilibrium between sediment delivery from the glacier and fluvial reworking (Slaymaker 2011; Heckmann et al., 2019). Where this equilibrium exists, it is highly dynamic.

One of the features of proglacial areas is the deposition of glacial sediments. As the glacier retreats, it releases sediments it had previously carried. This can result in the formation of various landforms such as moraines, which are ridges of debris left along the sides of the glacier's former path. These landforms provide evidence of the glacier's past extent and help scientists reconstruct its history.

Proglacial areas also experience changes in hydrology. Periglacial processes of freezing-thawing-drying on an annual basis perturb the composition of groundwaters within the proglacial zone (Tranter et al., 2014). The melting ice contributes to the formation of meltwater streams, ponds, and lakes. These water bodies often contain fine sediment, and they play a crucial role in transporting and depositing sediment downstream. Additionally, the availability of meltwater can impact the local ecosystem, influencing plant growth, animal habitats, and even human activities.

Lakes are a distinctive element of glacial landscapes. They are located near current or historical glaciers and ice sheets, in high alpine cirques, inner-alpine valleys, and lowlands. The formation of proglacial lakes occurs as retreating glaciers reveal topographical depressions in bedrock or open spaces behind sediment dams, prompting the accumulation of water and sediment. Consequently, proglacial lakes serve as primary sediment repositories, interrupting the natural flow of sediment from elevated areas to lower regions.

In recent years, new lakes have developed in glacier forefields, and the size of numerous proglacial lakes has expanded across mountainous regions, attributed to the effects of climate-induced glacier melting. These lakes hold substantial societal significance in mountainous landscapes, encompassing aspects ranging from water supply and energy generation to issues of hazard, risk, and tourism. Certain proglacial lakes have garnered significant attention from the public and scientific communities due to catastrophic occurrences like lake outburst floods, as well as increased hazards and risks downstream. Recent studies focused on the modelling of potential future lakes in mountain areas, once the glacier melted, considering natural risks, and socio-economic dimensions (Otto, 2019; Heckmann et al., 2019).

The subject of this work is a system of proglacial channelized streams joining in a shallow lake. The channelled streams develop covering an alpine plateau and are fed by the Rutor glacier, and the formed lake is called Lago Marginale.

2.1.3 Cryosphere and Hydrosphere

To understand the role of glaciers and proglacial lakes and streams in the Earth's ecosystem, it’s important to define the cryosphere and hydrosphere.

The cryosphere and hydrosphere are two interconnected components of Earth's complex system, each playing a crucial role in shaping our planet's climate and supporting life.

The cryosphere encompasses all frozen water on Earth's surface, including snow, sea ice, ice caps, ice sheets, frozen lakes, rivers, and permafrost. It constitutes about 10% of the planet's surface and plays a vital role in Earth's climate dynamics and its overall water distribution. Modifications within the cryosphere are intricately linked to mountain ecosystems, which serve as sources of water for downstream agriculture,

hydropower generation, environments, and human consumption. The cryosphere is pivotal for both human activities and natural processes, contributing to the equilibrium of Earth's climate conditions (Macelloni, 2022).

The hydrosphere, on the other hand, consists of all the water on Earth's surface, including oceans, lakes, rivers, groundwater, and atmospheric water vapour. It is the largest component of the climate system (Kundzewicz, 2008). It is in constant motion, driven by various processes like evaporation, condensation, and precipitation. The hydrosphere plays a crucial role in regulating Earth's temperature through heat absorption and release, as well as in transporting heat around the planet through ocean currents.

The cryosphere and hydrosphere are closely linked through the water cycle. Water evaporates from the hydrosphere, forms clouds, and is then transported through the atmosphere. When it condenses, it falls as precipitation, which can accumulate as snow and ice in colder regions. As the climate changes, alterations in the cryosphere can disrupt the delicate water cycle balance, affecting regional water availability and weather patterns. Understanding these interactions is crucial for predicting and mitigating the effects of climate change and ensuring the sustainable management of Earth's water resources. The interaction between the cryosphere and hydrosphere is particularly important in terms of water availability, sea-level changes, and climate feedback mechanisms. Melting glaciers and ice sheets contribute to rising sea levels, impacting coastal areas and communities. Water stored in glaciers and snow cover also serves as a significant source of freshwater for many regions around the world. Changes in the cryosphere can influence ocean circulation patterns, which in turn affect climate patterns.

Thus, being mountainous and glacial environments among the most sensitive to the impact of climate change, they are studied as key indicators of climate variations.

2.1.4 Climate Change

In recent years, the rapid retreat of glaciers due to global warming has brought increased attention to proglacial areas. Researchers are closely monitoring these regions to document the shifts in landscape, hydrology, and ecosystems as glaciers continue to recede. Understanding proglacial environments is not only vital for advancing our knowledge of glacial processes but also for anticipating and mitigating the effects of climate change on various interconnected systems.

The cryosphere is experiencing continuous transformations, particularly in mountainous regions, and these shifts are set to persist at both local and global scales. Within mountainous contexts, alterations will stem not only from climate change but also from indirect factors that bear significant environmental and socio-economic implications. Glaciers serve as pivotal components within the water balance cycle of mountain landscapes and serve as sensitive indicators of climate change.

Changes in temperature and precipitation directly affect glacier dynamics and subsequently impact the proglacial landscape.

In general, each component of the cryosphere and hydrosphere assumes a distinct role within Earth's ecosystem, with each modification triggering repercussions across multiple domains. The thawing of ice sheets and glaciers contributes to rising sea levels and yields changes in marine ecosystems. Similarly, the melting of sea ice has the potential to reshape general ocean circulation patterns and the productivity and biodiversity of marine ecosystems. In terms of climate, the reduction of the reflective snow-white surface intensifies global warming by diminishing Earth's albedo and triggering ice-albedo feedback. The thawing and subsequent diminishment of permafrost disrupt the delicate equilibrium of the subsurface, altering the carbon cycle by releasing higher levels of methane into the atmosphere (IPCC, 2013, 2017).

The ongoing pattern of continuously increasing emissions of Greenhouse Gases (GHGs) and the subsequent rise in temperatures have led to an elevation of the equilibrium line (the line that separates the accumulation and ablation areas of a glacier) and a consistent decline in glacial masses. Projections from the Intergovernmental Panel on Climate Change (IPCC) highlight that the most substantial loss of snow mass is occurring in areas with smaller glaciers, such as the Alps, resulting in significant social and economic repercussions (Macelloni, 2022). Proglacial areas are one of the most rapidly changing natural earth surface systems due to glacier and ice sheet mass loss and permafrost degradation, all of which have become more evident over the last three decades (IPCC, 2019) and all of which are predicted to continue for many decades (Shannon et al., 2019; Carrivick e Tweed 2021).

In the European Alps, there has been an observed rise in air temperature of 0.3°C per decade on average (IPCC, 2018). This increase displays seasonal variability, with more pronounced upticks in summer and spring (Auer et al., 2007; Ceppi et al., 2012). This non-uniform pattern of fluctuation is also visible on a global scale across various elevations. Warming trends are generally accentuated above 500 meters above sea level (Wang et al., 2016a; Qixiang et al., 2018). In contrast, a uniform global trend is lacking for high elevations.

A continuous decline in the mountain cryosphere is evident, particularly in the European Alps. Since 1850, the ice area in the European Alps has diminished by 54%, and this trend is projected to persist. Projections suggest that, if this trend goes on, approximately 4-13% of the original ice area will remain by 2100 (Rasul et al., 2020). Over recent decades, the snow line has gradually risen, accompanied by a reduction in the number of snow cover days. The IPCC Fifth Assessment Report (AR5) predicts an 80% loss in the current mass of European glaciers (IPCC, 2014).

The maintenance of glacier equilibrium relies significantly on the presence of snow cover. It contributes to thermal regulation by reflecting heat and protecting the underlying ice, thereby shielding it from melting. Snowfall patterns exhibit high

sensitivity to climate change, and they are characterized by significant fluctuations over both years and decades. As the snow line shifts to higher elevations, liquid precipitation becomes more frequent at lower altitudes. This intensifies overall melting and triggers mechanisms linked to air temperature changes.

The whitish colour of snow and glacial regions plays a key role in the albedo effect, essential to Earth's energy balance. Surfaces with high albedo, such as snow-covered areas and ice sheets, reflect a large portion of incoming solar radiation back into space. In the context of snow and glaciers, the albedo effect is particularly crucial. Snow and ice have high albedo due to their bright, white surfaces. When sunlight hits these surfaces, much of it is reflected, preventing the underlying ice from warming up too quickly. However, as temperatures rise and snow melts, the exposed darker surfaces, like soil, rock or older and dark ice, have lower albedo and absorb more heat. Local surface temperatures can rise up to 2 degrees. This leads to further melting and a positive feedback loop – the more melting occurs, the more heat-absorbing surfaces are exposed, causing even more melting. Additionally, the deposition of dark particulate matter like dust and black carbon, caused by pollution and wind transport, exacerbates melting by diminishing the remaining snow's reflectivity. This accelerates the reduction of snow cover. These feedback loops also hold significance for permafrost in mountainous areas, as the carbon dioxide and methane contained within it could be released into the atmosphere consequently.

Glacier types exhibit varying responses to shifts in climate conditions. As temperatures rise, the Equilibrium Line Altitude (ELA) of a glacier – originally set at a certain elevation (ELA1) – moves higher (ELA2), as illustrated in Figure 2.1. This change results in increased melting of snow and a reduced accumulation area. Over time, glaciers adjust their ELA in ways specific to their types. Smaller glaciers often vanish entirely, while mountain glaciers thin out, and valley glaciers lose their tongues. For instance, glaciers characterized by gentle slopes and elongated tongues in valleys, found in places like Alaska, Canada, and the Alps, experience a gradual mass reduction in response to climate-driven shifts. This leads to substantial thinning of the glaciers, while their outward appearance remains largely unchanged despite significant mass losses. In contrast, smaller mountainous glaciers adapt quicker to climate changes, reshaping by expanding their ablation areas more rapidly (Vaughan, et al., 2013).

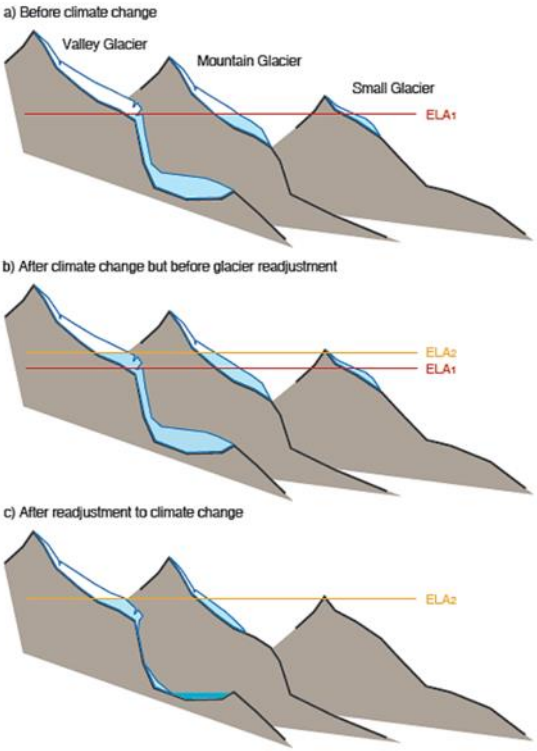

Figure 2.1 IPCC AR5, Schematic of three types of glaciers located at different elevations, and their response to an upward shift of the equilibrium line altitude (ELA).

In the European Alps, the retreat of alpine glaciers appears to have been influenced by the industrial revolution, rather than immediate climate change impacts that became evident later. The increase in black carbon soot played a pivotal role. Despite temperature rise and reduced precipitation, alpine glaciers experienced mass growth until around 1910. However, the late 1950s saw the onset of snow-covering dark particulate, diminishing albedo and accelerating snowmelt due to intensified solar radiation (Painter et al., 2013).

While climate models are currently examining shifts in snow cover, it's evident that heightened rainy precipitation in alpine regions, combined with an ongoing temperature increase, led to a 25% reduction in snow mass.

In the projections outlined by the IPCC, the expected reduction in snow cover ranges from 30% under RCP[2] 2.6 to potentially up to 80% under RCP 8.5 by the year 2100, as depicted in Figure 2.2

[2] RCP stands for Representative Concentration Pathways emission scenarios that IPCC defines as: "… used to assess the costs associated with emission reductions consistent with particular concentration pathways. The RCPs represent the range of GHG emissions in the wider literature well (Box 2.2, Figure 1); they include a stringent mitigation scenario (RCP2.6), two intermediate scenarios (RCP4.5 and RCP6.0), and one scenario with very high GHG emissions (RCP8.5)." (IPCC, 2014)

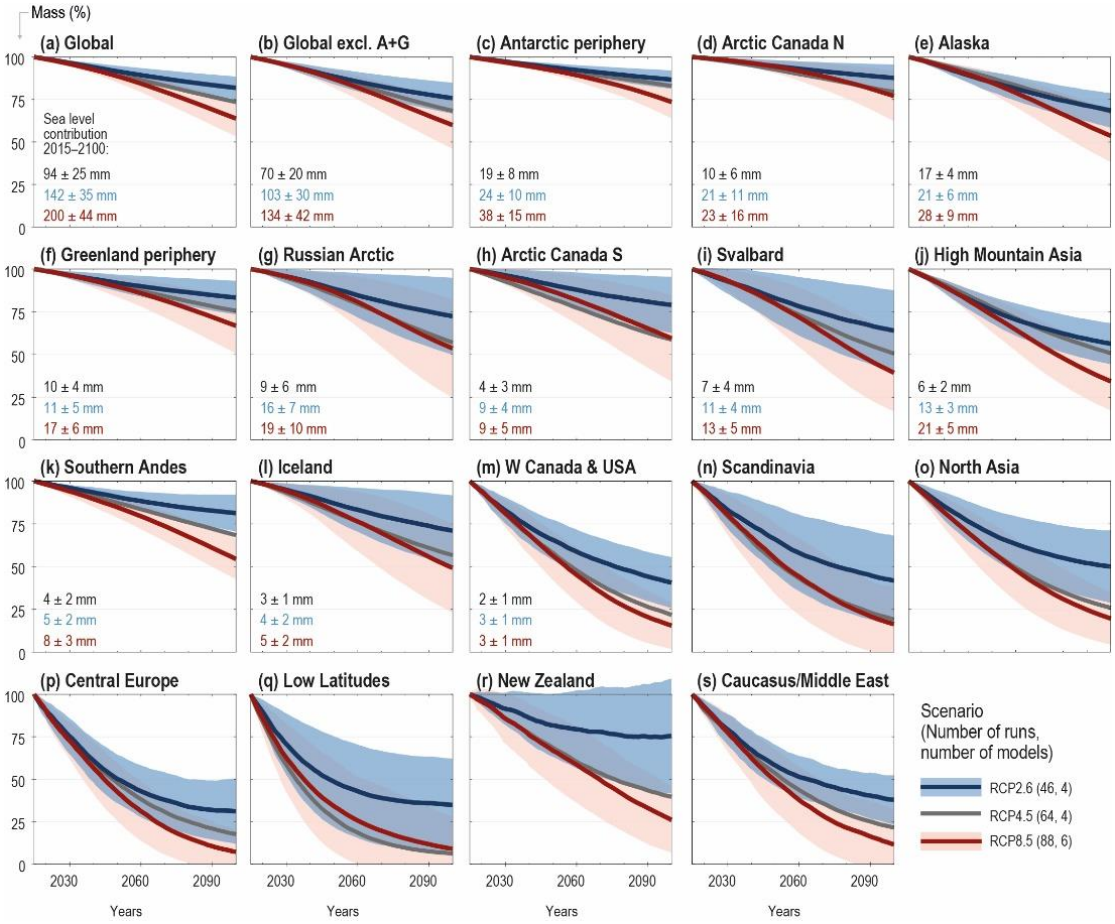

Figure 2.2 Projected glacier mass evolution between 2015 and 2100 relative to each region's glacier mass in 2015 (100%) based on three Representative Concentration Pathways (RCP) emission scenarios (IPCC,2022).

The global extent of glaciers encompasses approximately 250,000 km^2, spanning various regions around the world, except for Antarctica, the Greenland Region, and the Canadian and Russian Arctic. The evolution of glaciers primarily depends on the equilibrium between snow accumulation and ablation, while the glacier's response to temperature changes is influenced by factors like atmospheric warming, heightened longwave radiation, and shifts in air moisture. Atmospheric warming emerges as the primary catalyst for the widespread recession of glaciers, with human-driven increases in greenhouse gas emissions playing a significant role (Marzeion et al., 2014).

Empirical research demonstrates a strong likelihood of substantial ice mass loss across polar and high mountain regions, as indicated in Figure 2.3. The IPCC's projections for 2100 emphasize the most profound mass reductions in regions featuring smaller glaciers, such as the scenario observed in the European Alps. A similar concept also applies to the modification of permafrost mass, lake and river ice, and all ecosystems connected to them.

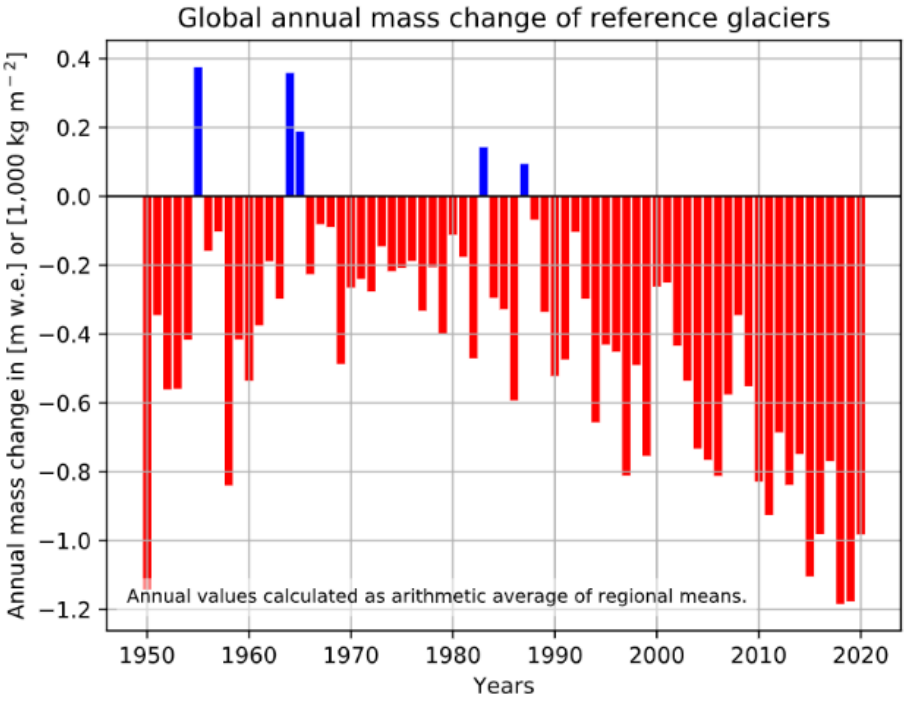

Figure 2.3 Annual mass balance of reference glaciers with more than 30 years of ongoing glaciological measurements. From the World Glacier Monitoring Service (WGMS).

2.1.5 Glacier-related Effects of Climate Change

Alterations in this equilibrium can give rise to numerous implications for delicate mountain ecosystems and the inhabitants residing within them. Glaciers, along with the broader cryosphere, regulate water reservoirs for over 600 million individuals globally, encompassing mountainous and downstream areas. This vital resource is harnessed for purposes ranging from hydropower generation to agricultural irrigation and the sustenance of domestic and industrial requirements. Any shift in the balance of the cryosphere can potentially exert profound influences, reshaping both human communities and the surrounding ecosystems.

The melting of glaciers, ice caps, ice sheets, and the broader cryosphere has a direct impact on rising sea levels. While there is ongoing research to precisely estimate the contribution of melting ice masses to sea level modification, current studies suggest they account for approximately 30% of sea level changes over the last century.

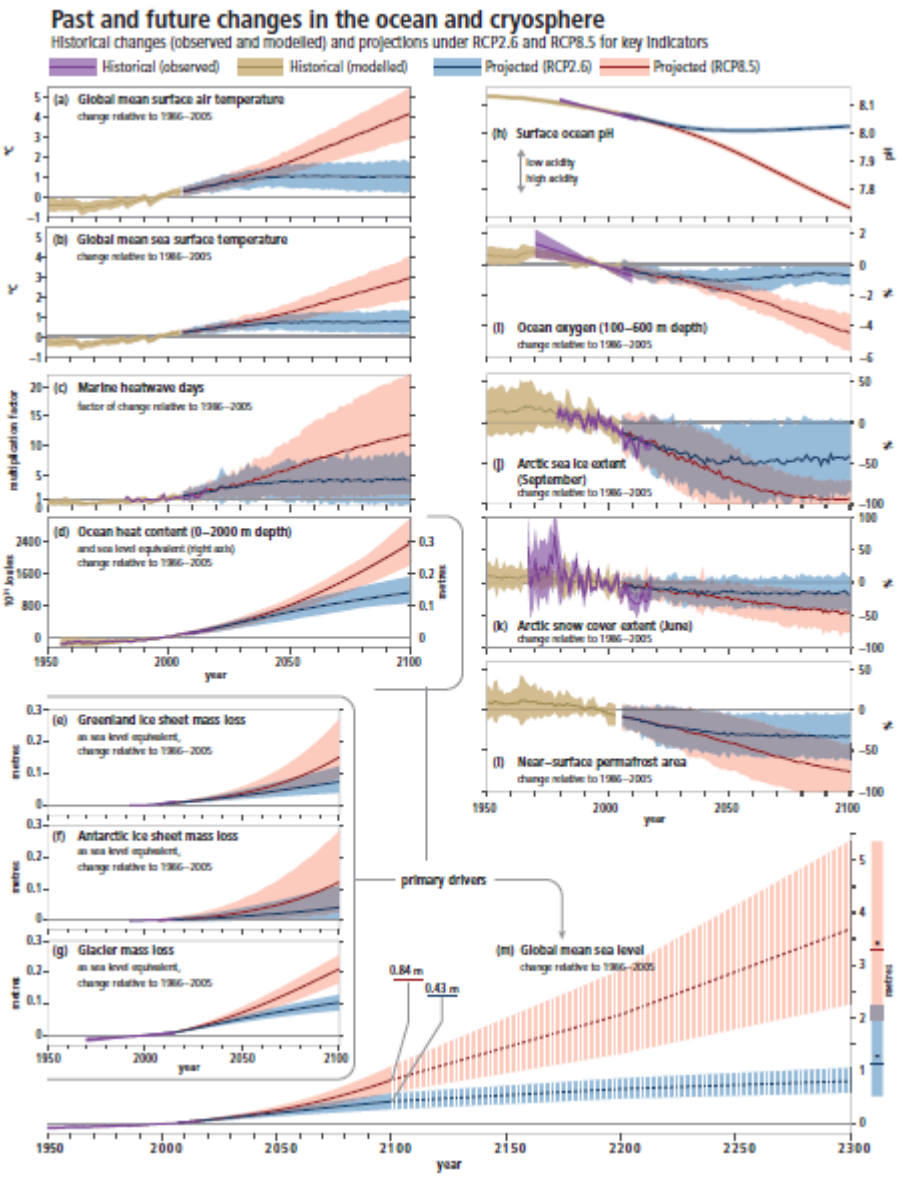

Figure 2.4 Observed and modelled historical changes in the ocean and cryosphere since 1950, and projected future changes under low (RCP2.6) and high (RCP8.5) greenhouse gas emissions scenarios (IPCC, 2019: Summary for Policymakers. In: IPCC Special Report on the Ocean and Cryosphere in a Changing Climate).

Additionally, the cryosphere, particularly in alpine regions, has significant socio-economic implications for mountain communities and tourism-dependent areas. The diminishing glaciers also exert an influence on water quality due to intensified anthropogenic pollutants affecting downstream ecosystems. This reduction in glaciers also disrupts hydropower production through altered runoff patterns and the release of sediment and debris from melting. In agriculture, the reduction of snowfall alters soil moisture and water supply levels for irrigation, possibly leading to the emergence of higher-altitude crops. Also, the tourism industry that relies on winter activities is affected by these phenomena. Rising temperatures lead to shorter and less predictable ski seasons. Warmer temperatures can result in reduced snow quality

and reliability, as in delaying the start of the skiing season and accelerating the end, reducing the overall window of opportunity for winter sports.

The ramifications of climate change in mountainous regions extend to water security, impacting both small-scale and regional scales, especially during dry periods. The changing cryosphere also increases the occurrence of natural hazards like landslides, avalanches, and flooding, all linked to the destabilization of long-standing geological formations. For instance, in the European Alps, the interaction of melting glaciers and increased sediment transport has led to heightened slope instability and landslide potential. Unprecedented heat waves in high-altitude regions can exacerbate melting and detachment phenomena from steep walls.

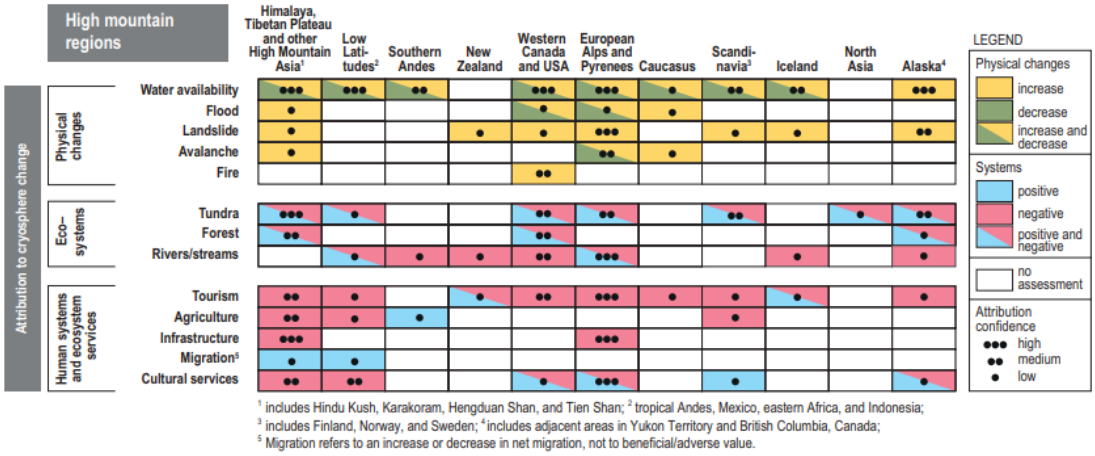

Figure 2.5 Synthesis of observed physical changes and impacts on ecosystems and human systems in eleven high mountain regions over the past decades that can at least partly be attributed to changes in the cryosphere. (IPCC, 2019: Summary for Policymakers. In: IPCC Special Report on the Ocean and Cryosphere in a Changing Climate).

Confidence is high that exposure to cryosphere hazards in high mountain regions has increased in recent years and is projected to persist (IPCC, 2021). The rise in rainy precipitation can amplify wet snow and avalanches, while heightened snowmelt can result in glacial lake expansion, increased water flow, and potential avalanches in periglacial lakes, culminating in flood risks. It's also essential to consider the economic significance of mountain areas, particularly in terms of tourism. The European Alps, renowned for their winter tourism and skiing industry, are at risk of substantial economic losses due to temperature increases, potentially leading to increased costs and financial vulnerability.

Moreover, changes in the cryosphere have far-reaching implications for cultural values and human well-being. From Arctic Island states to indigenous communities in Nepal's Annapurna Conservation Area, the alterations in mountain environments threaten cultural identities and livelihoods. Notably, 46 out of 247 UNESCO World Heritage natural sites encompass glacier regions, and projections indicate that eight of these sites could vanish by 2100 under varying scenarios (IPCC, 2017, 2021).

Mitigation strategies primarily aim to address hazards linked to rising temperatures, while adaptation approaches in this domain are still evolving. Often, adaptations involve community-driven modifications, such as altering agricultural practices and water management. However, it is unclear how effective they are over a prolonged period of time.

Climate change in glacial environments is predicted to amplify cryosphere hazards and trigger a comprehensive reshaping of ecosystems, habits, and equilibrium for populations that interact within these contexts. The imperative for safeguarding both the human population and biodiversity in these vulnerable areas necessitates vigilant glacier monitoring as a foundational step toward mitigating and adapting to these evolving circumstances.

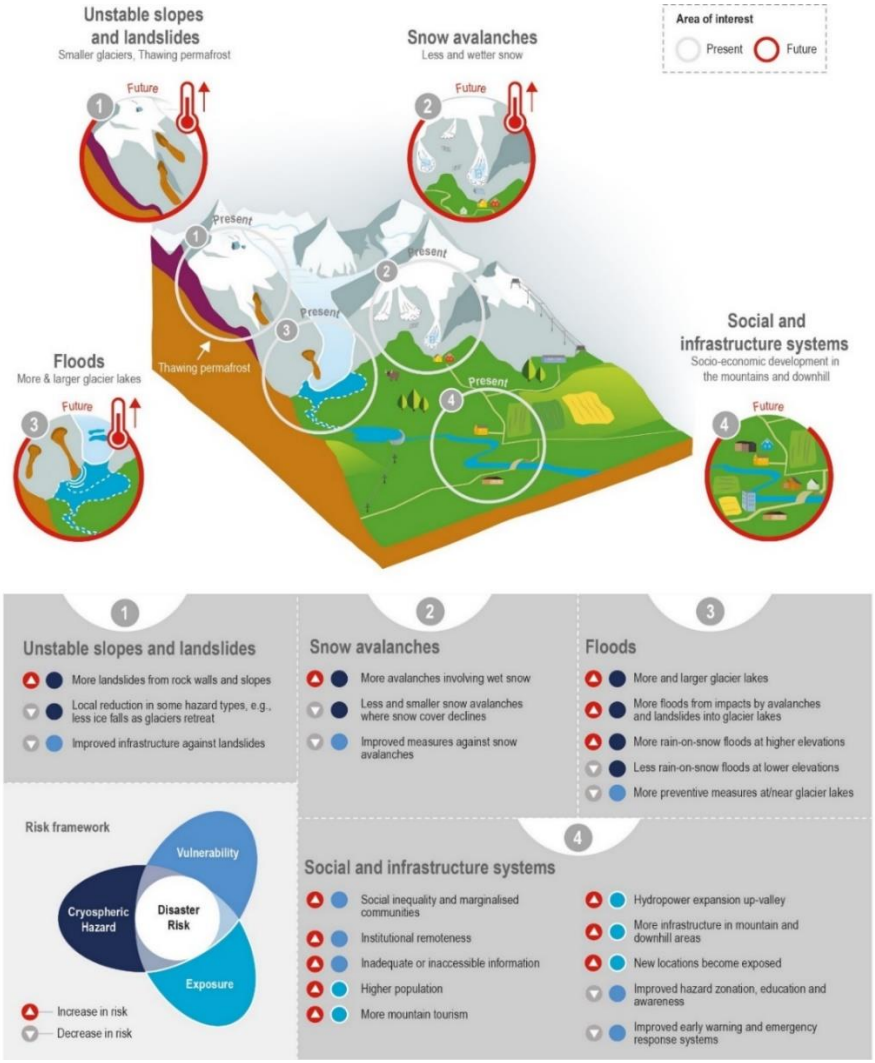

Figure 2.6 Anticipated changes in high mountain hazards under climate change, driven by changes in snow cover, glaciers and permafrost, overlay changes in the exposure and vulnerability of individuals, communities, and mountain infrastructure (IPCC, 2019).

2.2 Glaciers and Proglacial Areas Monitoring

2.2.1 Why?

Acting as indicators of climate change, glaciers and proglacial areas are environments that should be monitored over time. However, the study and monitoring of Alpine glaciers and proglacial areas are of crucial importance for several other reasons, too, which are listed below and have been briefly described in the previous paragraphs.

1. Indicators of climate change.
2. Supply of water resources.
3. Risk management. Monitoring glaciers and proglacial areas aids in assessing and managing the risk of events such as avalanches, landslides, and glacial outburst floods, providing crucial data for infrastructure planning and community protection.
4. Habitat and biodiversity: Proglacial areas, where glaciers are retreating, are unique environments that host a variety of habitats and unique species. Glacier retreats and the formation of proglacial lakes and valleys can influence biodiversity and species behaviour, as well as local ecological processes. Monitoring these areas helps to better understand the impacts of environmental change on fauna and flora.

In summary, the study and monitoring of Alpine glaciers and proglacial areas have significant implications across a wide range of sectors, from understanding climate change to managing water resources and conserving biodiversity. This research is essential to inform policy decisions, develop adaptation and mitigation strategies, and preserve mountain ecosystems and the communities connected to them.

2.2.2 How?

A systematic and synchronized monitoring effort to track changes in glacier extent (frontal variations or length shifts) with annual temporal resolution was initiated as early as 1893 during the 6th Geological Congress in Zurich. Initially encompassing a few hundred glaciers worldwide, this sample expanded to over 900 glaciers for several decades (from 1960 to 1990), and currently stands at approximately 600 glaciers (Zemp et al., 2015; Paul et al., 2019; Heckman et al., 2019).

Monitoring of these environments mainly takes place annually, to assess the extent of the glacier retreat at the end of the summer ablation period (Macelloni, 2022).

For a select number of glaciers, records of their terminus changes have been documented since 1850, although often lacking annual precision (WGMS 2008; Vaughan et al. 2013). Furthermore, for certain glaciers, not only frontal shifts (one-dimensional data) but also lateral extents have been reconstructed, offering a two-

dimensional (2D) perspective on their former glacier area, particularly for their lower sections (Zumbühl and Holzhauser 1988).
Since 1986, the World Glacier Monitoring Service (WGMS) has been in charge of collecting standardized observations on changes in mass, volume, area and length of glaciers over time (glacier fluctuations). It also compiles statistical information regarding the spatial distribution of perennial surface ice (glacier inventories). These glacier fluctuation and inventory datasets hold substantial significance as key variables in climate system monitoring. They serve as a foundational resource for hydrological modelling in relation to the potential impacts of atmospheric warming and provide fundamental insights into glaciology, glacial geomorphology, and quaternary geology. The highest information density is found for the Alps and Scandinavia, where long and uninterrupted records are available (WGMS 2015 and earlier versions, wgms.ch/ggcb).
With each year being added, the time series gains incremental value, serving a multitude of purposes including enhancing process understanding, detecting climate change patterns, and fine-tuning model calibration.
Detailed reconstructions of earlier glacier fluctuations are primarily constructed from indirect evidence sources, such as dated moraines, dendrochronology, and paintings (Paul et al., 2019; Heckman et al., 2019).

Satellite imagery offers alternative and largely free access to the reconstruction of glacial fluctuations. In comparison to ground-based data, satellite images cover a more limited period (e.g., Landsat Multi-Spectral Scanner (MSS) from 1972, Thematic Mapper (TM) from 1984) and may not be available for every year within a specific region due to factors such as cloud cover or acquisition strategies. Additionally, freely accessible satellite data with extensive historical records, such as Landsat, have a limited spatial resolution (MSS: 79 m, TM: 30 m), limiting the ability to monitor changes with finer temporal intervals (e.g., every 5–10 years, depending on the rate of change). However, these drawbacks are counterbalanced by the full spatial coverage of an entire region, capturing all glaciers within the area, rather than only a limited selection with easy ground access.

Satellite images are predominantly employed for the mapping of glacier extents (i.e., outlines), instead of front variations. Given that satellite data is available for regions or periods that may lack ground-based information, it can complement existing datasets in this aspect (Barandun et al. 2015). A notable advantage of satellite imagery lies in its potential for automatic classification of clean glacier ice using a straightforward band ratio approach (e.g., red divided by short-wave infrared band) combined with a segmentation threshold to create a binary image map. Subsequently, raster-to-vector conversion techniques can convert this map into glacier outlines (Paul 2002, 2015; Bolch and Kamp 2006).

Finally, uncrewed aerial vehicles (UAVs), also known as unmanned aircraft systems (UAS) or drones, have come to the forefront in the past. Combined with Structure-from-Motion (SfM) photogrammetry, UAVs established an exceptionally efficient workflow in the field of glacial and paraglacial geomorphology, filling the gap between traditional ground-based surveys and satellite remote sensing data. Various models of small Uncrewed Aerial Systems (UASs) are available in the market, designed for easy portability by an individual and providing a favourable balance between cost and benefit. This strategy allows the capture of imagery from relatively low altitudes, enabling highly detailed reconstruction of 3D features.

The data obtained from UAVs present a versatile spatial and temporal resolution, thereby facilitating a transition from mere descriptions of geomorphological features to a more profound comprehension of the relationships between processes and forms, e.g., by quantification of short-term landscape changes in response to various influencing factors.

Current applications of UAV-SfM in studies of modern and past glacial environments generally encompass geomorphological mapping and change-detection analysis. Researchers also indicate potential future applications, e.g., by combining UAV data with historical archives, terrestrial SfM, and crowd-based image gathering to allow for a better understanding of landscape changes in response to present climate warming (Śledź et al., 2021).

Measurement in photos, by satellites or UAVs, means also measuring points on the object without physical contact with the object. Therefore, photogrammetry and satellite images are useful for glacial and proglacial environments, in which the object cannot easily be reached (Kappas, 2011).

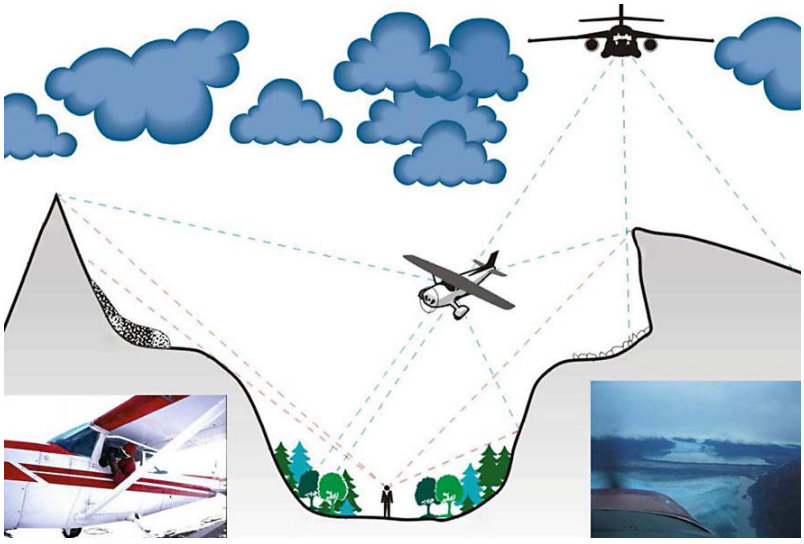

Figure 2.7 Schematic of aerial photogrammetry for glacial monitoring. (Kappas, 2011)

In glacial and proglacial environments, the difficulties related to equipment transportation and the limited accessibility of the areas to be monitored, along with the cost and risk of the measurement campaigns, are parameters of fundamental importance in the choice of the monitoring techniques to be adopted (Macelloni, 2022).

2.2.3 Geomatics Tools

For this study, the need for monitoring has required the implementation of in-situ measurement campaigns and the application of different geomatics techniques. Before highlighting the specific tools applied, a brief definition of geomatics follows. Geomatics is a *"systemic, multidisciplinary, integrated approach for selecting the instruments and the appropriate techniques for collecting, storing, integrating, modelling, analysing, retrieving at will, transforming, displaying, and distributing spatially georeferenced data from different sources with well-defined accuracy characteristics and continuity in a digital format"* (Gomarasca 2010).

The tools applied in the very first step of this work, which was monitoring and collecting data, are:

- Global Navigation Satellite System (GNSS)
- Geographical Information Systems (GIS)
- Aerial photogrammetry

Global Navigation Satellite System (GNSS) enables the precise localization of objects, achieving accuracy down to a few centimetres. This system relies on radiofrequency signals emitted by dedicated satellite constellations, such as the Global Positioning System (GPS), which are collected by ground receivers. By determining the satellite's position in relation to the Earth and calculating the satellite-receiver distance, the coordinates of a specific point can be established. This distance is derived indirectly by measuring the signal's time or phase emitted by the satellite and received by the receiver.

Geographical Information Systems (GIS) represent complex systems designed to store, manage, analyse, process, and visually present geographic data. They enable the integration of tools capable of receiving, recording, depicting, and manipulating georeferenced spatial data.

Aerial photogrammetry, a technique reliant on images briefly described in the previous paragraph, facilitates the reconstruction of three-dimensional models and the determination of intrinsic attributes along with their spatial positioning.

2.2.4 Aerial Photogrammetry

Several studies have already validated the potential of UAS photogrammetry (Barry and Coakley 2013, Gülch 2011, Haala et al. 2009, 2011, 2012, 2013, Küng et al. 2011, Vallet et al. 2011, Rosnell and Honkavaara 2012). Noteworthy advantages include the cost-effectiveness, the automation and high repeatability of surveys, and the exceptional resolution of the final output. Instead, drawbacks are associated with the post-processing phase.

Essential components for proficient aerial surveys using UASs include:

- a camera equipped to capture high-resolution imagery. this camera comes with distinct specifications like resolution, lens type, and image stabilization features;
- a GNSS receiver for precise location determination and georeferencing of the captured images;
- an inertial measurement unit (IMU) for assessing UAS orientation and acceleration. It provides data on roll, pitch, yaw angles, and linear accelerations, enhancing UAS stability and result accuracy;
- a wireless communication system for linking with a ground control station, enabling real-time monitoring (RTK) of flight status, command reception, and data transfer;
- an onboard small computer processor managing diverse tasks such as image processing, data storage, flight control algorithms, and component communication.

Specifically, the concept behind the application of photogrammetry for proglacial area surveys is relatively easy. It mainly takes place annually, to assess the extent of the glacier retreat at the end of the summer ablation period. The careful planning of the aerial survey during more favourable weather conditions is fundamental. Low wind (< 25 km/h) and short shade hours are preferred related to the specific UAS capability. Also, clear or uniformly cloudy skies are the optimal conditions. Being proglacial areas particularly prone to cloud cover, weather conditions present a constraint for aerial survey flights, and waiting for favourable weather can be time and cost-intensive in some instances.

The camera captures images with a designated overlap percentage, forming the basis for the Structure from Motion technique. These images, with around a 10 cm Ground Sampling Distance (GSD), yield a Digital Surface Model (DSM) or Digital Elevation Model (DEM) boasting a vertical accuracy of approximately 20 cm (Gonçalves et al. 2010, 2011).

The GSD [m] depends on flight height, H [m], focal length, f [mm], sensor dimension, and image dimension. This geometric ratio is readily estimated via tools like the PIX4D calculator.

Figure 2.8 2022 campaign - © Politecnico di Torino – DIATI | cc@polito

Utilizing photogrammetric processing software employing the SfM approach, the 2D DSM, orthomosaic, and 3D point cloud are generated. Subsequently, georeferencing can be accomplished. This can be achieved through direct photogrammetry thanks to the embedded GNSS receiver in the UAS, offering accuracy matching the GNSS signal. Alternatively, known coordinate points called Ground Control Points (GCPs) can be used for georeferencing. These GCPs can be natural elements identified from collected images or markers pre-placed on the ground for this purpose before the survey.

2.3 Paraglacial Geomorphology

In the late 19th century and by the early 20th century, "glacial theory" developed, encompassing glacial geomorphology with the description of glacial landforms and mapping of glaciated terrains. Over time, the field has forged intricate connections between glaciology, dating techniques, Geographic Information Systems (GIS), hydraulic modelling and glacial sedimentological studies. With these linkages, major paradigm shifts and scientific advances have increased our understanding of glacial environments. With climate change and global warming, understanding the latest glacial environments gains paramount importance (Menzies, 2018).

In this study, after the data collection performed using geomatics monitoring techniques, the bathymetry of a system of proglacial streams was reconstructed. The channelized streams develop covering an alpine highland downstream of the Rutor glacier, joining in a shallow lake, known as Lago Marginale.

Figure 2.9 Photo of the Marginale Lake, 18th July 2023.

Bathymetry mapping is the prerequisite activity that sets a basis for hydrological modelling and paraglacial geomorphology. To make evaluations of water quality, habitat conditions, and environmental flow for riverine ecosystems via hydraulic modelling, for a proper understanding of sediment fluxes and also inferring geomorphic responses to climate changes in proglacial environments, it is necessary to first undertake bathymetric mapping (Kim et al., 2019; Heckman and Morche, 2019).

2.3.1 Conventional methods for bathymetry mapping

Rivers and streams commonly exhibit irregular shapes, including confluences and meander bends, resulting in intricate flow patterns characterized by recirculating motions and centrifugal-induced secondary currents (Kalkwijk and De Vriend, 1980; Jia and Wang, 1999; Ferguson et al., 2003). Due to these complexities, precise and high-resolution bathymetric data have gained recognition as essential input elements for river modelling, serving to enhance the overall performance of the models (Crowder and Diplas, 2000; Merwade, 2009).

Traditional methods of surveying stream bathymetry have traditionally involved direct measurement techniques like robotic total stations (RTS), real-time kinematic global positioning systems (RTK-GPS), and echosounders mounted on moving vessels, as documented by Brasington et al. (2000), Julien et al. (2002), Lamarre and Roy (2008), and Kim et al. (2018). However, these on-site methodologies are known for their time-consuming, labour-intensive, and expensive nature, particularly when dealing with inaccessible areas (Ceyhun and Yalçın, 2010; Ding et al., 2018).

Bathymetric Light Detection and Ranging (LiDAR) systems, in contrast, offer the advantage of rapidly providing seamless topography data (Guenther et al., 2000) and have been employed for river bathymetry measurements (Kinzel et al., 2007; Hilldale and Raff, 2008). However, the utilization of such systems demands specialized algorithms to manage the extensive data and is contingent on water clarity at the study sites, as pointed out by Legleiter et al. (2009) and Abdallah et al. (2013).

In recent decades, an increasing number of studies have turned to remote sensing techniques for reconstructing bathymetry in coastal and inland waters, leveraging the spectral information present in multispectral and hyperspectral imagery, as demonstrated by Philpot (1989), Legleiter et al. (2004), Fonstad and Marcus (2005), Carbonneau et al. (2006), Lyzenga et al. (2006), and Pan et al. (2015). The radiance observed by remote sensors can be described as (Kanno and Tanaka, 2012):

$$L_t(\lambda) = L_a(\lambda) + L_s(\lambda) + L_w(\lambda) + L_b(\lambda)$$

where $L_t(\lambda)$ is the total radiance reaching a remote sensor; $L_a(\lambda)$ is the atmospheric scattering; $L_s(\lambda)$is the water surface-reflected radiance; $L_w(\lambda)$ is the in-water scattering corresponding to the water depth; $L_b(\lambda)$ is the radiance reflected by sea or stream beds (substrate); λ indicates the wavelength (spectral band) of remote-sensing imagery. In fact, the solar irradiance, in the impact of a water surface, breaks down according to different interaction mechanisms.

This radiance is nothing but the colour that the human eye perceives. When observed in small quantities, pure water is a substantially colourless element. Which justifies its very low reflectivity and high visible transmissivity. In the observation of a water body, it is necessary to consider the different contributions listed above.

In any case, the components of the previous equation different from $L_w(\lambda)$, the most important information needed, turn out to be a disturbance and undesired; the most arduous task of aquatic remote sensing lies precisely in isolating the radiance of interest from these components. The portion of energy reflected by the water, when it is pure, can reach a maximum of 3% of the incident radiant flux and is confined mostly to the bands of blue-green light from where a continuous decrease is observed going towards the lengths of longer waves, until completely absorbed, already from near-infrared. The colour of the water, therefore, is not an intrinsic property but depends almost exclusively on the influence of the surrounding environment, such as the colour of the sky or that of the seabed, and the result of the diffusion caused by the presence of compounds such as phytoplankton, the suspended sediment, the organic component, or other substances.

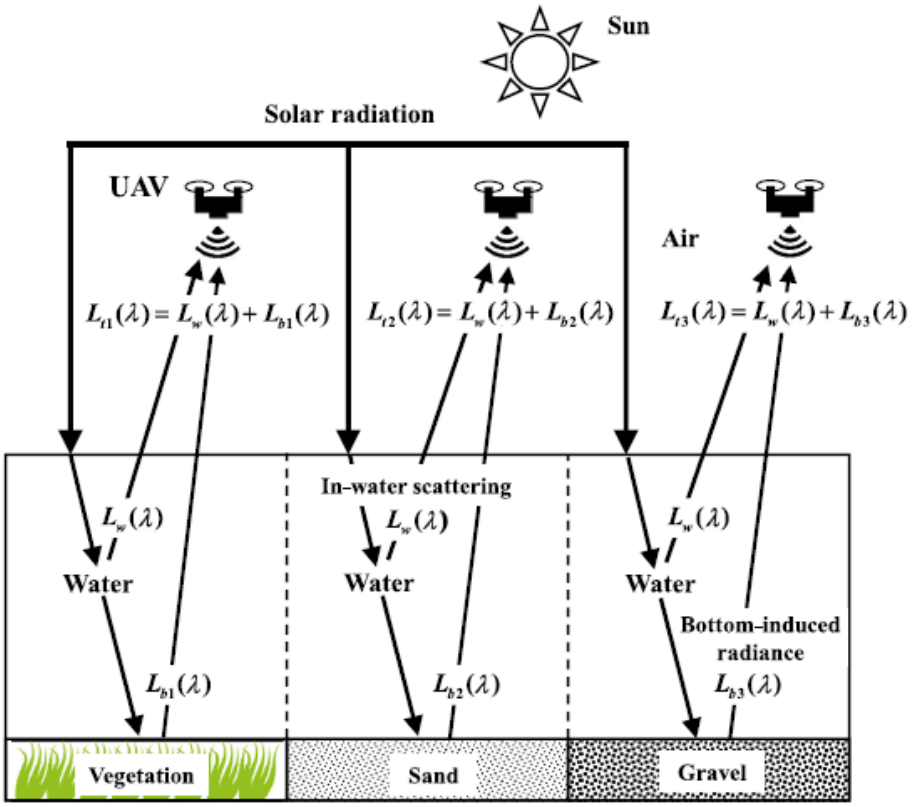

Figure 2.10 Effect of variable bottom types on remote-sensing radiance. Atmospheric scattering and water-surface-reflected radiance are ignored (Kim et al., 2019).

Within these variables, $L_a(\lambda)$and $L_s(\lambda)$ can be eliminated by atmospheric and sun-glint correction algorithms. In optically deep waters such as oceanic and lacustrine systems, $L_b(\lambda)$ usually has no significant effects on $L_t(\lambda)$ (Ma et al., 2011; Reichstetter et al., 2015). Thus, it becomes feasible to approximate water depth using remotely sensed data by considering $L_t(\lambda)$ as equivalent to $L_w(\lambda)$. Instead, in-stream and near-shore applications, this approximation is not valid due to the significant influence of $L_b(\lambda)$, particularly in shallow waters, as depicted in Figure 2.10 (Su et al., 2008; Legleiter et al., 2016). Consequently, accurately extracting $L_w(\lambda)$ from $L_t(\lambda)$ necessitates the identification of $L_b(\lambda)$.

Traditional bathymetric inversion algorithms relying on multispectral imagery typically assume a uniform relationship between water depth and $L_t(\lambda)$, assuming $L_b(\lambda)$ remains constant across the entire study area (Stumpf et al., 2003; Legleiter, 2013). However, rivers and streams frequently exhibit varying bottom types, resulting in spatially heterogeneous $L_b(\lambda)$ due to diverse bed materials like sediments, pavements, in-stream vegetation, and periphyton (Beisel et al., 2000; Cotton et al., 2006; Hondzo et al., 2013). This complexity limits the effectiveness of conventional global inversion models in cases where $L_b(\lambda)$ varies spatially. Although specialized inversion algorithms have succeeded in separating $L_b(\lambda)$and $L_t(\lambda)$ in coastal regions, this remains a challenge and is optimally achieved with hyperspectral imagery

(Brando et al., 2009; Lee et al., 1999; Ma et al., 2014; Wozencraft et al., 2003; Cannizzaro and Carder, 2006).

Some researchers reconstructed bathymetry using a methodology able to reduce the refraction error on photogrammetric data in fluvial environments, like the iterative Dietrich's refraction correction method (Lingua et al., 2023), or one based on Snell's law or on a polynomial correction relying on the physical and photogrammetric characteristics of the investigated object (Pontoglio et al., 2020).

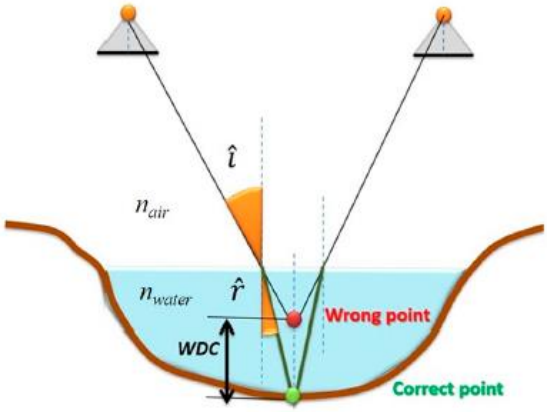

Figure 2.11 (Pontoglio et al., 2020) Water depth underestimation. Where WDC is the water depth correction, $\hat{\imath}$ and $\hat{r}$ the angle of incidence and angle of refraction of light, n_{air} and n_{water} are the refractive indices of air and water respectively. The Snell's law is

$$\frac{\sin i}{\sin r} = \frac{n_{water}}{n_{air}}$$

This study introduces a geographically weighted regression (GWR) model to enhance the accuracy of bathymetry mapping in streams with heterogeneous bottom types. The GWR model establishes local linear relationships between predictors and target values, incorporating geographical attributes specific to each location (Brunsdon et al., 1996). This geospatial regression approach effectively captures the spatially varying relationship between $L_t(\lambda)$ and water depth, accounting for the diverse substrates in stream environments. Several studies successfully retrieved bathymetry using GWR in near-shore coastal regions from multispectral imagery (Su et al., 2014; Monteys et al., 2015; Vinayaraj et al., 2016), where the heterogeneity of bottom types causes variability in the relationship between remotely-sensed radiance and shallow water depth. However, the application of this local inversion model to stream environments remains limited.

In the field experiment, the remote-sensing radiance measured by the sensor, $L_t(\lambda)$, is represented by a digital number (DN). The concept of DN is here introduced and will be helpful for the understating of the next paragraph. It refers to the numerical value assigned to a pixel in a digital image and corresponds to a particular brightness or intensity level. So, the DN represents the radiometric information enclosed in each pixel. DN is also called "digital value," "pixel value," or "digital intensity." UAV images are composed of different spectral bands: red, green and blue if the sensor works in

the visible range of wavelengths; near-infrared, thermal infrared and so on if the sensor is multi or hyperspectral. A DN value is assigned for each band of the image for every pixel. 8-bit images are the most common format of UAV imagery, and their DN can range between 0 and 255. This means that each pixel of the image can assume 256 values. There are also greater bit depth images, like 16- or 32-bit. For example, with 16 bits, there are 2^{16} possible combinations of bits, which correspond to 65536 distinct possible values (from 0 to 65535). As a result, a 16-bit image can represent a wider range of details and nuances compared to an 8-bit image.

2.3.2 Spatial statistics for environmental applications

When extracting bathymetric information from multispectral imagery, the commonly accepted approach for estimating water depth through bathymetric inversion models involves utilizing the natural logarithmic values of the band ratios derived from two distinct spectral bands (as indicated by Stumpf et al., 2003; Legleiter et al., 2009; Legleiter, 2013). This is represented by the ratio between the digital number of each band. To define the optimal band ratios from all possible combinations of the multispectral bands, this study employed the principal component analysis (PCA).

Principal component analysis (PCA) is a method that reduces the dimensionality of data while preserving its essential information. This technique is particularly valuable for datasets that have a large number of features. It finds frequent application in tasks like image processing and genome research, which often involve working with datasets containing thousands or even tens of thousands of variables. Although a larger volume of data is consistently advantageous, there are instances in which the abundance of information within datasets can lead to excessive model training durations and result in the development of dimensionality as a significant issue. Diminishing the count of variables invariably implies a compromise in accuracy; nonetheless, the art of dimensionality reduction lies in exchanging a slight degree of accuracy for enhanced simplicity. This is grounded in the notion that smaller datasets facilitate more efficient exploration and visualization, consequently rendering the analysis of data points considerably faster and more straightforward for machine learning algorithms.

Basically, it transforms the original dataset into a set of new variables, known as principal components, that are orthogonal (uncorrelated) to each other. Here are the steps involved in performing PCA:

1. Standardize the Data: The goal of this step is to standardize the range of continuous initial variables so that they all have equal impact on the analysis. Each variable's values can be standardized by subtracting their mean and dividing by their standard deviation.

$$z = \frac{value - mean}{standard\ deviation}$$

   This is crucial because PCA is sensitive to the scale of the data.

2. Compute the Covariance Matrix: The goal of this step is to understand if a correlation is present between pairs of the standardized variables. The covariance matrix says how the variables of the input data set vary from the mean with respect to each other.

$$\begin{bmatrix} Cov(x,x) & Cov(x,y) & Cov(x,z) \\ Cov(y,x) & Cov(y,y) & Cov(y,z) \\ Cov(z,x) & Cov(z,y) & Cov(z,z) \end{bmatrix}$$

Example of covariance Matrix, in this case for 3-dimensional Data.

3. Compute the eigenvectors and eigenvalues of the covariance matrix to identify the principal components. Eigenvectors represent the direction of the new feature space (called principal components), while eigenvalues indicate the variance of the data along these directions. They give insight into how much information each principal component carries. By ranking the eigenvectors in order of their eigenvalues, highest to lowest, the principal components are sorted in order of significance. The idea behind the principal components is that they are new variables that are built as linear combinations of the initial variables, in such a way that the new variables (i.e., principal components) are uncorrelated and most of the information within the initial variables is compressed into the first components. Geometrically speaking, principal components represent the directions of the data that explain the most variance. ("Principal Component Analysis (PCA) Explained | Built In")
4. Select Principal Components: Choose the top-k eigenvectors corresponding to the highest eigenvalues. The number of principal components selected depends on the desired dimensionality reduction.
5. Create the Projection Matrix and transform the data. Here a projection matrix is formed by stacking the selected eigenvectors as columns. This matrix will be used to transform the original data into the new feature space by multiplying the standardized data by the projection matrix.
6. Evaluate dimensionality reduction by computing the explained variance. The explained variance for each principal component is calculated by dividing its eigenvalue by the sum of all eigenvalues. This provides insight into how much variance each principal component retains from the original data, to decide on the number of principal components to retain. The aim is to retain a high proportion of the total variance while reducing dimensionality.

3. Case Study: the proglacial area of Rutor Glacier

The Rutor Glacier lies on the northwestern border of the Italian peninsula and forms part of the Italian-French border (as depicted in Figure 3.1).

Figure 3.1 Rutor geographical overview. Base map by ESRI.

It covers an area of 7.9 km^2 (Corte et al., 2023). It is 4.68 km long and extends from 2540 to 3486 m (head of the Rutor) above sea level. Among Valle d'Aosta's glaciers, it ranks as the third largest after the Miage and Lys glaciers.

It is also referred to as 'Ruitor' or 'Rhutor,' deriving its name from the French-Provençal language: 'Ru,' meaning a small river, and 'Tors,' highlighting a challenging path characterized by rocky jumps, tiers, and the precipitous course of a watercourse. The Rutor morphology is relatively flat, characterized by a combination of steep rocky ledges and sub-flat basins (Viani et al.,2020; Orombelli, 2005). Rocky ridges delimitate the upper part of the glacier (Testa del Rutor) and the peak called “Vedettes du Rutor” divides the glacier's front into two primary sections. Rocky zones partition the glacial front into three segments, bordered by moraines composed of glacial debris. The glacier terminates in three tongues at its front (Viani et al.,2020; Corte et al., 2023), and the eastern one reaches the lowest altitude of the glacier, which terminates in a lake, called Lago Superiore.

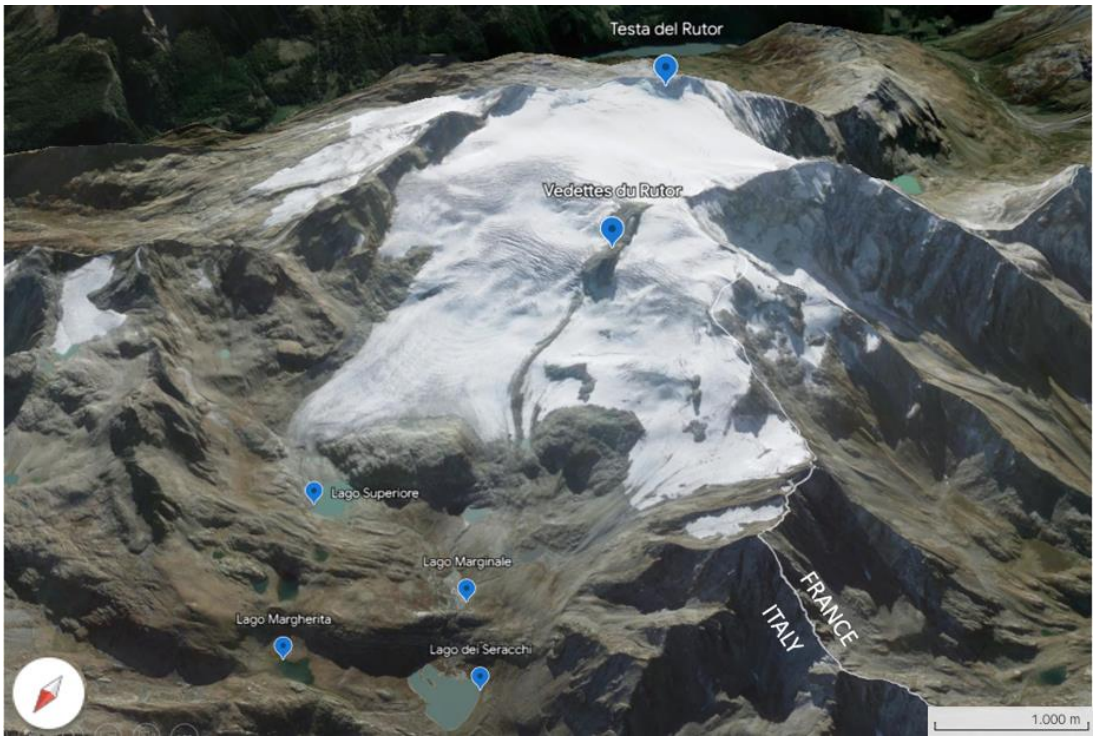

Figure 3.2. Overview of Rutor glacier and its proglacial area in 3D. Google Earth image.

A distinguishing feature of the Rutor is its proglacial area, which encompasses approximately 4 km^2, as detailed in Villa et al. (2007). This area holds significant relevance for the investigation of sediment dynamics within proglacial systems, primarily due to its diverse geomorphological characteristics. After the Little Ice Age (LIA), the retreat of the Rutor glacier has instigated a gradual expansion of its proglacial expanse. This glacier recession has brought forth previously concealed topographic depressions, leading to alterations in stream networks and the emergence of multiple proglacial lakes. These lakes serve as repositories for sediments, effectively blocking the transfer of sediments from the glacier's outlet to lower elevations. The elevation range between the lowest proglacial lake and the glacier terminus (middle tongue snout) spans from 2387 m a.s.l. to 2661 m a.s.l. Within the Rutor proglacial area, a variety of land-system components are evident, including steep slopes, outwash plains (sandurs), and both single and braided channels. Notably, the alluvial channel beds and banks exhibit a diverse range in composition, ranging from fine sands, silt, and clays to boulders (Corte et al., 2023).

At present, there are a total of five proglacial lakes that receive surface water supply from the eastern tongue of the glacier. In particular, two of these lakes have emerged within the last five years and are closely connected to the glacier lobe. Among these lakes, one prominent body of water is denoted as Superiore Lake (L1 in Figure 3.3), which ranks as the second-largest lake within the Rutor proglacial zone. It is sourced by multiple inflows, with a primary inflow originating directly from the glacier's eastern tongue. Following its accumulation, L1 discharges through a solitary outflow, which proceeds for a distance of 830 meters before entering a sandur.

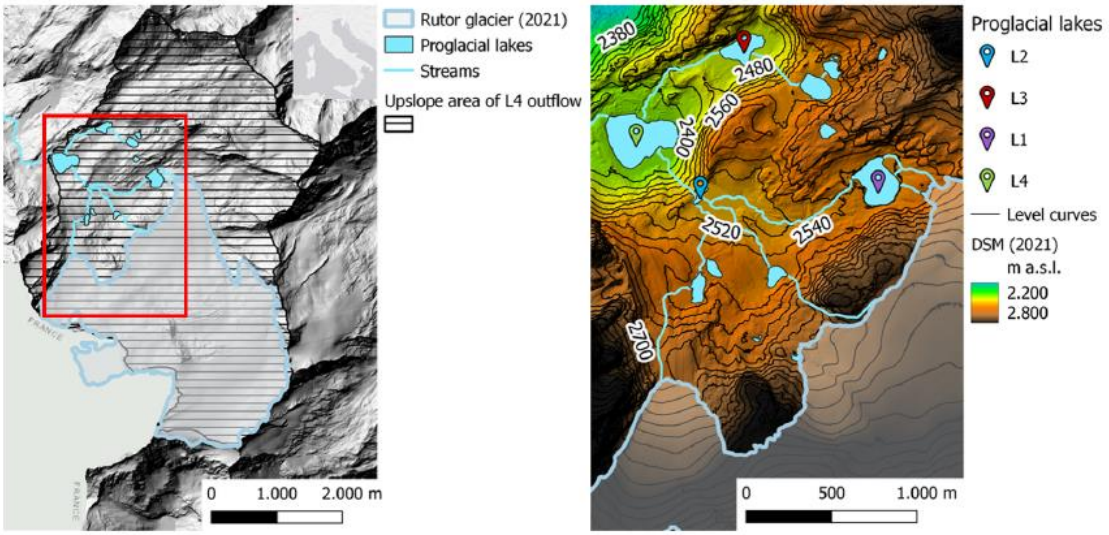

Figure 3.3 a) Digital Surface Model (DSM) as of 2008 of the Rutor glacier and the L4 lake catchment. The upslope area of L4 outflow (hatched area with continuous black lines) has been mapped using the 2008 model of Valle d'Aosta. The inset shows the location in Italy. b) DSM as of 2021 of the Rutor proglacial area and locations of L1, L2, L3 and L4 proglacial lakes. (Corte et al., 2023)

This sandur, fueled by the glacier's meltwater, spans an area of roughly 0.1 km^2. When the water level in the sandur rises, due to a topographic barrier present within it, another lake develops, called Marginale Lake (L2, 2504 m a.s.l.), which is the object of this work. Subsequently, water from L2 travels through a steep creek with a notable elevation drop of 100 m to the Seracchi Lake (L4) located at an elevation of 2387 m above sea level.

Another significant water body, Lake Santa Margherita (L3), now mostly represented by remnants of a peat bog, occupies a broad depression at an elevation of 2400 m a.s.l., intersecting perpendicularly to the glacier. Following 1820, the glacier front progressively receded, contributing to a gradual lowering of Lake Margherita's water level by approximately ten meters.

In the context of water dynamics, the outflows of L2 and L3 (Santa Margherita Lake) serve as the sole surface inflows for the L4 Lake. Notably, the outflow of L4 contributes to the majestic Rutor cascades. This fourth lake, L4, serves as the primary recipient of all meltwaters originating from the Rutor glacier and holds the distinction of being the largest and most downstream proglacial lake within the studied region. The outflow cross-section of L4 remains relatively stable, facilitating convenient measurement of the lake's discharge rate.

3.1 Rutor Glacier Retreat since the Little Ice Age

During the period known as the Little Ice Age (XIV-XIX centuries), the Rutor Glacier expanded significantly, reaching an elevation of 2150 m a.s.l. and extending up to the Lac Du Glacier above La Thuile. The Lac du Glacier, which was once more expansive

and now is partially filled with sediment, occupied the Plan de la Lière, a plain at an elevation of 2145 m a.s.l. This area is marked by two moraine ridges that delineate Rutor's maximum extent during the Little Ice Age.

Based on available studies, it is known that the Rutor Glacier's maximum expansion is dated back to 1864 (Viani et al.,2020; Orombelli, 2005), when the glacier had a surface area of approximately 12 km^2 (Villa et al., 2007).

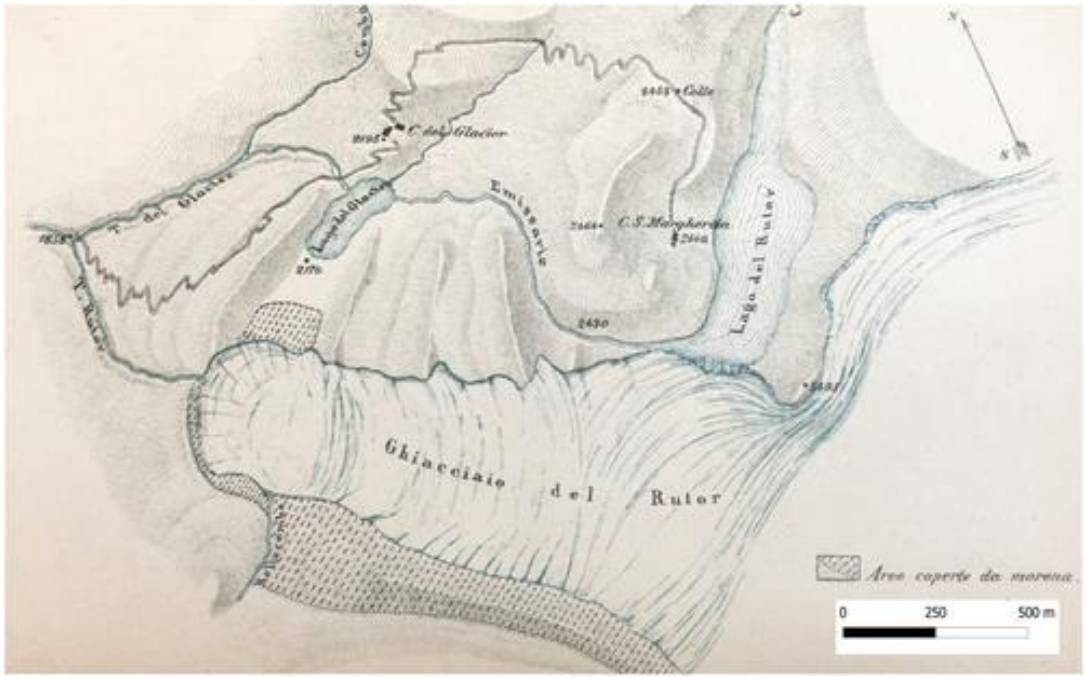

Figure 3.4. Chartography of Rutor basin in 1860 (Baretti, 1880). Lago del Rutor (now Lake Santa Margherita) fills the valley, blocked by the Rutor glacier, and discharges its water directly into Lac du Glacier, 250 m below. Superiore, Marginale and Seracchi Lakes do not exist yet [Colour figure can be viewed at wileyonlinelibrary.com] (Vergnano et al., 2023).

Since the conclusion of the Little Ice Age in the mid-19th century, the glacier has undergone a retreat of over 2 km, and up until the 1990s, an estimated ice loss of approximately 480 million cubic meters has been observed.

According to Villa et al., 2008: "From 1975 to the present, another 50% of the remaining volume was lost. This calculates to a volume reduction rate of –0,5%yr–1 from its maximum size during the Little Ice Age to 1975, a value of –1,1%yr–1 between 1975 and 1991, and a volume reduction rate of –2,1%yr–1 until 2006."

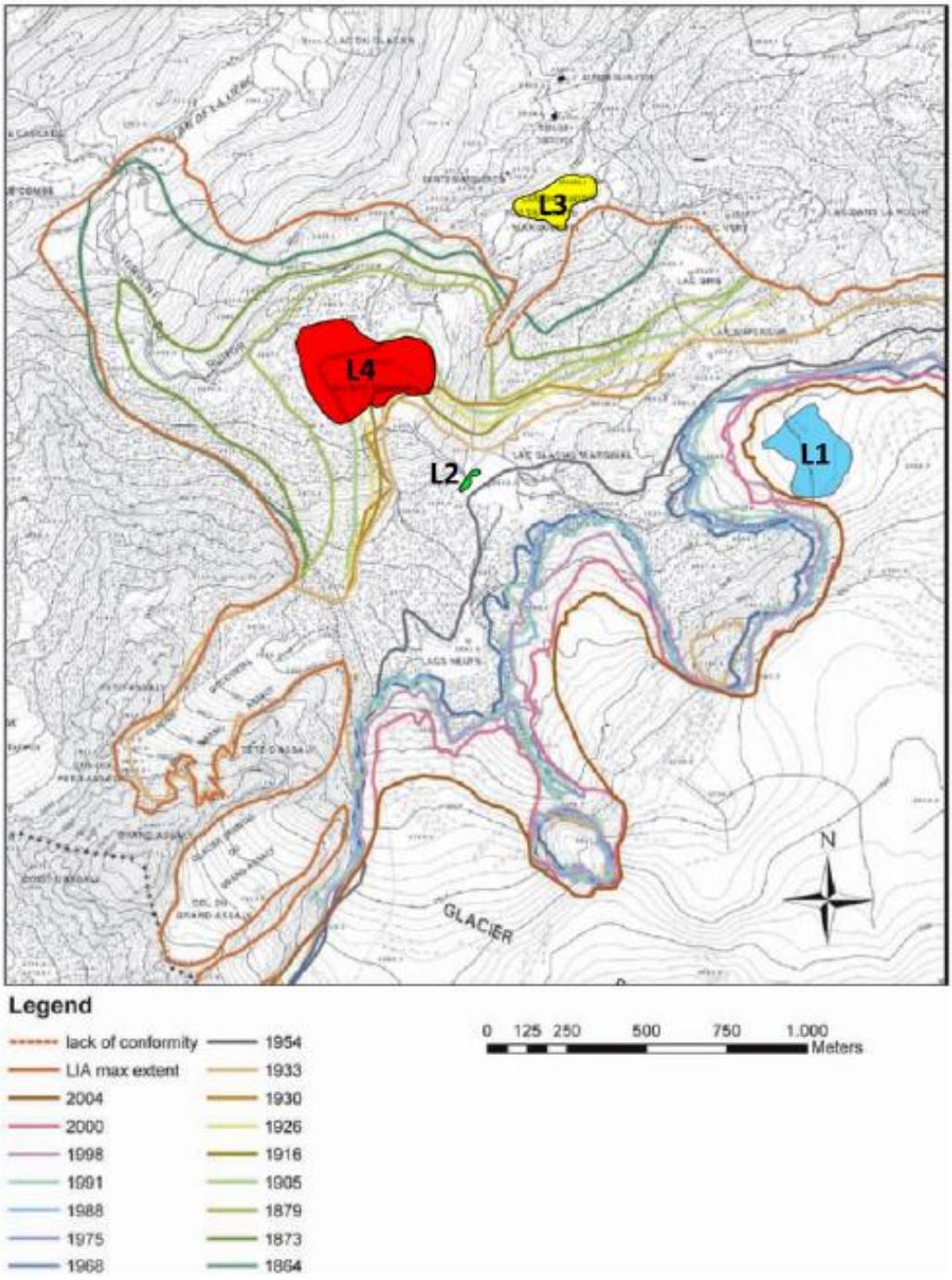

Figure 3.5. Reconstruction of the Rutor Glacier terminus from its maximum extent in LIA to 2004 (modified from Villa et al., 2007). The areas highlighted in blue, green, yellow and red indicate the current extent of lakes L1, L2, L3 and L4 respectively.

Since 2005, ARPA, the Aosta Valley regional agency for environmental protection has been monitoring the annual mass variation of the glacier. This variation is represented in Figure 3.6, expressed in mm of water equivalent, and is determined by calculating the net mass balance between winter-spring accumulation and summer ablation. The net mass balance for the 2021-2022 period resulted in -4.946 mm of water equivalent,

with a retreat of 31 – 40 m for the right tongue, 27 m for the left and 26 m for the central one (Arpa VdA).

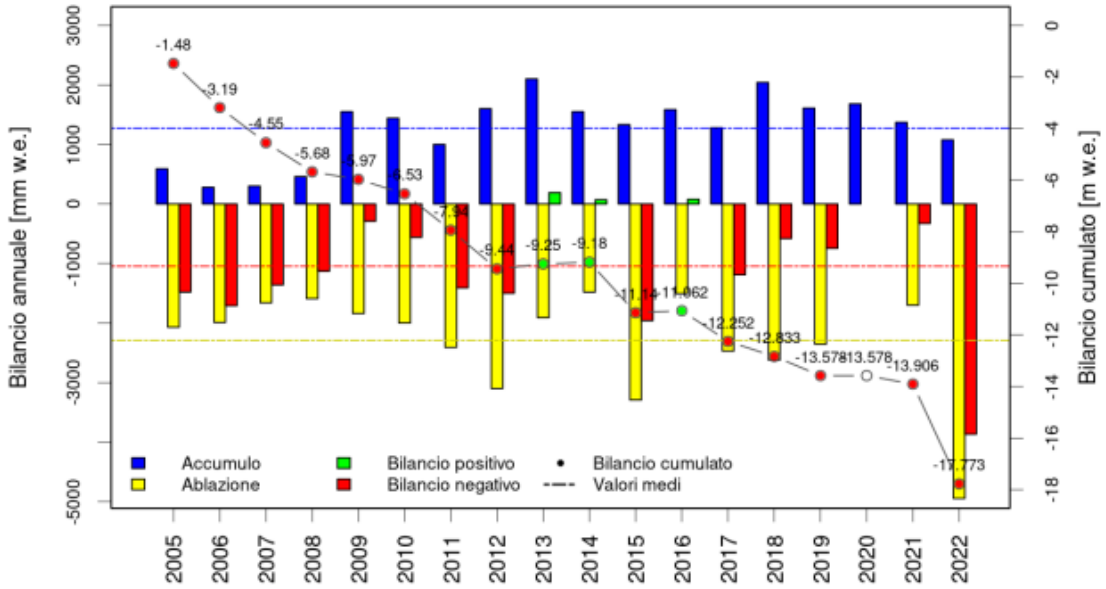

Figure 3.6 Rutor yearly mass balance for the period 2005-2022. The mass balance is calculated as winter-spring accumulation minus summer ablation (source ARPA VdA).

Under the new climate conditions, variations in the water and sediment budget of the lake become increasingly likely, posing the risk of catastrophic events and irreversible transformations. In fact, the increased sediment input, along with the area morphology, could contribute to the potential disappearance of these proglacial lakes in the future (Orombelli, 2005). The Rutor has experienced numerous instances of flooding, with the most severe and damaging occurrences documented between 1594 and 1598, as well as multiple events in the 17th century. Particularly, two notable flood events took place in 1751 and 1752. However, not all of these incidents have been meticulously recorded, as some recurred annually. In some cases, these flood events coincided with regional flooding, such as the one in 1640 that also led to the inundation of the town of Aosta. These floods were triggered by the presence of the glacial tongue obstructing the natural flow of water into Lake Santa Margherita. With rising water pressure, the rock face collapsed, resulting in flooding. The most recent glacial flood was registered in September 1864.

Given this context, the establishment of the "CC-Glacier Lab" at Politecnico di Torino - DIATI emerges as a significant initiative, forming part of the MIUR project "Department of Excellence." Operating as a multidisciplinary laboratory, the CC-Glacier Lab's primary mission revolves around identifying and comprehending the dynamics unfolding in proglacial regions undergoing deglaciation and associated mass movements. The chosen focus area for in-depth exploration is the Rutor Glacier and its adjacent proglacial zone, but also other glaciers in the Aosta Valley, Italy.

The importance of this research group lies in its interdisciplinary essence, bringing together researchers from diverse fields such as hydrology, geophysics, geomatics, and water engineering. Starting in 2021, the project has actively engaged in comprehensive data collection activities within the area, setting on-site survey campaigns along with continuous monitoring activities. Instrumentation has been strategically deployed across the region, enabling the collection of data spanning multiple years and encompassing entire melting seasons, thereby facilitating a comprehensive temporal assessment of the locale. Weather station, pluviometer, geophones, hydrometer, turbidimeter, ground control points for photogrammetry and other tools.

The CC-Glacier Lab project presents a unique opportunity to glean invaluable insights into the metamorphoses occurring in the Alps due to the impacts of climate change. Moreover, the knowledge gathered through this research holds the potential to contribute significantly to the formulation of effective strategies aimed at mitigating climate change effects and adapting to its far-reaching ramifications.

In conclusion, some pictures of the Rutor glacier and proglacial areas are shown below. They belong to historical archives and previous scientific research and field campaigns in the area. Moreover, they are presented in a manner that aims to encourage a comparison between the previous appearance of the site and the current one.

Figures 3.7 and 3.8 both represent an overview of the glacier as it can be seen from the path leading to the Deffeyes refuge, which is also visible in this pair of photos. These photos also capture the Vedettes du Rutor, the rocky peak that splits the glacier's front into two main sections.

Figure 3.9 shows the plain of actual Marginale Lake as it was in 1909: covered by the glacier. Figure 3.10 frames the glacier from a similar viewpoint, but from a greater distance, which allows a wider image of the same scene: the cascade outflowing from Marginale Lake and entering Seracchi Lake is pictured. Figure 3.11 displays the Seracchi Lake and the upstream slope, which was previously concealed by the glacier but is now crossed by the cascade.
Lastly, Figure 3.12 depicts the same slope and Margherita Lake.

Figure 3.7 Rutor 1926 (historical archive).

Figure 3.8 Rutor July 2021 (Macelloni, 2022).

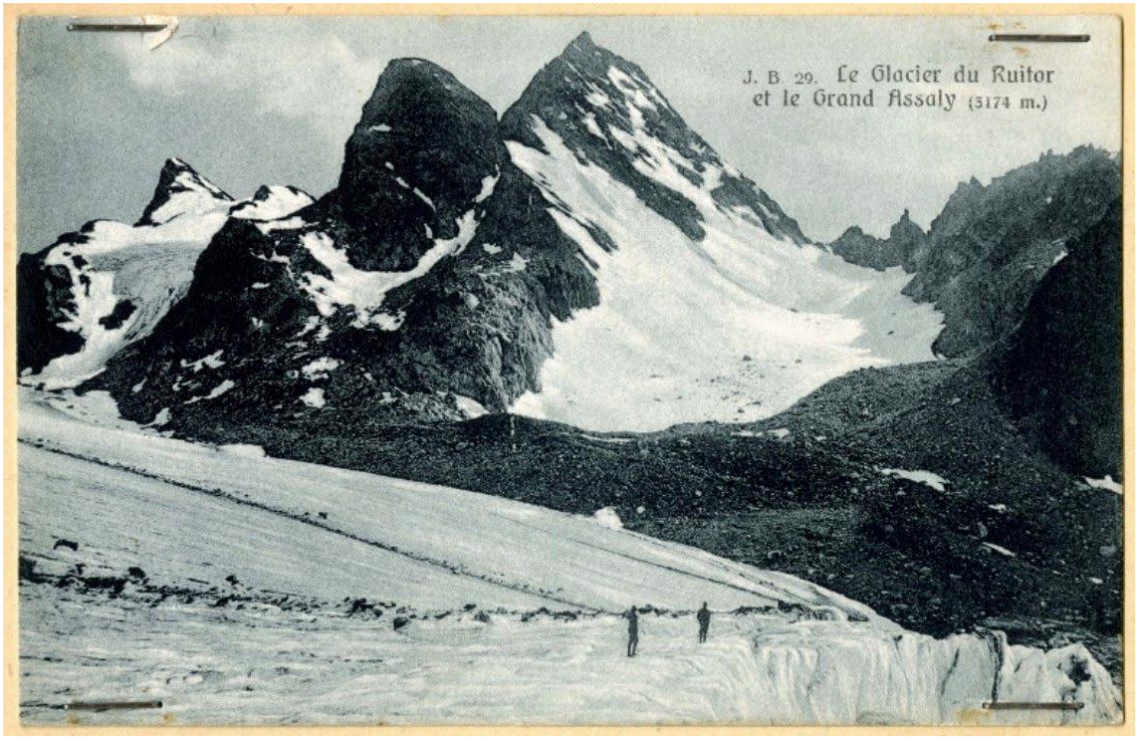

Figure 3.9 Brocherel, Rutor 1909 (historical archive).

Figure 3.10 Rutor Glacier in summer 2021 and Seracchi Lake (Macelloni, 2022).

Figure 3.11 Rutor Seracchi Lake 1909 (historical archive).

Figure 3.12 Santa Margherita Lake and the chapel on the top of the hill, summer 2021.

4. Methodology

4.1 Data Acquisition

To collect water depth and spectral imagery data, four field campaigns were conducted in the proglacial area of Rutor glacier, where the Lago Marginale (previously also called L2) is located. The field activities were performed on the 9th of July 2021 and, for 2023, on the 22nd of June, 18th of July and 2nd of September. Specifically, in 2023, the UAV survey was carried out in July, while the depth measurements are related to all the three expeditions.

Lake Marginale (Figure 4.1) spans an area of roughly 0.042 km^2 and is at 2504 m a.s.l. It covers an outwash plain and originates from an intricated system of streams fuelled by the glacier's meltwater. The bed materials of the alluvial channels are mainly fine sands, silt and, depending on the seasonal and daily changes in water level, submerged vegetation. This heterogeneity of the streambed could exhibit different patterns of bottom reflection on the remotely sensed data. The stream banks are mainly covered by bigger boulders and vegetation.

Figure 4.1 Marginale Lake, July 2023.

4.1.1 Photogrammetry Survey

The aerial imagery was collected using different UAVs in different years.

In 2021, images with 5472 × 3648 pixels in spatial resolution were acquired using a RGB-based digital camera mounted on a Phantom 4, DJI. The UAV was operated 126

m above the ground to cover the whole region of interest in the image frame. The RGB camera has a 20MP resolution and a focal length of 8.8 mm. The ground resolution or ground sample distance (GSD) obtained was 2.86 cm/pix. The flight was conducted in Real-Time Kinematic (RTK), which provides centimetric precision, thanks to the RTK GNSS receiver for real-time positioning integrated into the drone. Weighing 1380 grams and being compact, the DJI Phantom 4 was easy to carry on the site. Due to favourable weather conditions and the absence of winds, it successfully conducted flights during the measurement campaign. Moreover, when planning a survey in high mountain environments, it's crucial to account for the operating temperature range of the UAV, which typically spans from 0°C to 40°C. While the estimated maximum flight time is around 28 minutes, cold temperatures can significantly shorten this duration, necessitating frequent battery replacements. Throughout the campaign, four spare batteries had to be carried for on-the-fly changes as required.

Figure 4.2 Phantom 4 DJI (Macelloni, 2022)

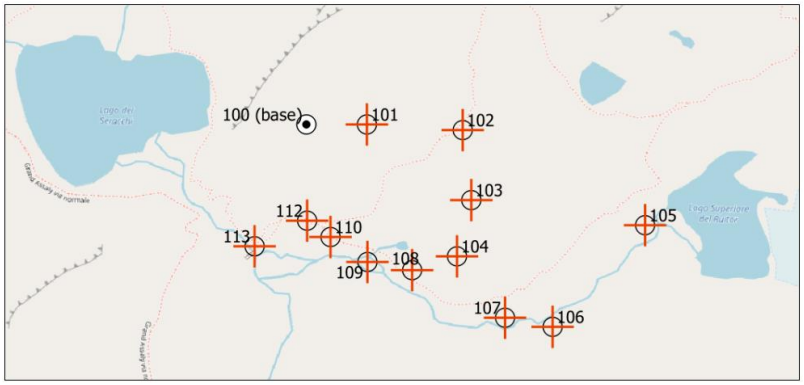

Figure 4.3 GCPs of July 2021 campaign (Macelloni, 2022).

Twelve stable points were measured, consisting of painted marks on stable boulders and canvas markers, georeferenced with RTK and static Global Navigation Satellite System (GNSS) positioning approach (Figure 4.3). These points will be then used in the processing phase as ground control points (GCPs), to improve the accuracy of the models. The GCPs positioning was performed using the GNSS base station DIATI100, placed in front of the Deffeyes hut (Figure 4.4).

Figure 4.4 GNSS base station DIATI100. Coordinates UTM ETRF2000, Est = 342979.659, Nord = 5059115.879, Ellipsoidal height = 2621.306, Orthometric height H= 2567.337 (Macelloni, 2022).

The base station is needed to get differential corrections (needed to improve the positioning accuracy) during the positioning of points when the NRTK approach is not feasible, meaning when there is no internet connection, which is a frequent scenario in mountain environments. Trimble SP80 receivers (Figure 4.5) were employed for all point positionings during the Rutor campaigns, both in 2021 and 2023. It was ensured that the instrument height was consistently marked each time, accounting for variations depending on the pole used. This variation was then subtracted from the measured height to obtain the precise point height. The specifications of the TRIMBLE SP80 receiver are detailed in the figure below.

Characteristics SP80 Spectra Precision	
Dimensions	
GNSS constellations and channels	GPS L1C/A, L1P(Y), L2P(Y), L2C, L5 GLONASS L1C/A, L2C/A - BeiDou B1 (phase 2), B2 Galileo E1, E5a, E5b QZSS L1C/A, L2C, L1SAIF, L5 SBAS
Precision Real-Time RTK	Horizontal 8 mm+1ppm Vertical 15 mm+1ppm

Figure 4.5 Trimble SP80 and its characteristics (Macelloni, 2022).

In July 2023, instead, a DJI Mavic 3M was used for the 2023 imagery. This UAV has two sensors, one RGB (20MP, focal length of 12 mm), and one multispectral (5MP, focal length of 4 mm), which covers the following wavelength ranges:

- Green (G): 560 ± 16 nm;
- Red (R): 650 ± 16 nm;
- Red Edge (RE): 730 ± 16 nm;
- Near-infrared (NIR): 860 nm ± 26 nm.

The imagery dimensions are 5280 × 3956 pixels, and 2592 × 1944 pixels, respectively for RGB and multispectral cameras. The flight height was 58.7 m, with a ground resolution (GSD) of 1.54 cm/pix. Also in this case the flight was conducted in RTK and ground control points were used: some of them were the same as the previous years' surveys, and some were installed and then removed. Their positioning was performed using the Trimble receiver previously introduced.

Figure 4.6 DJI Mavic 3M (online source).

As the drone camera's coordinates are specified in geographic coordinates ETRF2000 (Rete Dinamica Nazionale RDN2008), including longitude and latitude, they need to be transformed into cartographic coordinates: Est and Nord. Also, the altitude coordinate must be converted from ellipsoidal to orthometric height. Then, the image coordinates were orthorectified and converted to the UTM coordinates (RDN2008 / UTM zone 32N) through the software ConveRgo (Conversioni di coordinate per le Regioni), using Italian grids for projective transformation.

After each flight, the Agisoft Metashape software was used to generate the final models of the area surveyed, that, for the purposes of this work, were the orthomosaic

and the digital elevation model (DEM) of the area of Marginale Lake. For 2021 data, these products were provided by the geomatics researchers of the CC-Glacier Lab and they cover a bigger area, ranging from the glacier to the Seracchi Lake, of interest for their research; while data of the 2023 survey were processed specifically for the area of Marginale Lake.

The photogrammetric processing follows the standard Structure from Motion (SfM) workflow, which will be briefly described below. The input data of the processing are imagery and geolocation information, meaning coordinates of markers. Firstly, the images are aligned, and then, by collimating the stable points defined by the GCPs, a more precise spatial position of the image acquisition centres can be obtained. The collimation step can take time, as each marker must be searched for in the various photos and associated with the corresponding coordinates. Once the camera centres and georeferentiation are done, the dense cloud is built. Consequently, the mesh is created by interpolating the dense point cloud. The mesh is then used to generate the next product, which is the digital elevation model (DEM). Finally, the orthomosaic can be generated, too. The reports of the processing can be found in Annex 1.

For both datasets, the models were made using the reference system RDN2008 / UTM zone 32N (N-E) (EPSG: 6707), and all the processing steps were carried out with a high-accuracy approach.

For 2021, 1480 RGB images were aligned and nine GCPs from the twelve (Figure 4.3) measured on the field were used in the collimation phase. The residual errors estimated by the software for both camera location and GCPs are shown in the tables below.

Table 4.1 Average camera location error on drone model 9th July 2021.

X error [cm]	Y error [cm]	Z error [cm]	XY error [cm]	TOT error [cm]
0,667	0,950	1,098	1,161	1,598

Table 4.2 Residual errors on GCPs drone model 9th July 2021.

N. Points	X error [cm]	Y error [cm]	Z error [cm]	XY error [cm]	TOT error [cm]
9	1,675	1,849	1,786	2,4956	3,069

Due to its low flight altitude and RTK positioning, this survey returns highly precise 3D models with centimetre-level accuracy. These final models reproduced the area spanning from the glacier to the Seracchi Lake, so only a portion of them was used for this work, cutting the orthophoto and the DEM in GIS environment so to extract only the region of Marginale Lake.

For the 2023's dataset, 4220 images were aligned. Even if the area of survey is smaller with respect to 2021, covering only the outwash plain of Marginale Lake, the number of pictures results higher since they include not only RGB images, but also R, G, RE and NIR ones. So, during the flight, for each location, the drone took contemporarily 5 photos, one for each sensor. Then, it results that the 4220 photos correspond to 844 sets of 5 images of the same frame. When uploading the images on Metashape, selecting the option "Multiple-camera system", it is able to recognize the multispectral nature of the images. The workflow for multispectral imagery processing does not change from the standard workflow for RGB photos, apart from an additional step where the primary channel can be selected after adding the images to the project, that for this work was the RGB one, being the sharpest and most detailed. Then, the following processing steps (Align photos, manual collimation of GCPs, Build Dense Cloud, Build DEM, Build Orthomosaic) are performed based on the primary channel. All spectral bands are processed together to create a multispectral orthomosaic that retains the same channels as the source images when exporting the orthomosaic (Agisoft Metashape User Manual - Professional Edition, Version 1.8).

In this case, five GCPs were used in the collimation step. As for 2021's dataset, the residual errors of both cameras and GCPs are shown below.

Table 4.3 Average camera location error on drone model 18th July 2023. Multispectral imagery.

X error [cm]	Y error [cm]	Z error [cm]	XY error [cm]	TOT error [cm]
16.532	13.388	9.962	21.273	23.490

Table 4.4 Residual errors on GCPs drone model 18th July 2023. Multispectral imagery.

N. Points	X error [cm]	Y error [cm]	Z error [cm]	XY error [cm]	TOT error [cm]
5	20.793	12.996	76.630	24.521	80.478

Being the precision of both camera and GCPs alignment quite low, another processing was performed considering only the RGB photos, which allowed better results. For this reason, as Metashape allows to build the orthomosaic from an imported DEM, the final multispectral orthomosaic was built on the DEM generated from the RGB images of 2023 dataset. Nevertheless, the orthomosaic of 2023 was still less accurate compared to that of 2021. Below, the residual errors of the only-RGB project are in tables 4.5 and 4.6.

Table 4.5 Average camera location error on drone model 18th July 2023. RGB imagery.

X error [cm]	Y error [cm]	Z error [cm]	XY error [cm]	TOT error [cm]
2.077	2.1454	4.284	2.986	5.222

Table 4.6 Residual errors on GCPs drone model 18th July 2023. RGB imagery.

N. Points	X error [cm]	Y error [cm]	Z error [cm]	XY error [cm]	TOT error [cm]
5	5.074	5.521	6.097	7.498	9.664

The final DEMs of 2021 and 2023 datasets were used to retrieve water depth in some points of the area of interest, while the orthomosaics were used to extract the digital numbers (DN) to create the model inputs.

4.1.2 GPS Measurements and Water Depth Estimation

This study used the GNSS receiver Trimble SP80 for the positioning of the GCPs but also of some points on the streambed along several cross-sections along the alluvial channels, which is shown in Figure 4.5. In 2021, 100 points were measured (Figure 4.7), while in 2023, 595 points positions were collected (Figure 4.8), both in RTK. The accuracy provided by this coordinate measurement method is centimetric, around 0.03 m.

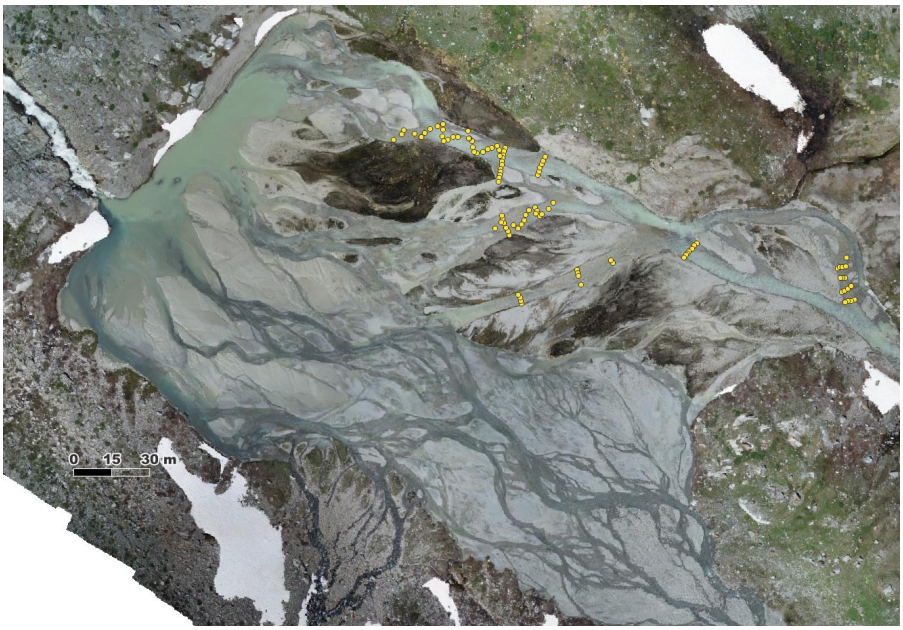

Figure 4.7 GPS measurements (yellow dots) on the orthophoto of Marginale Lake produced from UAV flight of July 2021.

The measured data were used to estimate the water depth along those sections of the streams. In 2021, the water free-surface height was calculated as the average altitude of two points on opposite sides of the river section. This altitude was read from the DEM generated from the UAV flight. Then, the water depth at each of the 100 sampled points was retrieved subtracting the free surface height and the measured streambed altitude.

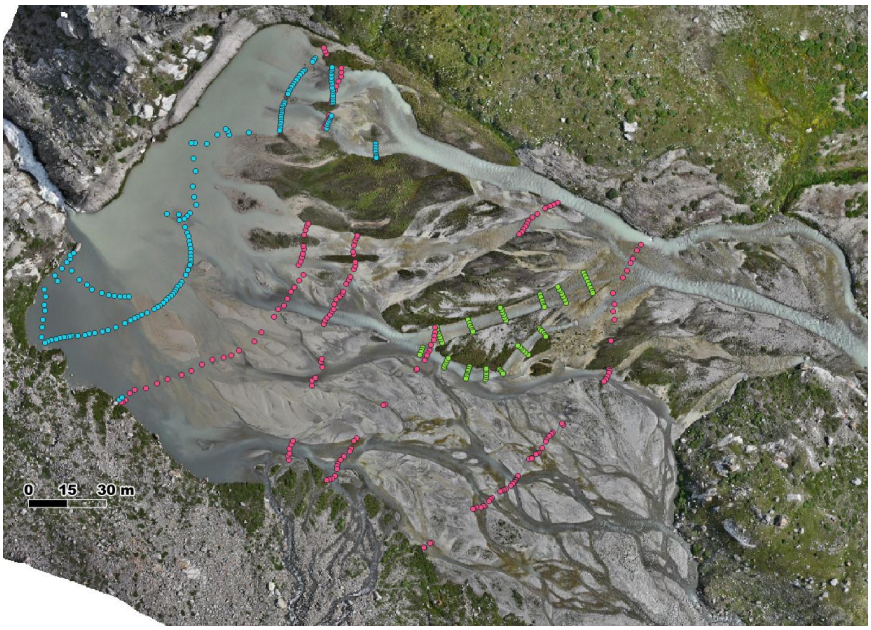

Figure 4.8 GPS measurements on the orthophoto of Marginale Lake produced from RGB imagery of UAV flight of July 2023. Different coloured dots indicate different measurement times: blue dots were sampled in June 2023, magenta in July 2023, and green in September 2023.

Instead, for 2023, water depth was measured directly in the field, together with the point position, for most of the sample. So, the DEM was used to retrieve water depth only for a few points. In particular, the depth of points measured during June and September campaigns was retrieved as for the 2021 dataset, while during the July expedition a metre was installed on the pole of the receiver and the depth read on the metre was recorded simultaneously to the position. Afterwards, a constant value corresponding to the height of the tip of the pole was add to each measure (Figure 4.9).

Figure 4.9 Measurement of the depth of points in July expedition.

In the further processes of this work, the estimated water depth data were all considered as observed data for the construction of the bathymetric inversion model.

4.2 Selection of Model Inputs through PCA

In the process of retrieving bathymetry from multispectral imagery, it is a common practice to use the natural logarithmic values of the band ratios of two spectral bands as suitable estimators for water depth (Stumpf et al., 2003; Legleiter et al., 2009; Legleiter, 2013). Accordingly, this study also employed RGB and multispectral band ratios as input variables for the bathymetric inversion model. In particular, two GWR models were tested for both the 2021 and 2023 datasets: a simple linear GWR model (GWR1) with one band ratio input and a multiple linear GWR model (GWR2) with two band ratio inputs.

To compute the band ratios, the digital number (DN) values were used. The imagery captured in 2021 is in 8-bit format, so their DN values range from 0 to 255, instead 2023's are 16-bit images so DN range from 0 to 65535.

To identify the most suitable band ratios from the numerous possible combinations of bands, this study applied the principal component analysis (PCA). This dimension reduction technique effectively reduces a large set of correlated data to a smaller set of uncorrelated data by removing the multicollinearity that can reduce the precision of estimated parameters in regression models (Aguilera et al., 2006). PCA calculates new variables known as principal components, or also axes or factors, through the eigenvalue decomposition of a data covariance matrix. The first principal component (PC1) is characterized by the highest variance, and the second principal component (PC2), has the second-highest variance and is orthogonal to PC1.

The PC analysis was performed using the Excel tool XLSTAT, which allows to analyse the correlation between the input variables by selecting different approaches: here the Pearson PCA type was selected, that is the traditional PCA, where data is standardized or normalized before calculations, so to prevent the undue influence of variables with high variances on the result. The PC analysis results are shown below, firstly for the 2021's dataset, and then for the 2023's dataset.

2021 RGB imagery

Following the PC analysis, it was observed that $\ln(DN_B/DN_R)$ exhibited a strong correlation with PC1, accounting for 69% of the overall variance across all six band ratios, as outlined in Table 4.7. Conversely, $\ln(DN_G/DN_B)$ demonstrated a positive correlation with PC2, which was entirely uncorrelated with PC1, explaining 31% of the total variance.

Table 4.7 Correlation between band ratios and principal components, 2021 dataset.

	PC1 (69%)	PC2 (31%)
ln(R/G)	-0.782	-0.624
ln(R/B)	-1.000	-0.011
ln(G/R)	0.782	0.624
ln(G/B)	-0.678	**0.735**
ln(B/R)	**1.000**	0.011
ln(B/G)	0.678	-0.735

Consequently, in order to construct both the single and multiple linear GWR models (GWR1 and GWR2, respectively), $\ln(DN_B/DN_R)$ and $\ln(DN_G/DN_B)$ emerged as potential candidates for input variables in the bathymetric inversion models for 2021 dataset.

Therefore, both band ratios were selected as input variables for the multiple linear GWR model (GWR2). Instead, for building the single linear regression model (GWR1) that only uses one spectral input, one of the two band ratios was chosen. To determine which band ratio to use, the methodology outlined by Kim et al. (2019) was followed, which consists of selecting the band ratio that shows the highest correlation to water depth.

This study revealed (Table 4.8) that the most correlated band ratio was $\ln(DN_B/DN_R)$, with a correlation coefficient (ρ) to water depth of 0.64, while $\ln(DN_G/DN_B)$ was found to be less sensitive to changes in water depth, as depicted in Figure 4.10. To identify the statistical significance of these correlations, the corresponding p-values were computed, too. Both band ratios had a p-value less than the significance level of 0.05, indicating rejection of the null hypothesis of no correlation between the variables and water depth.

The higher correlation between $\ln(DN_B/DN_R)$ and the observed water depth can be attributed to the radiative transfer characteristics of the red band, which are highly sensitive to changes in water depth due to the significant light absorption by pure water. In contrast, the blue band is more related to the spectral properties of bottom types and the water column. In aquatic environments, the red band typically experiences greater light absorption compared to the blue-green bands, which instead have higher reflectance, leading to an increase in $\ln(DN_B/DN_R)$ with rising water depth (Legleiter, 2013).

Therefore, $\ln(DN_B/DN_R)$ was considered as the sole input variable for the bathymetric inversion model GWR1.

Table 4.8 Correlation between PCA-selected band ratios and observed water depth, 2021 dataset.

	ρ	p-value
ln(B/R)	0.648	0.000
ln(G/B)	-0.324	0.001

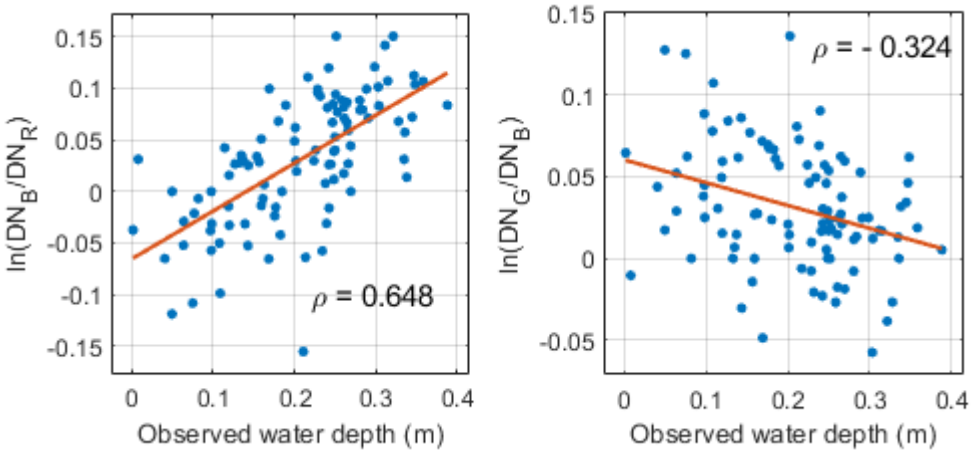

Figure 4.10 Response of PCA-selected band ratios, $\ln(DN_B/DN_R)$ on the left and $\ln(DN_G/DN_B)$ on the right, to observed water depth. The orange line indicates a fitting line to observation. 2021 dataset.

2023 imagery

The DNs to compute the band ratios for 2023's dataset were extracted from the two orthomosaics generated and previously mentioned: the RGB one (which had a better accuracy) and the multispectral one.

- For the RGB case, as for the 2021 dataset, six variables were to be submitted to PCA, which are all the natural logarithms of all the possible combinations between the three bands RGB (8-bit images).
- For the multispectral case, eighteen variables were submitted to PCA, which are all the natural logarithms of all the possible combinations between the total seven bands: three bands of the RGB camera, and the four of the multispectral sensor, G, R, RE, NIR. (16-bit images).

RGB only

The PCA analysis revealed that the ratio of $\ln(DN_B/DN_R)$ was strongly correlated with PC1, explaining 83% of the total variance of all six band ratios listed in Table 4.9. On the other hand, $\ln(DN_R/DN_G)$ had the strongest positive correlation with PC2, which was orthogonal to PC1, and accounts for 17% of the total variance. Therefore, $\ln(DN_B/DN_R)$ and $\ln(DN_R/DN_G)$ are potential input variables for the bathymetric inversion models.

Table 4.9 Correlation between band ratios and principal components, 2023 dataset (RGB only).

	PC1 (83%)	PC2 (17%)
ln(R/G)	-0.826	**0.564**
ln(R/B)	-0.997	-0.080
ln(G/R)	0.826	-0.564
ln(G/B)	-0.905	-0.426
ln(B/R)	**0.997**	0.080
ln(B/G)	0.905	0.426

In order to build both the single and multiple linear GWR models (GWR1 and GWR2), $\ln(DN_B/DN_R)$ and $\ln(DN_R/DN_G)$ were selected as input variables for the latter. For GWR1, which utilizes a single spectral input, the appropriate band ratio input was chosen among the two variables with the same approach used for 2021's dataset. Subsequently, the correlation between the PCA-selected band ratios and water depth was analysed, as illustrated in Table 4.10 and Figure 4.11. Then, $\ln(DN_R/DN_G)$, showing the highest correlation to water depth, was used as input of GWR1.

Table 4.10 Correlation between PCA-selected band ratios and observed water depth, 2023 dataset (RGB only).

	ρ	p-value
ln(B/R)	0.452	0.135×10^{-21}
ln(R/G)	-0.574	0.000×10^{-21}

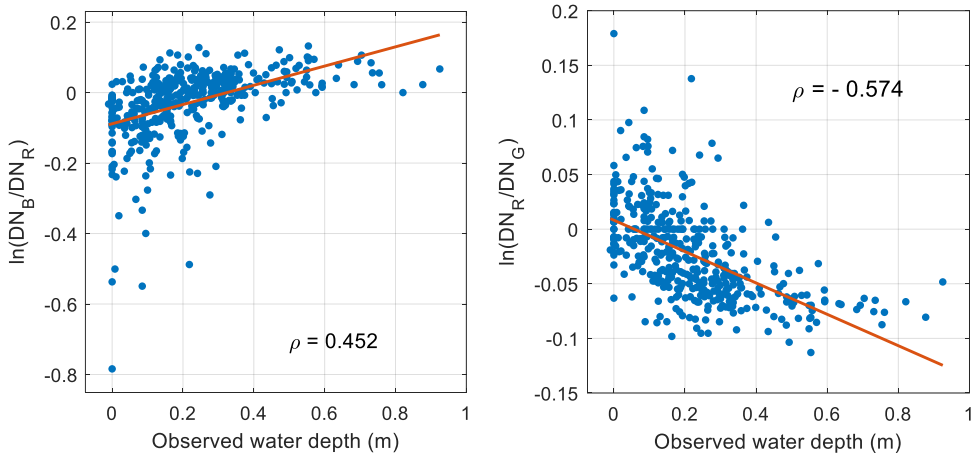

Figure 4.11 Response of PCA-selected band ratios, $\ln(DN_B/DN_R)$ on the left and $\ln(DN_R/DN_G)$ on the right, to observed water depth. The orange line indicates a fitting line to observation. 2023 dataset (RGB only).

Multispectral

In this dataset the number of all possible combinations of the seven bands (RGB, R, G, RE, NIR) is eighteen. As a result of the PCA, $\ln(DN_{NIR}/DN_G)$ was highly correlated to PC1, explaining 65% of the total variance attributed to all eighteen variables, as shown in Table 4.11. Instead, $\ln(DN_G/DN_B)$ had the strongest positive correlation with PC2, perfectly orthogonal to PC1 and accounted for 17% of the total variance. Thus, $\ln(DN_{NIR}/DN_G)$ and $\ln(DN_G/DN_B)$ can be candidates for input variables of the bathymetric inversion models. PC3, PC4 and PC5 were not considered, as each of them represents smaller percentages of the total variance of the set of variables.

Table 4.11 Correlation between band ratios and principal components, 2023 dataset (RGB and multispectral). For an easier visualization, the band ratios obtained from the RGB sensor of the drone are in pink, while those of the multispectral sensor are in grey.

	PC1 (65%)	PC2 (17%)	PC3 (11%)	PC4 (5%)	PC5 (2%)
ln(R/G)	0.711	0.127	0.365	-0.582	0.078
ln(R/B)	0.643	0.762	0.073	0.012	0.020
ln(G/R)	-0.711	-0.127	-0.365	0.582	-0.078
ln(G/B)	0.496	**0.839**	-0.043	0.219	-0.004
ln(B/R)	-0.643	-0.762	-0.073	-0.012	-0.020
ln(B/G)	-0.496	-0.839	0.043	-0.219	0.004
ln(G/R)	-0.389	0.205	-0.856	-0.260	0.081
ln(G/RE)	-0.969	0.154	0.082	0.016	0.175
ln(G/NIR)	-0.971	0.217	0.070	-0.074	-0.020
ln(R/G)	0.389	-0.205	**0.856**	0.260	-0.081
ln(R/RE)	-0.938	0.118	0.272	0.073	0.167
ln(R/NIR)	-0.962	0.200	0.179	-0.045	-0.031
ln(RE/G)	0.969	-0.154	-0.082	-0.016	-0.175
ln(RE/R)	0.938	-0.118	-0.272	-0.073	-0.167
ln(RE/NIR)	-0.902	0.280	0.050	-0.184	-0.268
ln(NIR/G)	**0.971**	-0.217	-0.070	0.074	0.020
ln(NIR/R)	0.962	-0.200	-0.179	0.045	0.031
ln(NIR/RE)	0.902	-0.280	-0.050	0.184	0.268

To decide which of the two bands was the best input for the single linear regression GWR1, the most correlated with the observed water depth was found: the result showed that change in water depth was more sensitive to $\ln(DN_{NIR}/DN_G)$ (Table 4.12 and Figure 4.12).

Table 4.12 Correlation between PCA-selected band ratios and observed water depth, 2023 dataset (RGB and multispectral).

	ρ	p-value
ln(NIR/G)	-0.541	0.000×10^{-3}
ln(G/B)	-0.170	0.459×10^{-3}

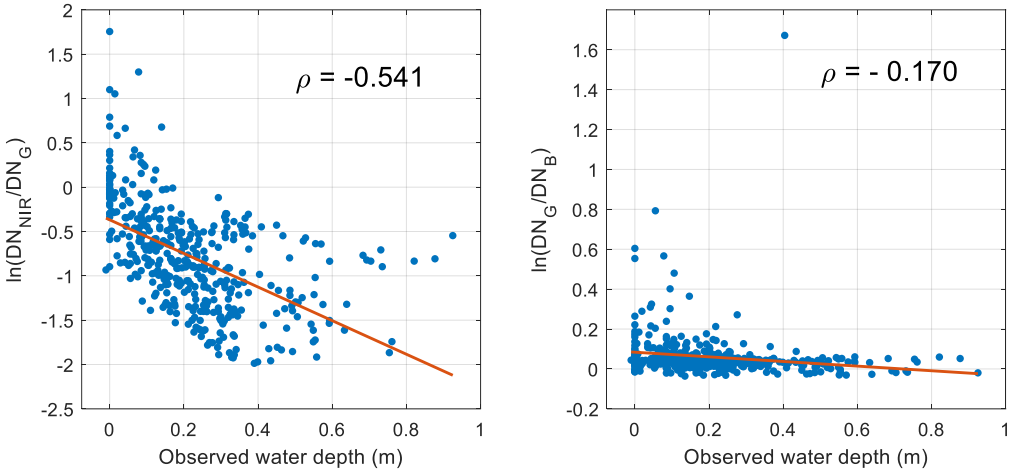

Figure 4.12 Response of PCA-selected band ratios, $\ln(DN_{NIR}/DN_G)$ on the left and $\ln(DN_G/DN_B)$ on the right, to observed water depth. The orange line indicates a fitting line to observation. 2023 dataset (RGB and multispectral).

4.3 GWR Model

The relationship between the PCA-selected band ratios and water depth was analysed using two types of GWR methods, as previously mentioned: firstly, a simple linear regression model (GWR1), using a single input (the most correlated band ratio) and then a multiple linear regression model (GWR2), using both band ratios.

The geographically weighted regression model has the capability to capture the spatially heterogeneous relationships between the spectral input of the model, and its output, the water depth, which is induced by the inhomogeneous streambed. This is allowed thanks to the parameters of the model that are functions of the spatial locations (Fotheringhamet al., 1998).

Simple linear GWR (GWR1)

Based on Kim et al. (2019), the equation used to build the first type of GWR model (GWR1), which is a simple linear regression, is the following:

$$\hat{h}_i = \alpha_i X_i + b_i \tag{2}$$

where $\hat{h}_i$ is the estimated water depth, α_i is the local regression coefficient at i, which accounts for geographical characteristics inherent to locations. Instead, X_i represents the single spectral input of the model, selected as the most correlated to water depth among the PCA-selected band ratios, as described in the previous paragraph. It is the value of the natural logarithm of the band ratio at the location i. Finally, b_i is the bias at i point. For this study, b_i was disregarded, as a first approximation.

Here in, i indicates the regression point equivalent to the observation point. In fact, this model was calibrated on the field-measured points of known coordinates and depths. The aim was to estimate the model parameters and then interpolate them all over the area of the lake, also where water depth was unknown. The local regression

coefficients, for all the i known points, were determined using weighted least squares and can be written as a vector:

$$\alpha(i) = (X^T W(i) X)^{-1}\ X^T W(i) \hat{h}(i) \quad (3)$$

where $\alpha(i)$ is the vector of estimated values for α_i; X is the vector of natural logarithm of the band ratio selected as input; $W(i)$ is the diagonal matrix representing the geographical weighting factor of $\hat{h}_i$; and $\hat{h}(i)$ is the single column vector of $\hat{h}_i$. In equation (3), $W(i)$ contains the weights of the model, w_{ij}, estimated by the bi-square kernel function:

$$w_{ij} = \left[1 - \left(\frac{d_{ij}^2}{b_{krn}^2}\right)\right]^2 , \text{if } b_{krn} \geq d_{ij}$$

$$w_{ij} = 0 \text{ , otherwise} \quad (4)$$

where b_{krn} is the kernel bandwidth that can be optimized by minimizing the sum of squared errors defined in Eq. (5); j is the observation point other than i within b_{krn}; and d_{ij} is the distance between i and j (Kim et al., 2019).

$$SSE = \sum_{i=1}^{n} (h_i - \hat{h}_i)^2 \quad (5)$$

Multiple linear GWR (GWR2)

To build the second type of GWR model tested (GWR2), a multiple linear regression was used, based on the equation (2):

$$\hat{h}_i = \alpha_i(1) X_i(1) + \alpha_i(2) X_i(2) + b_i \quad (6)$$

where $\alpha_i(1)$ and $\alpha_i(2)$ are the local regression coefficients at i respectively for the variables $X_i(1)$ and $X_i(2)$ at i, which are the two PCA-selected band ratios. As for Eq. (2), b_i is the bias at i point, which was disregarded for this study.

The model works exactly as (2) except for the fact that two input variables are used. For this reason, the Eq. (3), (4) and (5) are also valid for this model.

For this study, both models were implemented on the software MATLAB and QGIS[3], respectively for the calibration and the prediction steps of the model. The calibration phase allowed to estimate the model parameters α_i for the known i points, and then, using QGIS, to interpolate them all over the area of the lake, so to predict water depth where it was unknown.

[3] mathworks.com and qgis.org, respectively.

4.4 Model Calibration

The calibration of the model in MATLAB was based on field-measured points with known depth. In the 2021 dataset, all 100 measured points were utilized. For the 2023 dataset, which was sufficiently large, the model was calibrated using 70% of the total dataset, specifically 422 randomly selected points. The remaining 30% (173 points) were used for model validation.

The main goal of the calibration step was to retrieve the coefficients α_i for the known i points.

The MATLAB code was developed based on that written by Ning Liu (2023). The inputs of the code were:

- a two-column matrix, containing the east and north coordinates of the i known points.
- a single column vector containing the known depth values for the i points.
- a single column vector of the one PCA-selected band ratio for the simple linear GWR1, or a two-column matrix of both band ratios for the multiple linear GWR2, computed for the i points.

The outputs of the code were:

- the model parameters α_i estimated for the known i points.
- the model performance criteria: the scatter plot of estimated depths versus the observed one for the i points, and R^2 and RSR statistical indexes. R^2 is the coefficient of determination and was used to assess the goodness of fit of the regression model. It ranges from 0 to 1, the closer the value is to 1, the better the model performance. Instead, the zero value denotes poor fitting. Finally, the RSR is the Root Mean Standard Deviation Ratio and normalizes the Root Mean Squared Error (RMSE) by the standard deviation of the observation data. It varies from an optimal value of 0 to infinity. According to Moriasi et al. (2007), RSR provides performance rankings as: very good (0-0.50), good (0.50-0.60), satisfactory (0.60-0.70), and unsatisfactory (>0.70). The formulas applied to compute R^2 and RSR are the following:

$$R^2 = \frac{\sum_{i=1}^{n}(h_i - \hat{h}_i)^2}{\sum_{i=1}^{n}(h_i - \bar{h}_i)^2} \tag{7}$$

$$RSR = \frac{\sqrt{\sum_{i=1}^{n}(h_i - \hat{h}_i)^2}}{\sqrt{\sum_{i=1}^{n}(h_i - \bar{h}_i)^2}} \tag{8}$$

The outputs of this calibration phase are illustrated hereafter, firstly for the 2021's dataset, and then for the 2023's dataset. As mentioned before, two GWR models were calibrated for each dataset and are shown below, beginning with the simple linear GWR model (GWR1) with one band ratio input and the multiple linear GWR model (GWR2) with two band ratio inputs.

2021 RGB Imagery

The 2021 dataset of measured depth was too small to consider calibrating the model only over a portion of it, and using the remaining data for validation: so the calibration was carried out over the 100-field measured points.

The results of model calibration for 2021's dataset are shown in Figure 4.13 and Table 4.13. According to the correlation analysis illustrated in the previous paragraph (Table 4.8 and Figure 4.10), $\ln(DN_B/DN_R)$ resulted to be more correlated to water depth so the ideal candidate for the simple linear regression GWR1. However, considering only this spectral input, the model performances are not acceptable: the comparison of observed water depth and estimated one results in a sparse scatter plot, with low R^2. Moreover, 28 out of 100 estimated depths are negative values, which is physically unfeasible. Instead, when considering both PCA-selected band ratios, $\ln(DN_B/DN_R)$ and $\ln(DN_G/DN_B)$, the number of negative estimations decreased to 7 out of 100, the cloud was denser and the R^2 index increased from 0.48 to 0.77. Instead, RSR exhibited only a slight improvement, still not satisfactory, reducing from 1.89 to 1.26.

In conclusion, the GWR2 resulted in the best model to exploit in the bathymetry retrieving.

Table 4.13 Accuracy of GWR models in estimating water depth. 2021 dataset.

	Input	R^2	RSR	Negative values
GWR1	**ln(B/R)**	0.475	1.894	28/100
GWR2	**ln(B/R) and ln(G/B)**	0.769	1.257	7/100

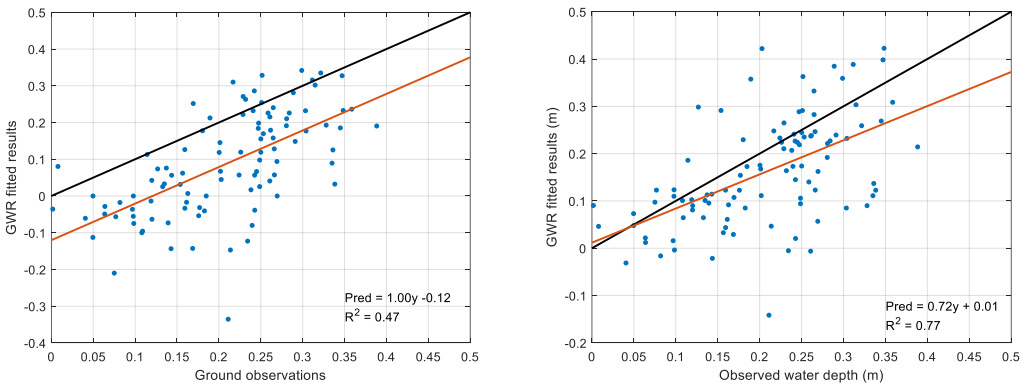

Figure 4.13 Comparison between observed water depth and estimated water depth using the simple linear GWR model (GWR1) (on the left) and the multiple linear GWR (GWR2) (on the right). The black line indicates a linear line passing through the origin, while the orange line is a fitting line to estimations, represented by the formula in the graph. 2021 dataset.

2023 RGB and Multispectral Imagery

For the 2023 dataset, the calibration of the models was performed with 70% of the total data, precisely 422 randomly chosen data points. The remaining 30%, comprising 173 points, were reserved for model validation.

RGB only

Based on the correlation analysis (Table 4.10 and Figure 4.11), $\ln(DN_R/DN_G)$ is the most correlated band ratio with water depth and is the best option for the simple linear regression GWR1. However, when considering both PCA-selected band ratios, $\ln(DN_B/DN_R)$ and $\ln(DN_R/DN_G)$, the model improved: the plot of observed depth versus estimated one became denser, the number of negative values estimates decreased from 77 to 32 out of 422, and the performance measures R^2 and RSR improved (Table 4.14).

Table 4.14 Accuracy of GWR models in estimating water depth. 2023 dataset (RGB only).

	Input	R^2	RSR	Negative values
GWR1	**ln(R/G)**	0.790	0.750	77/422
GWR2	**ln(B/R) and ln(R/G)**	0.873	0.583	32/422

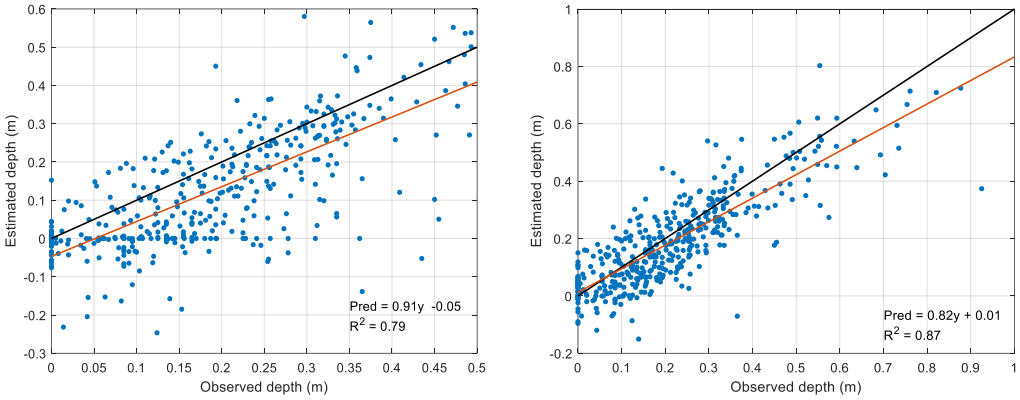

Figure 4.14 Comparison between observed water depth and estimated water depth using the simple linear GWR model (GWR1) (on the left) and the multiple linear GWR (GWR2) (on the right). The black line indicates a linear line passing through the origin, while the orange line is a fitting line to estimations, represented by the formula in the graph. 2023 dataset (RGB only).

Multispectral

According to the correlation analysis (Table 4.12 and Figure 4.12), $\ln(DN_{NIR}/DN_G)$ was selected as the single spectral input for the simple linear regression GWR1. However, when only this input is considered, the model goodness is lower compared to when both PCA-selected band ratios are used. In fact, when considering both $\ln(DN_{NIR}/DN_G)$ and $\ln(DN_G/DN_B)$, the plot of observed depth versus estimated one became denser,

the number of negative values estimates decreased from 33 to 22 out of 422, and the performance measures R^2 and RSR showed modest but good improvements (Table 4.15). Then, also in this case, the multiple linear regression was more efficient in reproducing the spectral-depth relationship.

Table 4.15 Accuracy of GWR models in estimating water depth. 2023 dataset (RGB and multispectral).

	Input	R^2	RSR	Negative values
GWR1	**ln(NIR/G)**	0.895	0.530	33/422
GWR2	**ln(NIR/G) and ln(G/B)**	0.937	0.410	22/422

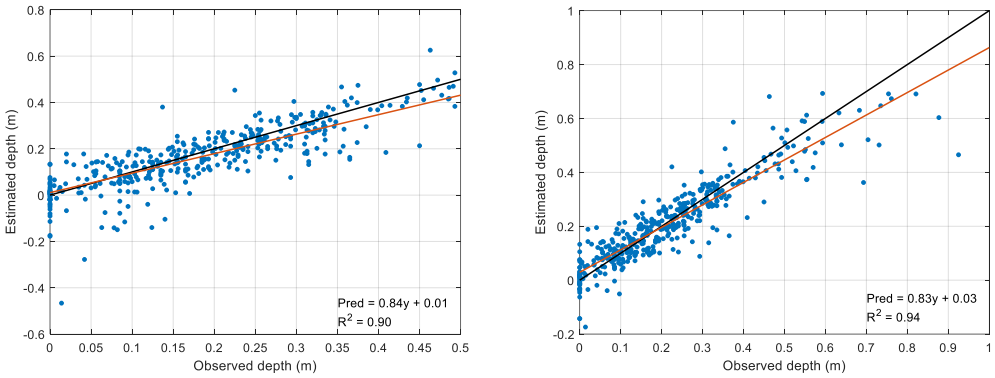

Figure 4.15 Comparison between observed water depth and estimated water depth using the simple linear GWR model (GWR1) (on the left) and the multiple linear GWR (GWR2) (on the right). The black line indicates a linear line passing through the origin, while the orange line is a fitting line to estimations, represented by the formula in the graph. 2023 dataset (RGB and multispectral).

Finally, to select only one final model for the 2023 dataset, multispectral-based and RGB-based models were compared. According to the results of R^2 and RSR (Tables 4.14 and 4.15), and Figures 4.14 and 4.15, the models built based on the multispectral imagery exhibit better performances compared to those based only on the RGB imagery. Particularly, the multispectral GWR2 significantly reduced the discrepancy between the model and the observations, mitigating the deviations from the perfect linear line with respect to the RGB GWR2 model. In comparison to the results obtained from this latter model, the estimation accuracy was greatly enhanced. Specifically, the RSR value decreased from 0.583 to 0.410; and the R-squared value increased from 0.873 to 0.937. Consequently, the GWR2 of the multispectral dataset was used to retrieve the 2023's bathymetry.

4.5 Model Prediction

In the prediction step, the water depth was estimated for all points outside the calibration domain, all over the Marginale Lake area. Recalling the generalized formula of the model used,

$$\hat{h}_j = \alpha_j(1)X_j(1) + \alpha_j(2)X_j(2) + b_j \quad (9)$$

$\hat{h}_j$ is the value to retrieve for a generic unmeasured or uncalibrated j point; X_j are the spectral inputs available all over the area, thanks to the orthomosaic; b_j is disregarded. Then, the unknown parameters are the α_j at all the uncalibrated j points of the area of interest. To estimate these coefficients, the Inverse Distance Weighting (IDW) was employed, using QGIS software, that interpolated the α_i coefficients calculated in the calibration step for the known i points.

Once obtained the GWR parameters, the equation (9) was applied using the "Raster calculator" tool of QGIS and the final output produced was the bathymetry estimation all over the Marginale Lake.

This procedure was applied for the models that during the calibration phase showed the best performance for each dataset:

- For the 2021's dataset, the bathymetry was retrieved using the multiple linear type of the GWR model (GWR2), with $\ln(DN_B/DN_R)$ and $\ln(DN_G/DN_B)$ as input band ratios.
- For the 2023, the entire multispectral dataset was used, resulting better than using only RGB, and the bathymetry was retrieved using the multiple linear type of the GWR model (GWR2), with $\ln(DN_{NIR}/DN_G)$ and $\ln(DN_G/DN_B)$ as spectral inputs.

5. Results and Discussion

At the end of the procedure exposed in Chapter 4, bathymetry estimation all over the Marginale Lake was retrieved for both years studied, reproducing the site morphology of summer 2021 and 2023.
In 2021, bathymetry was obtained using the multiple linear model GWR2, with the PCA-derived band ratios $\ln(DN_B/DN_R)$ and $\ln(DN_G/DN_B)$. For 2023, the bathymetry was retrieved using the multispectral GWR2 model, with spectral inputs $\ln(DN_{NIR}/DN_G)$ and $\ln(DN_G/DN_B)$.

5.1 2021 Results

Figure 5.1 illustrates the streams and lake bathymetry retrieved by the model. The data indicates that the majority of the area has a depth of 0 to 0.5 meters, which matches the expectations from the field campaign as walking across the streams was possible. This is more distinctively elucidated in the histogram in Figure 5.2, according to which the most frequent depth is around 0.25 m. Deeper water is on the left side of the streams and lake and near the outflowing cascade, confirming also in this case the experience on the field. This is due to a topographic barrier that makes water to accumulate and flow downstream through a single channel.

Basic statistics of the bathymetry obtained show a mean value of water depth of 0.22 m. Minimum and maximum values, respectively of - 1.03 and 2.39 m, indicate model biases, being negative values physically unfeasible and the lake generally shallower than about 1 m. However, these biases remained quite contained to a few pixels (Figure 5.1) and to low frequency of occurrence, as for the histogram. According to this latter graph, model biases were mostly related to negative estimated depth.

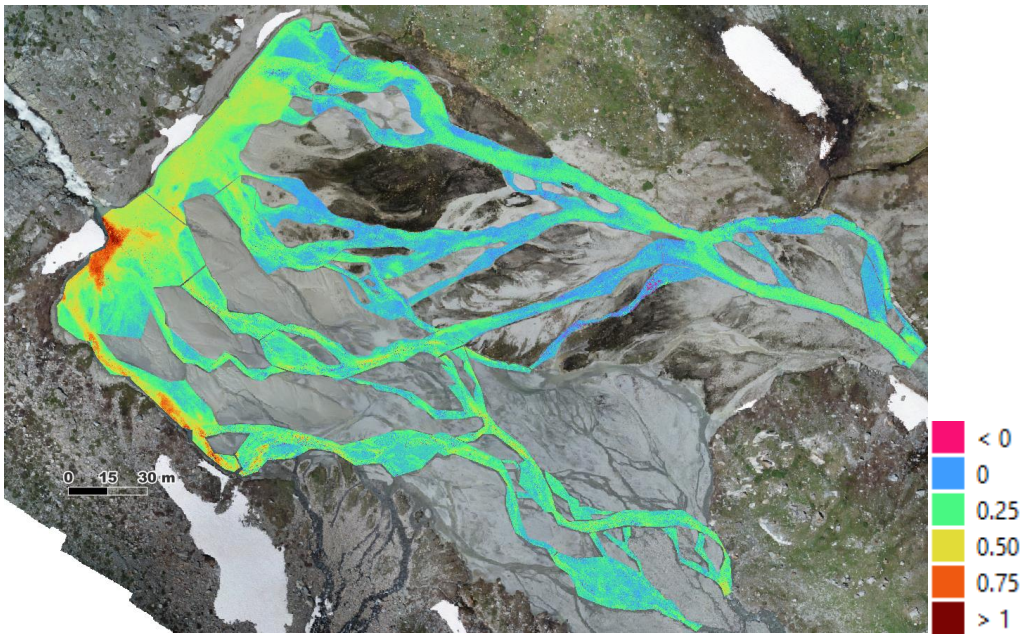

Figure 5.1 Spatial distribution of water depth estimated by the GWR model. Legenda: estimated depth (m). 2021 dataset.

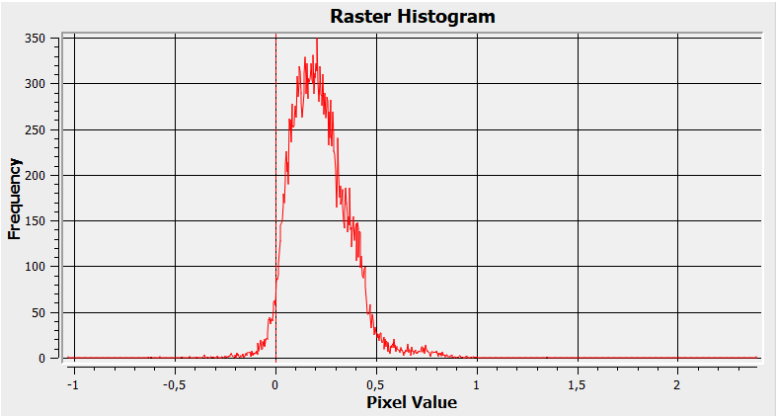

Mean	0.22 m
σ	0.14 m
Minimum	-1.03 m
Maximum	2.39 m

Figure 5.2 Frequency histogram of the water depth estimated by the GWR model and basic statistics. 2021 dataset.

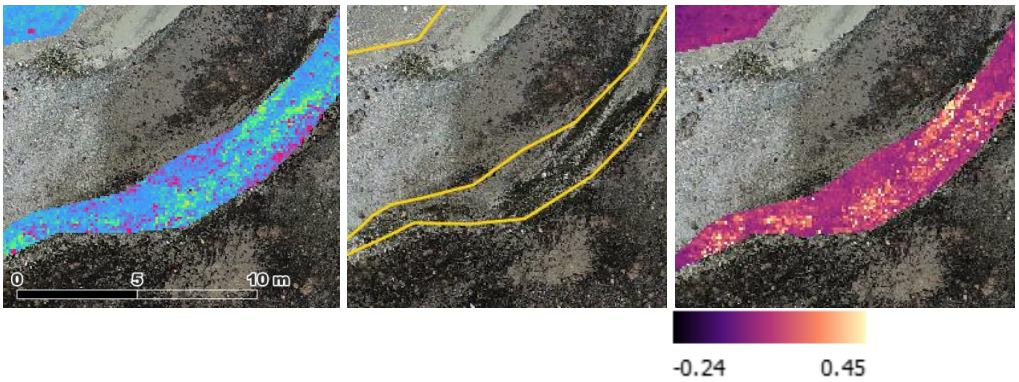

Figure 5.3 Detail of the GWR model (on the left), orthomosaic (centre) and the spatial distribution of $\ln(DN_G/DN_B)$ (on the right).

Based on Figure 5.1, most of the biases related to negative values (magenta and purple pixels) are concentrated along a shallow and narrow stream whose bed is characterized by submerged vegetation. This stream is more distinctively shown in Figure 5.3, where the vegetation cover pictured by the orthomosaic (on the centre) is strongly responding to the spatial distribution of the band ratio $\ln(DN_G/DN_B)$ (on the right), which shows higher values where vegetation is present. In fact, vegetation exhibits higher reflection in the green band and higher absorption in blue, which led to the increase in $\ln(DN_G/DN_B)$ values not directly associated with change in water depth and thus to model bias (magenta and purple pixels in the lefthand image).

Finally, Figures 5.4 and 5.5 show the spatial distribution over the area of the regression coefficients α_j and of the spectral inputs $\ln(DN_B/DN_R)$ and $\ln(DN_G/DN_B)$, respectively.

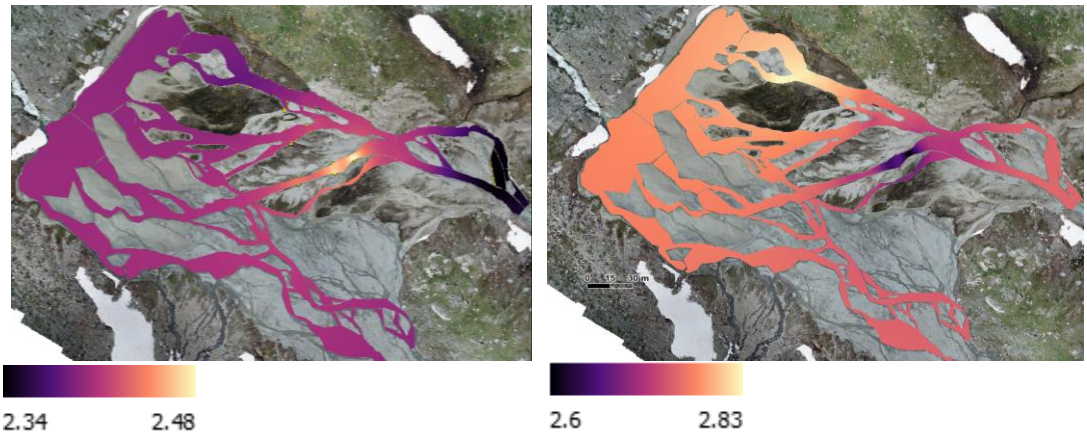

Figure 5.4 Spatial distribution of the regression coefficient $\alpha_j(1)$ (left) and $\alpha_j(2)$ (right) interpolated by IDW. 2021 dataset.

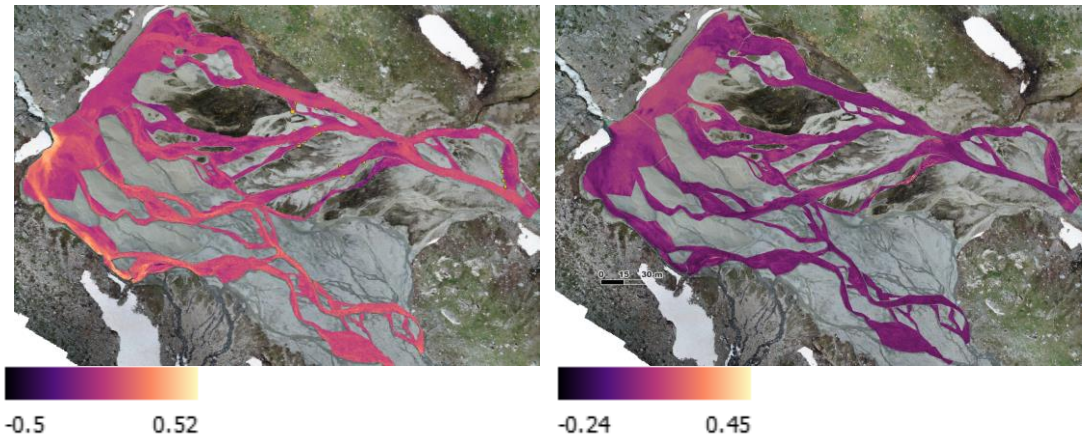

Figure 5.5 Spatial distribution of $\ln(DN_B/DN_R)$ (left) and $\ln(DN_G/DN_B)$ (right). 2021 dataset.

Figure 5.6 represents the frequency of the residuals $h_i - \hat{h}_i$ between observations and estimations of water depth. Considering the total dataset (a), the model's estimation accuracy is good, as there is little deviation from the mean value, which is 0.05 m (for a perfect model it should be zero). A general underestimation trend is exhibited, nevertheless, it is restrained in terms of mean value: in fact, the average residual for $h_i \leq 0.20$ m is 0.02 m, while for $h_i > 0.20$ m is 0.06 m. However, from the point of view of the dispersion of the data, the distribution is quite large, especially for water deeper than 0.20 m, for which residuals up to 0.40 m are recorded.

The underestimation trend is confirmed when examining Figure 5.7. It compares the simulated water depth to the measured one, along two randomly selected cross-sections. Section 2 has a depth ranging from 0 to around 0.20 m, and is shallower than Section 1, which instead goes up to 0.35 m. As illustrated by the figure, the shallower section has smaller residuals, of the order of 0.10 m, represented by the distance between the two curves, while Section 1 shows a maximum residual of about 0.20 m where it reaches a depth of 0.35 m.

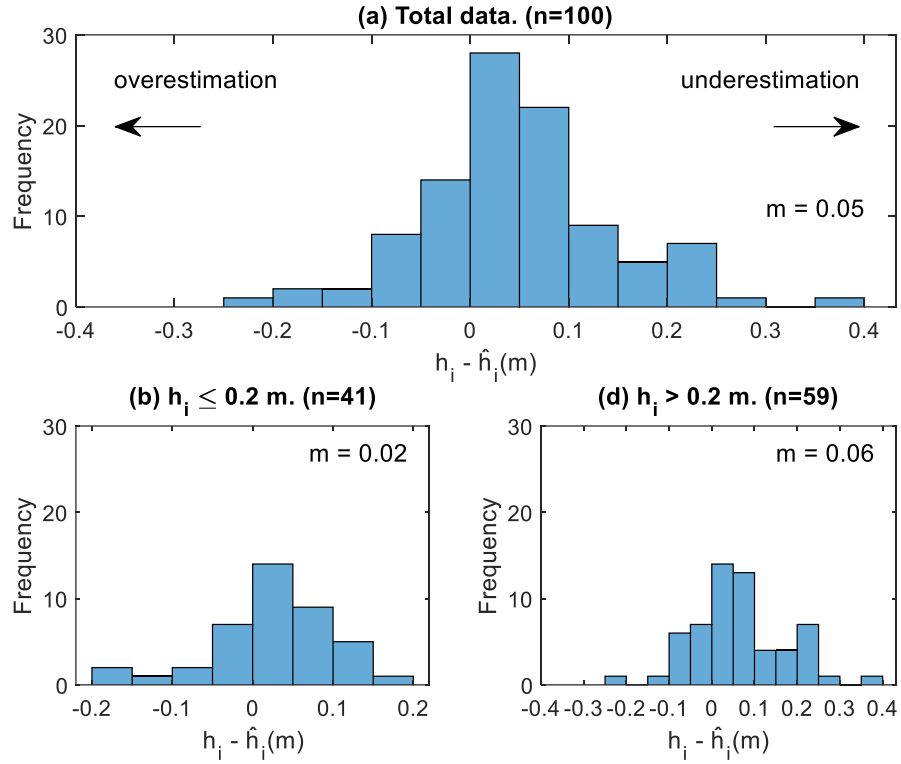

Figure 5.6 Frequency distribution of residuals $h_i - \hat{h}_i$ for different ranges of observed water depth: (a) whole data set, (b) depth shallower than 0.2 m, (c) deeper than 0.2. The *m* in the graph indicates the mean value of the residuals in metres. Bar width of 0.05m. 2021 dataset.

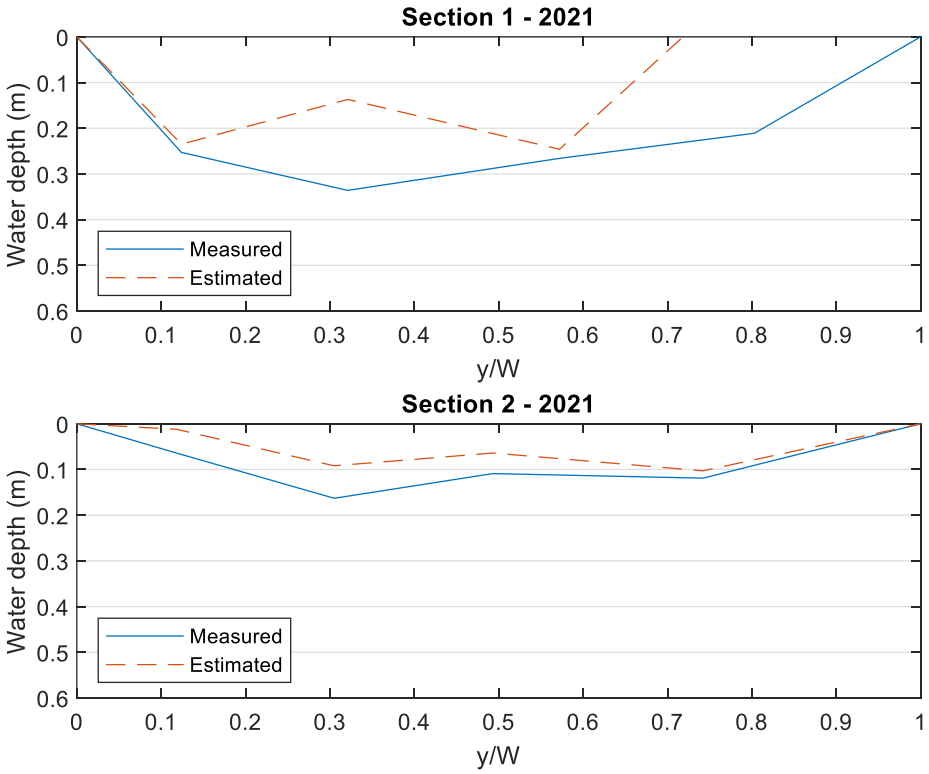

Figure 5.7 Comparison of simulated to measured water depth at two sections. y/W indicates the dimensionless distance from a bank of the section. 2021 dataset.

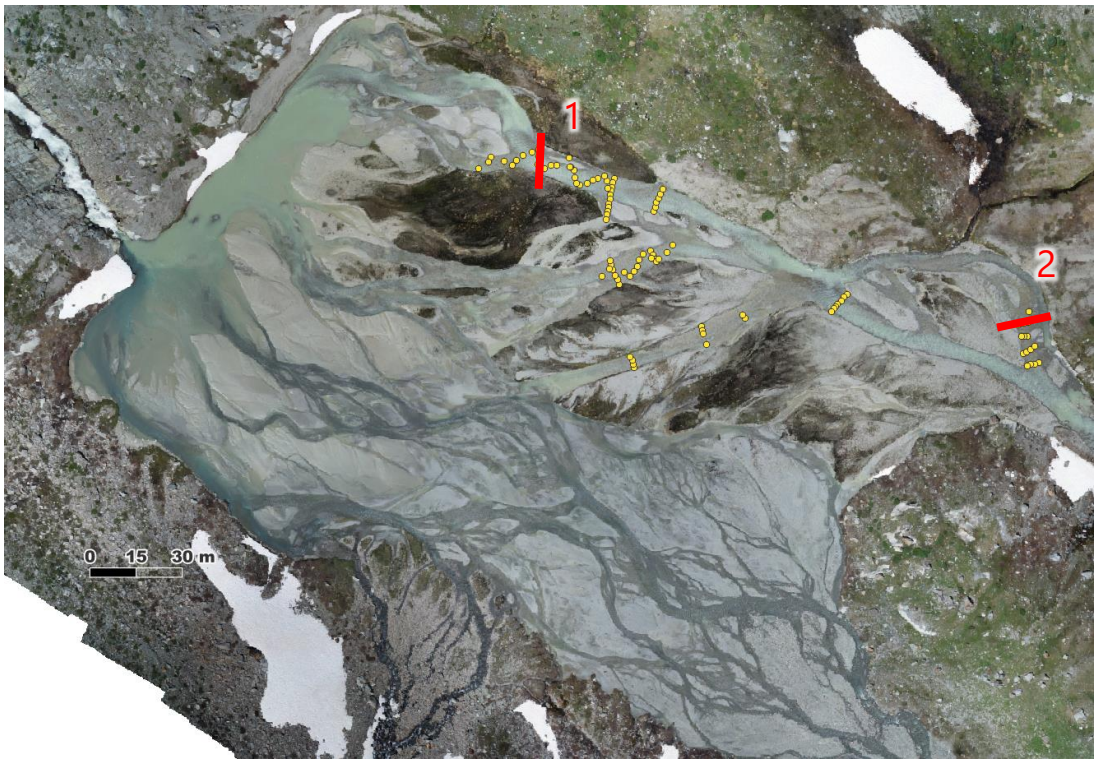

Figure 5.8 Overview of the position of Section 1 and Section 2. 2021 dataset.

One possible explanation of these model biases may be the local changes in the type of bed in the area. Furthermore, the presence of high turbidity resulting from sediment fluxes along the streams could also contribute to increased variability in the water column.

In conclusion, the GWR model generally underestimated the Lake's bathymetry by an average of 0.05 m, being more precise for water shallower than 20 centimetres with respect to deeper one.

Differently from the 2023 case, which will be presented in the following paragraph, the above-mentioned analysis on the residuals could not be carried out as a validation step of the 2021 model. Being the dataset of measured depths small (100 points), it was not possible to divide it into a calibration dataset and a validation dataset. Then, Figures 5.6 and 5.7 were built from the same calibration data. Therefore, they are not presented here as a validation of the model, but they could be considered as an introduction to the procedure used for 2023 model validation.

5.2 2023 Results

The model depicted in Figure 5.9 provides a visual representation of the water depth in the streams and lake retrieved by GWR2 using 2023 multispectral data. The majority of the area has a depth ranging from 0 to 0.40 meters. This is consistent with the field campaign, where it was possible to wade across the streams to get GPS measurements, as for 2021. The histogram in Figure 5.10 further illustrates this, showing that the most common depths are 0.10 m and 0.23 m. Deeper water can be found on the left side of the streams and lake, as well as near the effluent cascade.

Figure 5.10 also displays the basic statistics of the bathymetry. The mean water depth is 0.18 m. The extreme values have a minimum of -0.42 m and a maximum of 1.36 m, which can be considered improved with respect to those of 2021, which are more dispersed. This can be observed by comparing the histograms in Figures 5.2 and 5.10.

Negative values indicate model biases or not submerged areas, but they are limited to a few pixels and occur less frequently than in 2021.

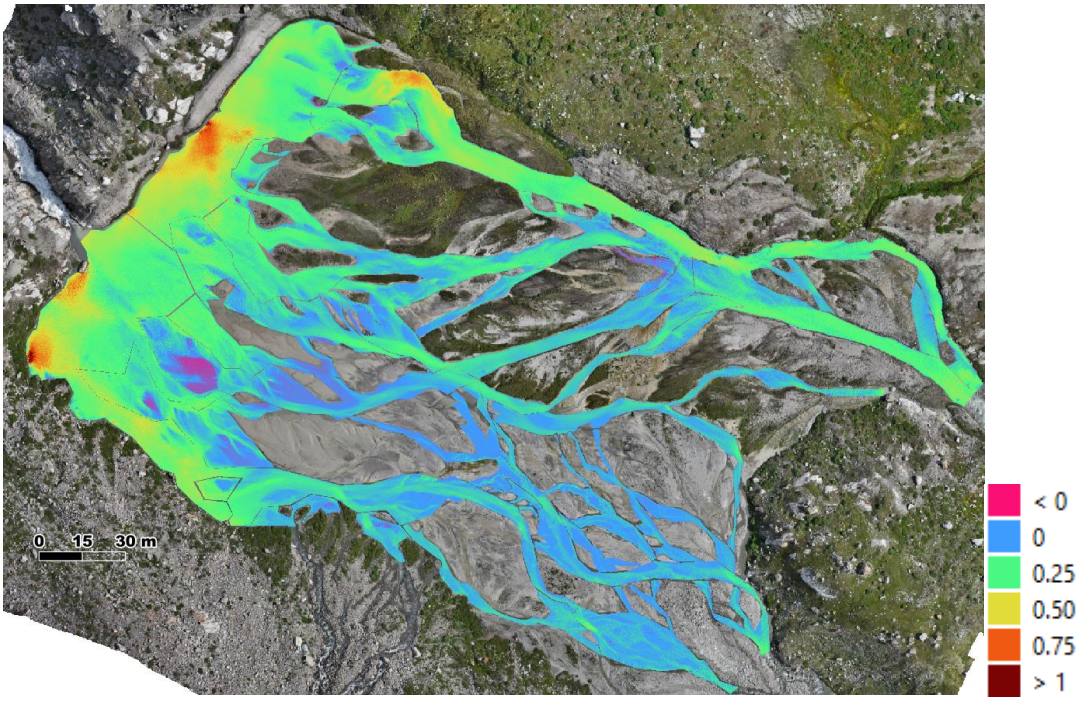

Figure 5.9 Spatial distribution of water depth estimated by the GWR model. Legenda: estimated depth (m). 2023 dataset.

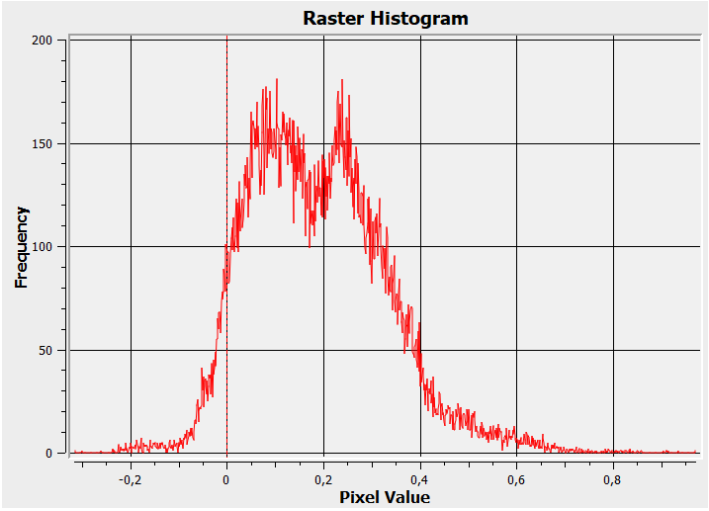

Mean	0.18 m
σ	0.14 m
Minimum	-0.42 m
Maximum	1.36 m

Figure 5.10 Frequency histogram of the water depth estimated by the GWR model and basic statistics. 2023 dataset.

According to the histogram (Figure 5.10), model biases are mostly related to negative estimated depths, which are magenta and purple pixels in Figure 5.9. However, they are concentrated in the highlighted areas (in Figure 5.11), where the boundary between the water layer and the shoreline is indeed unclear or the water is very shallow. Thus, the presence of negative estimated values of depth in those areas does not indicate bias but no presence of water depth at all, as can be better seen from Figure 5.12, which zooms in these highlighted areas.

This fact is also confirmed by studying the spectral response of these areas, which is described in Figure 5.13.

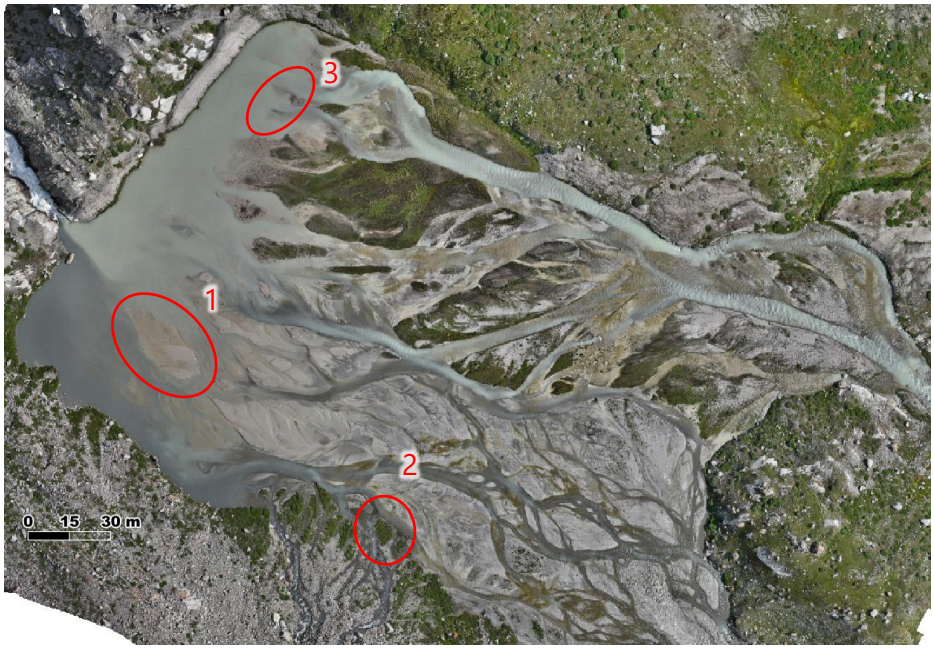

Figure 5.11 Orthophoto from RGB imagery of 2023, with the highlighted areas (1, 2, 3) of the boundary between the water and the shoreline.

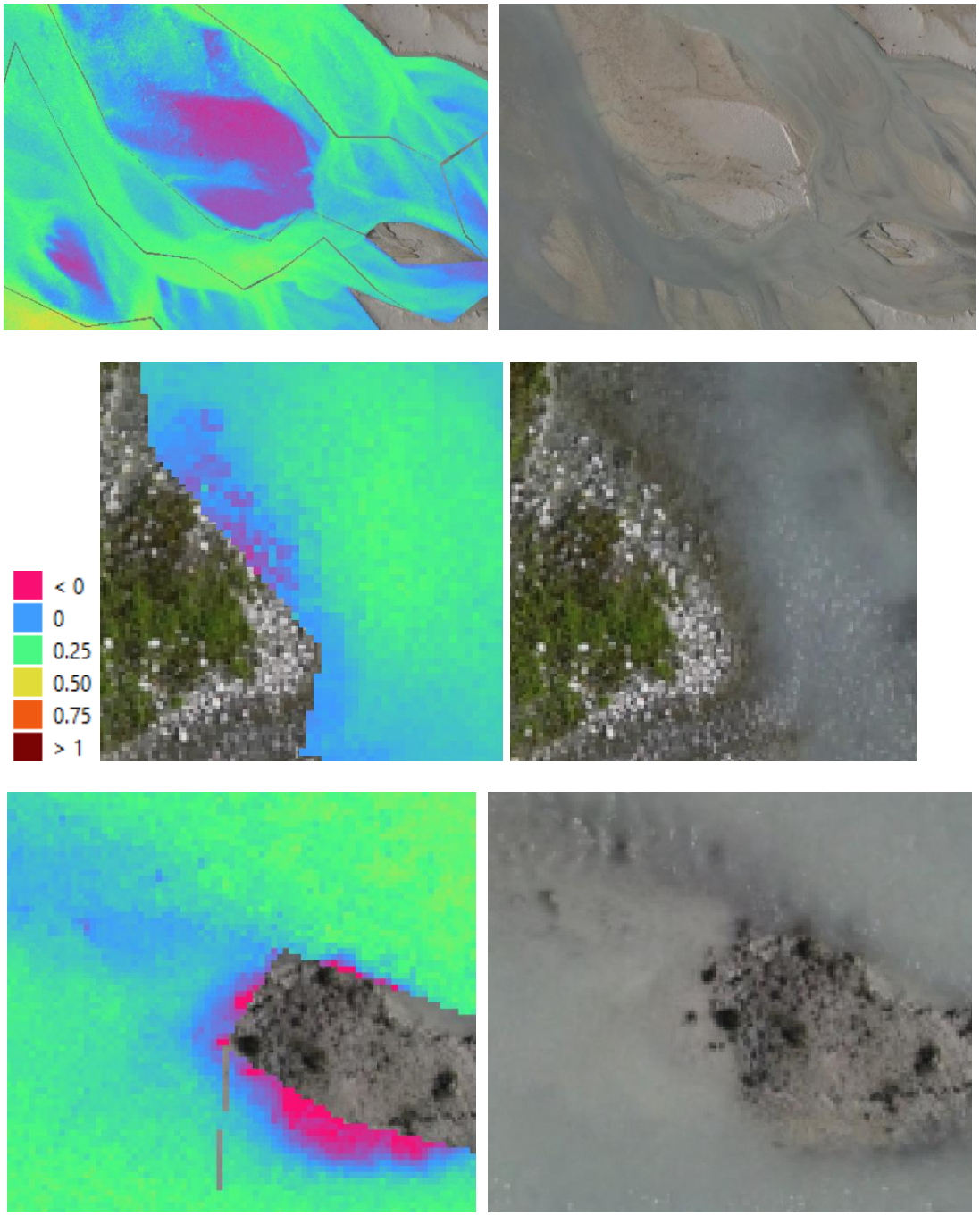

Figure 5.12 Detail of the model and the orthophoto for the highlighted areas 1 (top), 2 (centre), and 3 (bottom). Legenda: estimated depth (m). 2023 dataset.

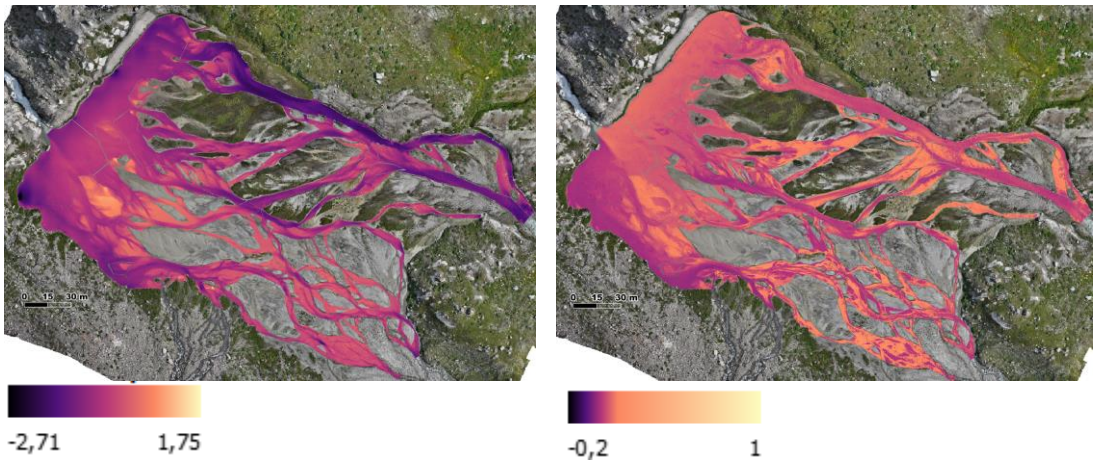

Figure 5.13 Spatial distribution of $\ln(DN_{NIR}/DN_G)$ (left) and $\ln(DN_G/DN_B)$ (right). 2023 dataset.

The undefined border between water and soil is also shown in Figure 5.13 (left) of the spatial distribution of $\ln(DN_{NIR}/DN_G)$, where these border regions are in orange. In fact, the soil absorbs more in blue and then gradually decreases for higher wavelengths. Water instead absorbs more in NIR than in visible bands. This opposite behaviour of soil and water in visible-NIR wavelength, can be also seen in Figure 5.14, looking at the trend of their spectral signatures. Therefore, in Figure 5.13, where there is soil, $\ln(DN_{NIR}/DN_G)$ is high (yellow) because it absorbs more in G than in NIR, while the water has lower values of $\ln(DN_{NIR}/DN_G)$ because it absorbs more in NIR (dark purple). Therefore, the presence of negative estimated depth values in those regions coupled with the spectral response in $\ln(DN_{NIR}/DN_G)$ values suggests the absence of any water depth.

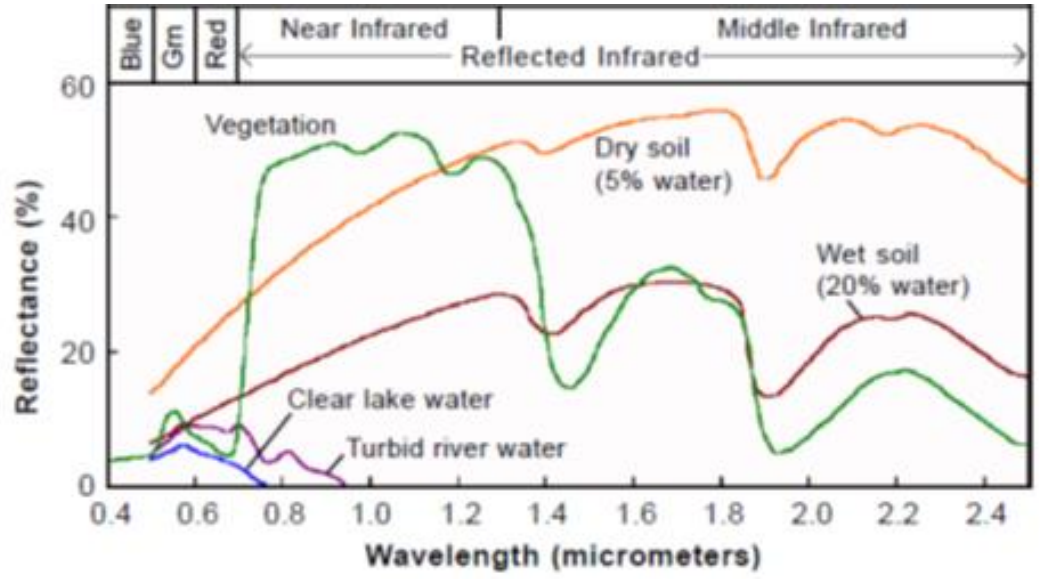

Figure 5.14 Spectral signatures of different materials, among them water and soil. Where the reflectance curve has a low peak, absorption is high. The blue band range is around 0.45 μm, Green 0.56 μm, Red 0.65 μm, Red Edge 0.73 μm, Near Infrared 0.86 μm. Online source.

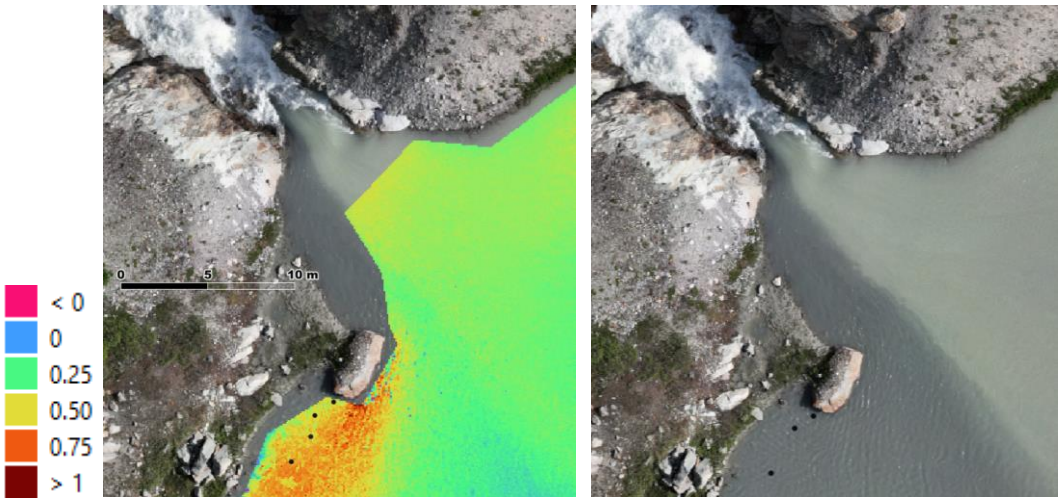

Figure 5.15 Detail of the model and orthophoto for the area of the outflowing cascade of the Lake. The lefthand picture shows the model results, and the black dots (in both pictures) indicate the points where measured depth values are available. Legenda: estimated depth (m). 2023 dataset.

Figure 5.15 shows another detail of the Lake, near the effluent cascade and the topographic barrier that causes water accumulation. In this area, the bathymetric model probably underestimates the water depth. In fact, the estimated depth in these areas ranges between 0.30 and 0.50 m, but according to the nearby measured points (black dots), this area probably is deeper. The measured points have a depth between 0.7 and 0.95 m, as well as the estimated depth in the vicinity of these points. The plausible cause of this potential underestimation can be attributed to water turbidity. Moreover, the demarcation line delineating two distinct sedimentary hues originating from separate tongues of the Rutor glacier is clearly evident.

Finally, Figure 5.16 shows the spatial distribution over the area of the regression coefficients α_j of the model.

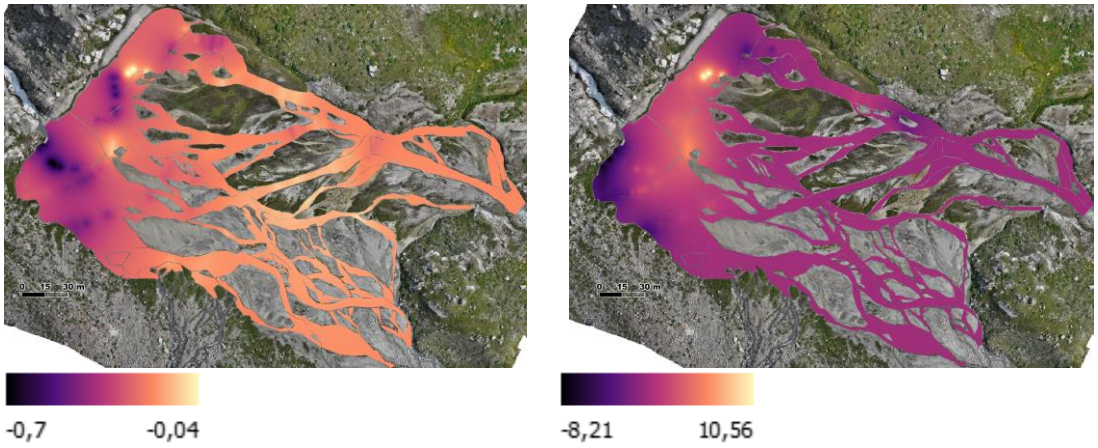

Figure 5.16 Spatial distribution of the regression coefficient $\alpha_j(1)$ (left) and $\alpha_j(2)$ (right) interpolated by IDW. 2023 dataset.

5.2.1 2023 Model Validation

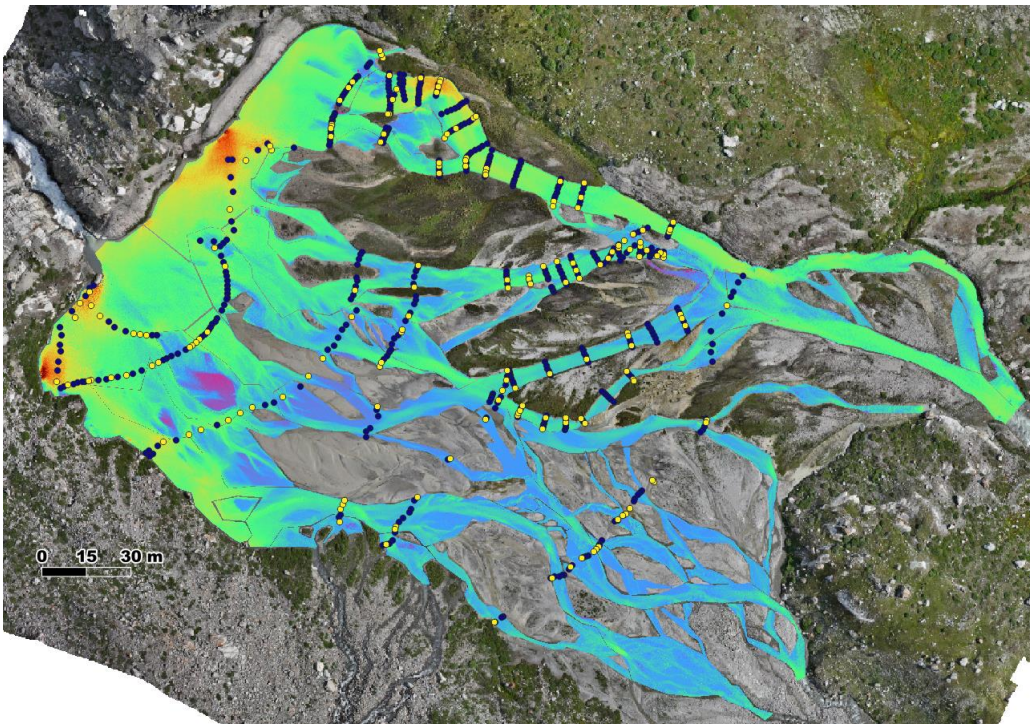

Figure 5.17 Blue dots are field-measurement points used for the calibration of the model, the yellow ones were used for the validation. 2023 dataset.

As previously mentioned, after the model calibration and prediction, the 2023 GWR2 was validated over the 30% of the total dataset (173 points). Figure 5.18 and Table 5.1 show the results of this validation, also recalling the calibration results, so to facilitate the comparison between the trained (calibrated) and the tested (validated) model. They show that even reducing the sample size, as the validation was performed only over 173 points, the model performances do not diminish significantly: R^2 decreases by about the 3% and RSR increased by the 15%, reaching the value of 0.472, still remaining in the range of very good performance, according to Moriasi et al. (2007) ranking classification.

Table 5.1 Accuracy of GWR2 models (calibrated and validated) in estimating water depth. 2023 dataset.

	Sample size	R^2	RSR	Negative values
calibration	422	0.937	0.410	22/422
validation	173	0.905	0.472	12/173

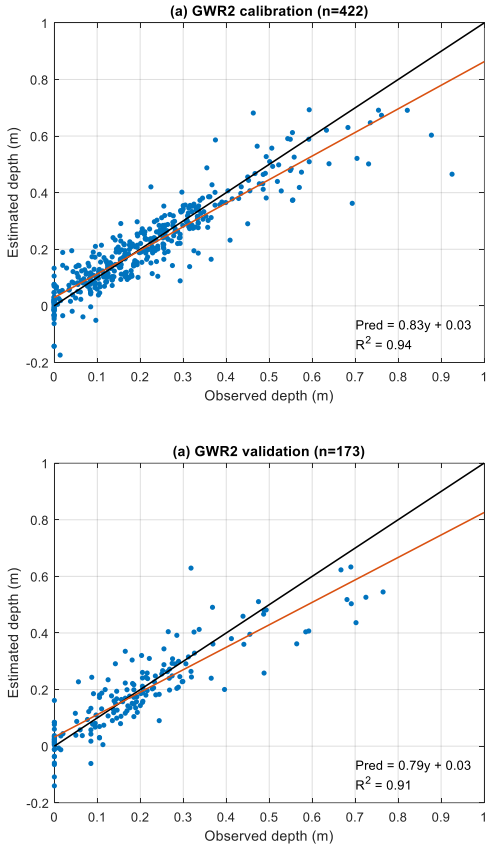

Figure 5.18 Comparison between observed water depth and estimated water depth using the calibrated GWR2 model (on the left) and the validated one (on the right). The black line indicates a linear line passing through the origin, while the orange line is a fitting line to estimations, represented by the formula in the graph. 2023 dataset (RGB and multispectral).

Figure 5.19 represents the frequency of the residuals $h_i - \hat{h}_i$ between observations and estimations of water depth, computed over the 173 measured points of the validation. Considering the total dataset (a), the model's estimation accuracy is good, as there is little deviation from the mean value, which is around 1 cm. In particular, for water depth shallower than 0.20 m and deeper than 0.40 m, little underestimation predominates, while for water depth ranging between 0.20 and 0.40 m there is mostly overestimation. However, the histogram is narrowly distributed around the mean, meaning little dispersion and standard deviation (s = 0.078 m for the total dataset). Residual values are significantly smaller for water depth shallower than 0.20 m, for which the average residual is less than 1 mm. On the other hand, the model results less precise when estimating water deeper than 0.40 m, being the mean residual for this range of depth about 9 cm. Good model performances are shown also for intermediate water depth, being the average residual for 0.20 m < h_i < 0.40 m only 8 mm.

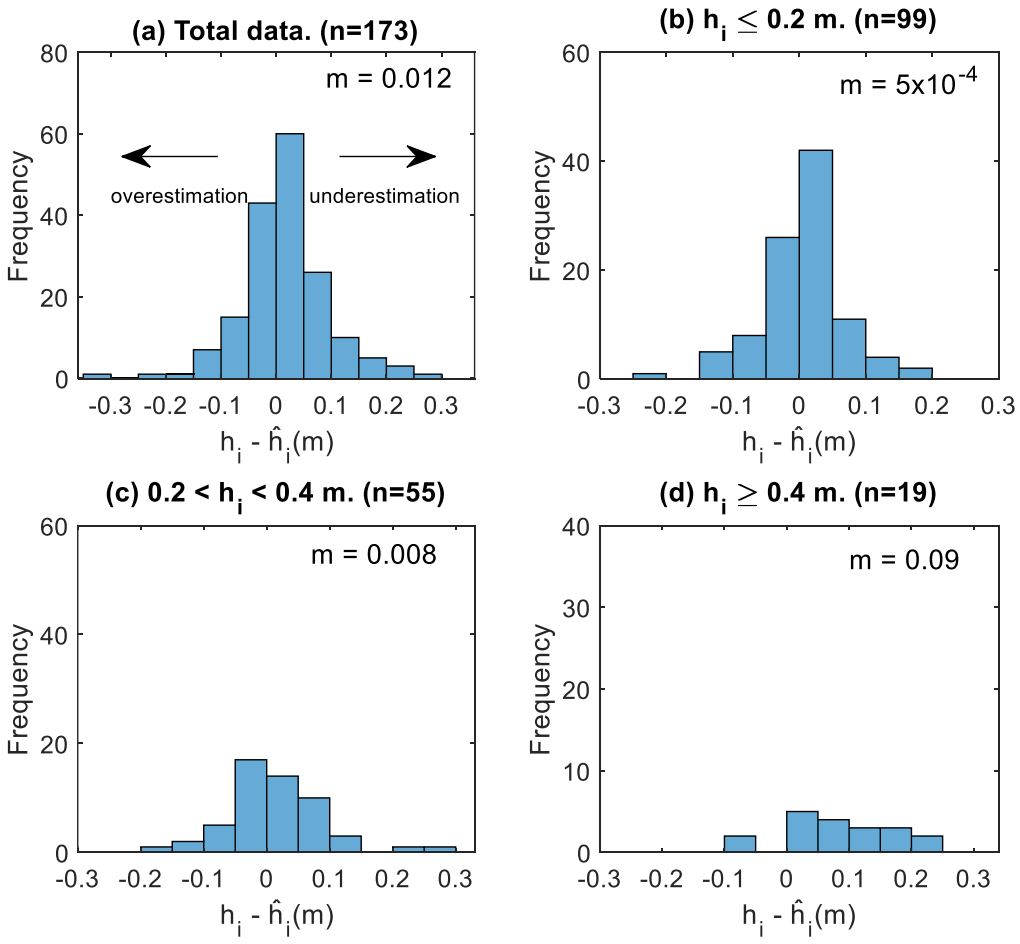

Figure 5.19 Frequency distribution of residuals $h_i - \hat{h}_i$ for different ranges of observed water depth: (a) whole data set, (b) depth shallower than 0.20 m, (c) between 0.20 and 0.40 m, (d) deeper than 0.40 m. The *m* in the graph indicates the mean value of the residuals in metres. Bar width=0.05m. 2023 dataset.

The under- and overestimation trends are visible also when examining Figure 5.20. It compares the simulated water depth to the measured one, along three randomly selected cross-sections among those of the 2023 field campaign. Both calibration and validation points falling in these sections are marked with different symbology (circles and diamonds, respectively).

Section 1 shows overestimation when its depth ranges between 0.20 and 0.40 m. Instead, underestimation can be observed in Section 1, where it goes deeper than 0.40 m, and in Sections 2 and 3 for water shallower than 0.20 m. However, biases generally remain contained to a few centimetres.

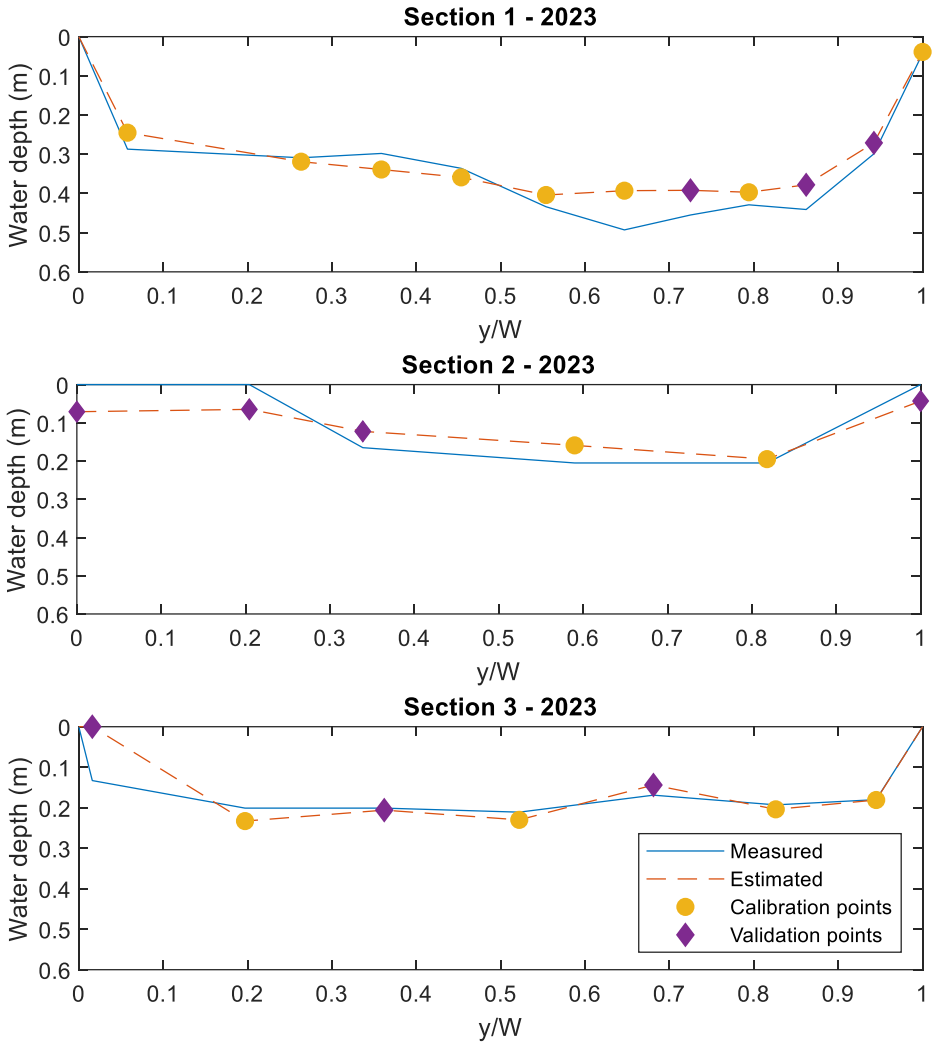

Figure 5.20 Comparison of simulated to measured water depth at three sections. y/W indicates the dimensionless distance from a bank of the section. Purple diamonds represent data points that belong to the 30% of the dataset, used for the validation, while the orange circles indicate calibration points. 2023 dataset.

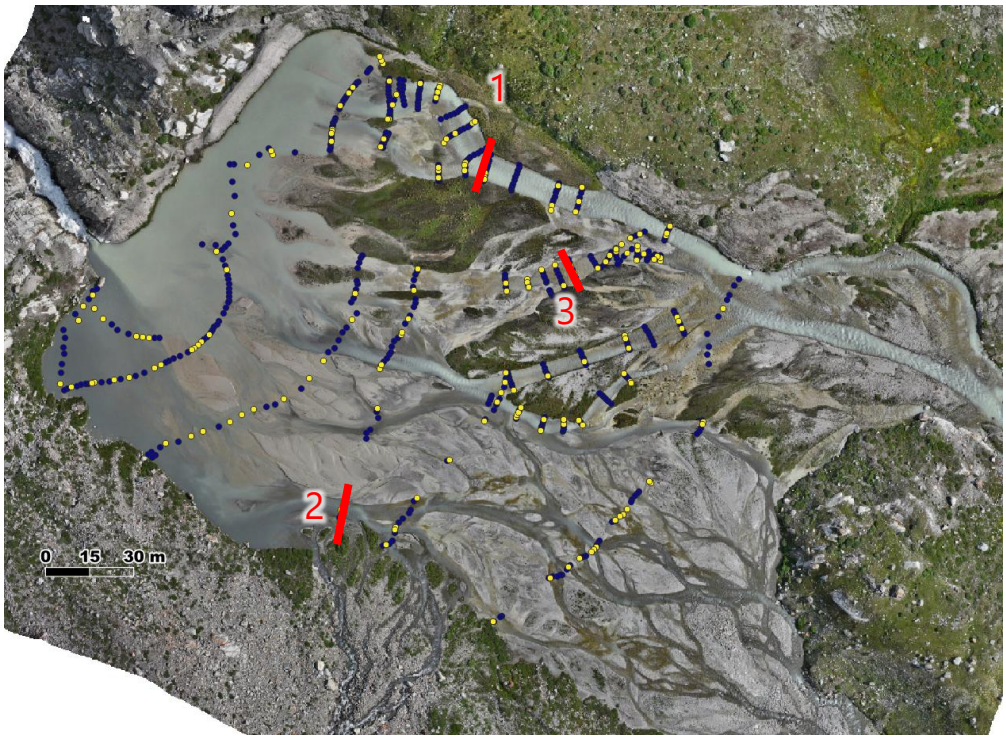

Figure 5.21 Overview of the position of Section 1, 2 and 3. 2023 dataset. Different colours in the label of points in the top pictures indicate the type of data: the blue label stands for calibration points, the yellow label for validation.

In conclusion, the GWR model gave a good representation of water depth with the average residual that was about 1 cm. Its best performance were related to the most frequent depth range of 0 - 0.40 m, where residuals were of the order of millimetres or even less.

5.3 Model Comparison

Comparing the results of the two datasets, the 2023 bathymetry reconstruction was more accurate than the 2021 reconstruction, likely due to the larger dataset of water depth observations and the use of multispectral UAV acquisition. This model performed better with low residuals average (0.01 m) and standard deviation (0.08 m).

Moreover, performance metrics were greatly enhanced. Specifically, R^2 were 0.77 for the 2021 dataset, improving to 0.94 for the 2023 dataset; and RSR decreased to 0.41 from 1.26.

A possible explanation is that multispectral data could more effectively model the effect of spatial heterogeneous bottom types, caused by submerged vegetation and sediment.

Ultimately, it can be asserted that the 2021 model primarily served as a procedural test, considering the limited dataset available. It resulted in a good preparatory analysis for the construction of the 2023 model, which constituted a significant application, given its substantial field-sourced data sample.

The multispectral data showed to be better than only RGB ones in bathymetry retrieval also if comparing the two models of 2023: the only RGB one and the multispectral one. The multispectral GWR2 significantly reduced the discrepancy between the model and the observations with respect to the RGB GWR2 model. In comparison to the results obtained from this latter model, the estimation accuracy improved. Particularly, the RSR value decreased from 0.583 to 0.410; and the R-squared value increased from 0.873 to 0.937.

5.4 Future Developments

Following the analysis of the existing literature and the research undertaken in this study, prospective ways for future developments include:

- improving the accuracy of the multispectral cartographic models, in particular of the DEM and orthomosaic. A possibility could be increasing the number of markers used both as GCPs and check points.
- gathering information on the spectral signatures of sediment types and vegetation by training the sensor in the laboratory, so as to know their radiometric response in the band ratios used as model inputs.
- combining photogrammetric data with those from other bathymetric mapping techniques, such as ERT or hydrographic LiDAR, to achieve a more accurate estimation of lake depth. ERT is Electrical Resistivity Tomography and due to the recent development, this method is comparatively easy to apply even in very heterogeneous mountain and arctic terrain.
- enlarging the sample size of the ground truth depth measurements to obtain better model calibration.
- exploiting a Kriging interpolation instead of an IDW for obtaining the model coefficients $\alpha_j(1)$ and $\alpha_j(2)$ during the prediction phase. Prediction accuracy results highlighted by Monteys et al., (2015) indicate that a Kriging model with an external drift, utilizing local Kriging neighbourhoods, emerges as the strongest predictor.
- considering the local bias b_i in the model equation (2), that here was disregarded, as a first approximation.

In order to characterize the ecosystem and its dynamics, vegetation and sediment transport would be interesting to study. In fact, while the glacier melts and retreats, the vegetation starts colonizing the terrain left uncovered by ice. This phenomenon is called the rising of the tree line.

Moreover, the catchment sediment supply has been deeply affected by the accelerated retreat and thinning of glaciers and ice sheets in recent decades. This, in turn, affects nutrient cycling, carbon flow, and the management of natural resources. Whilst significant attention has been focused on comprehending the spatio-temporal variations in meltwater production associated with deglaciation, sediment yields, which represent a comprehensive indicator of geomorphological activity and

consequently the stability of a landscape within a watershed, have received comparatively less research (Carrivick and Tweed, 2021).

5.4.1 Thermal Data

After the last expedition to Rutor in September 2023, where a new UAV thermal sensor was tested, the idea to integrate this new dataset with the presented GWR model, was developed. The new bathymetric model should select its input variables not only from the bands here studied, but it could rely on a new wavelength range which is the thermal one. The UAV used was a DJI Mavic 3T which can acquire photos in the spectral range 8-14 μm of thermal infrared, and measure temperatures between -20° to 150° C. This idea is based on the fact that temperature is a good proxy for water depth, due to the temperature gradient that a water column typically exhibits.

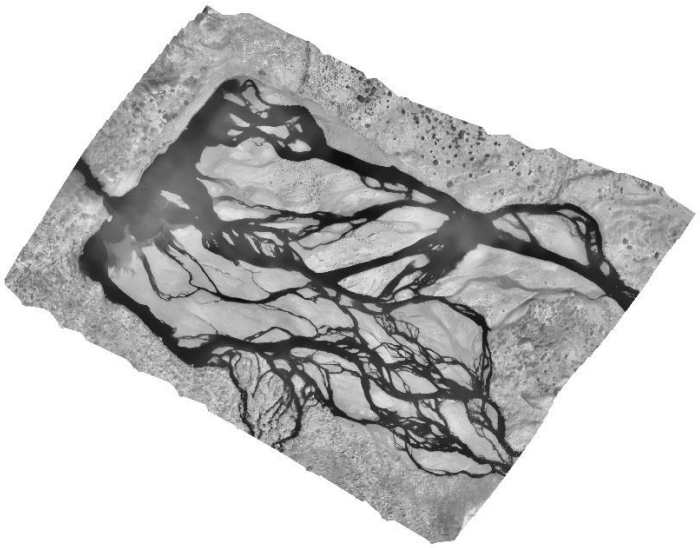

Figure 5.22 Orthophoto produced from a UAV flight of September 2023, using a thermal sensor.

Figure 5.22 shows the first results from the processing of thermal sensor imagery, provided by the Glacier-Lab researchers. The DN (Digital Number) values of the orthophoto have not been calibrated yet. However, based on a qualitative estimate, it can be stated that the temperatures in the study area are as follows: around 15-20 °C on the bars, approximately zero °C near the cascade, and 5-6 °C in the shallower areas.

6. Conclusions

The objective of this thesis was a comprehensive exploration of bathymetry estimation in a dynamic proglacial environment, specifically focusing on Marginale Lake in the Italian Alps. Through geomatic data collected in 2021 and 2023, valuable insights were provided regarding the effectiveness of Geographically Weighted Regression (GWR) models in the retrieval of bathymetric information from remote sensing data.

The bathymetric inversion models were constructed by utilizing the ratio of two spectral bands, derived through principal component analysis (PCA). The chosen input band ratios exhibited a significant correlation with the observed water depth, measured on the field.

6.1 Key Findings

6.1.1 2021 Results

In 2021, the GWR model, employing PCA-selected band ratios $\ln(DN_B/DN_R)$ and $\ln(DN_G/DN_B)$, revealed interesting insights into Marginale Lake's bathymetry. While the model showed promise, it tended to underestimate water depth, particularly for depths greater than 20 cm. This underestimation appeared to be related to localized changes in the bed type, high turbidity of the water and, mostly, the small size of the dataset over which the model was trained. Nevertheless, this preliminary analysis laid the foundation for subsequent investigations.

6.1.2 2023 Results

The 2023 dataset, characterized by a more extensive collection of water depth observations and the inclusion of multispectral data, marked a significant advancement. The spectral inputs selected for this GWR model were the band ratios $\ln(DN_{NIR}/DN_G)$ and $\ln(DN_G/DN_B)$. The GWR model calibrated for 2023 demonstrated improved accuracy, with average residuals of about 1 cm. It successfully reproduced the most common depth range of 0 - 0.40 m, where the average residual was measured in the order of millimetres. However, underestimation occurred for depths exceeding 0.40 m. Notably, the larger dataset and multispectral data contributed to this enhanced performance.

6.1.3 Model Comparison

The findings indicated that for both the 2021 and 2023 datasets, the GWR models relying on a single band ratio input exhibited discrepancies between estimates and observations, especially in the 2021 dataset. Conversely, when both PCA-selected band ratios were considered, the GWR models demonstrated enhanced performance.

Comparing the two datasets, the 2023 bathymetry reconstruction stood out as more accurate than the 2021 reconstruction. This improvement was attributed to the greater number of ground truth depth measurements over which the model was calibrated and the use of multispectral imagery. The multispectral GWR model significantly reduced deviations between the model and observations, exemplified by lower values of the Root Mean Standard Deviation Ratio (RSR) and higher R^2 values, which were 0.41 and 0.94, respectively. Multispectral imagery was more advantageous to resolve the effects of inhomogeneous streambeds.

Ultimately, the 2021 model was mainly used as a procedural test due to the limited dataset. However, it proved to be a useful preparatory analysis for the development of the 2023 model, which had a significant amount of field-sourced data and was the main focus of the application.

6.2 Final Remarks

In summary, this thesis has made significant strides in advancing our understanding of proglacial environments and the application of GWR models and UAV imagery for bathymetric mapping. While challenges and limitations persist, the findings underscore the potential of multispectral data and expanded datasets in improving the accuracy of bathymetry estimations in dynamic mountainous regions. As global warming continues to impact these critical ecosystems, the research serves as a valuable foundation for further investigations, ultimately contributing to the comprehensive monitoring and management of proglacial areas in the face of ongoing environmental changes.

References

Agisoft Metashape User Manual - Professional Edition, Version 1.8

Aguilera, A.M., Escabias, M., Valderrama, M.J., 2006. Using principal components for estimating logistic regression with high-dimensional multicollinear data. Computational Statistics & Data Analysis 50 (8), 1905–1924.

ARPA VDA. Rilievi Glaciologici in Valle D'Aosta – anno 2022. Tech. rep. Loc. Grande Charrière 44 - 11020 Saint-Christophe (AO), Valle d'Aosta, Italy: Agenzia Regionale per la Protezione dell'Ambiente (ARPA VDA), 2022 (cit. on p. 12).

Barandun M, Huss M, Sold L, Farinotti D, Asisov E, Salzmann N, Usubaliev R, Merkushkin A, Hoelzle M (2015) Re-analysis of seasonal mass balance at Abramov glacier 1968–2014. J Glaciol 61 (230):1103–1117

Barry P., Coakley R.; Accuracy of UAV photogrammetry compared with network RTK GPS. Int. Arch. Photogrammetric Remote Sens. XL-1/W2, 27–31, 2013.

Beisel, J.N., Usseglio-Polatera, P., Moreteau, J.C., 2000. The spatial heterogeneity of a river bottom: a key factor determining macroinvertebrate communities. Assessing the Ecological Integrity of Running Waters. Springer, Dordrecht, pp. 163–171

Bolch T, Kamp U (2006) Glacier mapping in high mountains using DEMs, Landsat and ASTER data. Grazer Schriften der Geographie und Raumforschung 41. In: Proceedings of the 8th Int. Symp. on High Mountain Remote Sensing Cartography, 20–27 March 2005, La Paz, Bolivia, pp. 13–24

Brando, V.E., Anstee, J.M.,Wettle,M., Dekker, A.G., Phinn, S.R., Roelfsema, C., 2009. A physics based retrieval and quality assessment of bathymetry from suboptimal hyperspectral data. Remote Sens. Environ. 113 (4), 755–770.

Carrivick, J.L., Tweed, F.S., 2021. Deglaciation controls on sediment yield: Towards capturing spatio-temporal variability. Earth-Science Reviews 221, 103809. https://doi.org/10.1016/j.earscirev.2021.103809

ConveRgo, www.cisis.it

Corte, E., Ajmar, A., Camporeale, C., Cina, A., Coviello, V., Giulio Tonolo, F., Godio, A., Macelloni, M. M., Tamea, S., and Vergnano, A.: Multitemporal characterisation of a proglacial system: a multidisciplinary approach, Earth Syst. Sci. Data Discuss. [preprint], https://doi.org/10.5194/essd-2023-94, in review, 2023.

Cotton, J.A., Wharton, G., Bass, J.A.B., Heppell, C.M., Wotton, R.S., 2006. The effects of seasonal changes to in-streamvegetation cover on patterns of flow and accumulation of sediment. Geomorphology 77 (3–4), 320–334.

Crowder, D.W., Diplas, P., 2000. Using two-dimensional hydrodynamicmodels at scales of ecological importance. J. Hydrol. 230 (3–4), 172–191.

Ding, K., Li, Q., Zhu, J., Wang, C., Guan, M., Chen, Z., Yang, C., Cui, Y., Liao, J., 2018. An improved quadrilateral fitting algorithm for the water column contribution in airborne bathymetric Lidar waveforms. Sensors 18 (2), 552.

Dixon John C., 2016, Glacial and Periglacial Geomorphology

Ferguson, R.I., Parsons, D.R., Lane, S.N., Hardy, R.J., 2003. Flow in meander bends with recirculation at the inner bank. Water Resour. Res. 39 (11).

Fonstad, M.A., Marcus, W.A., 2005. Remote sensing of stream depths with hydraulically assisted bathymetry (HAB) models. Geomorphology 72 (1–4), 320–339.

Fotheringham, A.S., Charlton, M.E., Brunsdon, C., 1998. Geographically weighted regression: a natural evolution of the expansion method for spatial data analysis. Environ Plan A 30 (11), 1905–1927.

Gomarasca M.A.; Basics of geomatics. Apply Geomatics 2, 137–146, 2010. https://doi.org/10.1007/s12518-010-0029-6

Gonçalves J.A., Bastos L., Perez B., Magalhães A.; Monitoring of beaches and sand dunes using digital aerial photography with direct georeferencing. Int. Arch. Photogramm. Remote Sens. XXXVIII-7/B, 228–232, 2010.

Gonçalves J.A., Bastos L., Pinho J., Granja H.; Digital aerial photography to monitor changes in coastal areas based on direct georeferencing; Proceedings of the 5th EARSeL Workshop on Remote Sensing of the Coastal Zone, Prague, 2011.

Grenfell Thomas C.(2011). Albedo. In V. P. Singh, P. Singh, & U. K. Haritashya (A c. Di), Encyclopedia of Snow, Ice and Glaciers (pp. 23-24). Springer Netherlands. https://doi.org/10.1007/978-90-481-2642-2

Guenther, G.C., Cunningham, A.G., LaRocque, P.E., Reid, D.J., 2000. Meeting the Accuracy Challenge in Airborne Bathymetry (National Oceanic Atmospheric Administration/Nesdis Silver Spring MD).

Gülch E.; Photogrammetric evaluation of multi-temporal fixed wing UAV imagery. Int. Arch. Photogrammetry Remote Sensing XXXVIII-1/C22, 265–270, 2011.

Haala N., Cramer M., Rothermel M.; Quality of 3D point clouds from highly overlapping UAV Imagery; Int. Arch. Photogramm. Remote Sens. XL-1/W2, 183– 188, 2013.

Haala N., Cramer M., Weimer F., Trittler M.; Performance test on UAV-based data collection; Int. Arch. Photogramm. Remote Sens. XXXVIII-1/C22, 7–12, 2011.

Haala N., Rothermel M.; Dense Multi-Stereo Matching for High Quality Digital Elevation Models. PFG Photogrammetrie, Fernerkundung, Geoinformation. 2012 (4), 331–343, 2012.

Haala N.; Comeback of digital image matching; Photogrammetric Week. Wichmann Verlag, Heidelberg, pp. 289–301, 2009.

Heckmann, T., Morche, D., Becht, M. (2019). Introduction. In: Heckmann, T., Morche, D. (eds) Geomorphology of Proglacial Systems. Geography of the Physical Environment. Springer, Cham. https://doi-org.ezproxy.biblio.polito.it/10.1007/978-3-319-94184-4_1

Hilldale, R.C., Raff, D., 2008. Assessing the ability of airborne LiDAR to map river bathymetry. Earth Surf. Process. Landf. 33 (5), 773–783.

Hock, R., G. Rasul, C. Adler, B. Cáceres, S. Gruber, Y. Hirabayashi, M. Jackson, A. Kääb, S. Kang, S. Kutuzov, Al. Milner, U. Molau, S. Morin, B. Orlove, and H. Steltzer, 2019: High Mountain Areas. In: IPCC Special Report on the Ocean and Cryosphere in a Changing Climate [H.-O. Pörtner, D.C. Roberts, V. Masson-Delmotte, P. Zhai, M. Tignor, E. Poloczanska, K. Mintenbeck, A. Alegría, M. Nicolai, A. Okem, J. Petzold, B. Rama, N.M. Weyer (eds.)]. Cambridge University Press, Cambridge, UK and New York, NY, USA, pp. 131–202. https://doi.org/10.1017/9781009157964.004. In: Special Report on the Ocean and Cryosphere in a Changing Climate. Special Report of the Intergovernmental Panel on Climate Change. 2022.

Hondzo, M., Voller, V.R., Morris, M., Foufoula-Georgiou, E., Finlay, J., Ganti, V., Power, M.E., 2013. Estimating and scaling stream ecosystemmetabolismalong channels with heterogeneous substrate. Ecohydrology 6 (4), 679–688

IPCC Reports from 2013, 2017, 2018, 2021

IPCC, 2014: Climate Change 2014: Synthesis Report. Contribution of Working Groups I, II and III to the Fifth Assessment Report of the Intergovernmental Panel on Climate Change [Core Writing Team, R.K. Pachauri and L.A. Meyer (eds.)]. IPCC, Geneva, Switzerland, 151 pp.

IPCC, 2019. Summary for policymakers. In: P¨ortner, H.-O., Roberts, D.C., Masson-Delmotte, V., Zhai, P., Tignor, M., Poloczanska, E., Mintenbeck, K., Nicolai, M., Okem, A., Petzold, J., Rama, B., Weyer, N. (Eds.), IPCC Special Report on the Ocean and Cryosphere in a Changing Climate.

Jia, Y., Wang, S.S., 1999. Numerical model for channel flow and morphological change studies. J. Hydraul. Eng. 125 (9), 924–933.

John Menzies, Glacial Geomorphology, Reference Module in Earth Systems and Environmental Sciences, Elsevier, 2018

Johnson PG (2002) Proglacial and paraglacial fluvial and lacustrine environments in transition. In: Hewitt K,Byrne M-L, English M, Young G (eds) Landscapes oftransition. Springer, Netherlands, Dordrecht, pp 43–62

Jonathan L. Carrivick, Fiona S. Tweed, Deglaciation controls on sediment yield: Towards capturing spatio-temporal variability, Earth-Science Reviews, Volume 221, 2021, 103809,ISSN 0012-8252,https://doi.org/10.1016/j.earscirev.2021.103809.

Julien, P.Y., Klaassen, G.J., Ten Brinke,W.B.M.,Wilbers, A.W.E., 2002. Case study: bed resistance of Rhine River during 1998 flood. J. Hydraul. Eng. 128 (12), 1042–1050.

Kalkwijk, J.T., De Vriend, H.J., 1980. Computation of the flow in shallow river bends. J. Hydraul. Res. 18 (4), 327–342.

Kanno, A., Tanaka, Y., 2012. Modified Lyzenga's method for estimating generalized coefficients of satellite-based predictor of shallow water depth. IEEE Geosci. Remote Sens. Lett. 9 (4), 715–719.

Kappas Martin (2011). Aerial photogrammetry for glacial monitoring. In V. P. Singh, P. Singh, & U. K. Haritashya (A c. Di), Encyclopedia of Snow, Ice and Glaciers (pp. 4-15). Springer Netherlands. https://doi.org/10.1007/978-90-481-2642-2

Kim, J. S., Baek, D., Seo, I. W., & Shin, J. (2019). Retrieving shallow stream bathymetry from UAV-assisted RGB imagery using a geospatial regression method. Geomorphology, 341, 102–114. https://doi.org/10.1016/j.geomorph.2019.05.016

Kim, J., Kim, D., Son, G., Kim, S., 2015. Accuracy analysis of velocity and water depth measurement in the straight channel using ADCP. Journal of KoreaWater Resources Association 48 (5), 367–377.

Kim, J.S., Seo, I.W., Baek, D., 2018. Modeling spatial variability of harmful algal bloom in regulated rivers using a depth-averaged 2D numerical model. J. Hydro Environ. Res. 20, 63–76.

Kinzel, P.J., Wright, C.W., Nelson, J.M., Burman, A.R., 2007. Evaluation of an experimental LiDAR for surveying a shallow, braided, sand-bedded river. J. Hydraul. Eng. 133 (7), 838–842.

Kundzewicz Z.W., in Encyclopedia of Ecology, 2008

Küng O., Strecha C., Beyeler A., Zufferey J.C., Floreano D., Fua P., Gervaix F.; The accuracy of automatic photogrammetric techniques on ultra-light UAV imagery; Int. Arch. Photogramm. Remote Sens. XXXVIII-1/C22, 125–130, 2011.

Lamarre, H., Roy, A.G., 2008. The role of morphology on the displacement of particles in a step–pool river system. Geomorphology 99 (1–4), 270–279

Lee, Z., Carder, K.L., Mobley, C.D., Steward, R.G., Patch, J.S., 1999. Hyperspectral remote sensing for shallow waters: 2. Deriving bottom depths and water properties by optimization. Appl. Opt. 38 (18), 3831–3843.

Legleiter, C.J., 2013. Mapping river depth from publicly available aerial images. River Res. Appl. 29 (6), 760–780.

Legleiter, C.J., Overstreet, B.T., Glennie, C.L., Pan, Z., Fernandez-Diaz, J.C., Singhania, A., 2016. Evaluating the capabilities of the CASI hyperspectral imaging system and Aquarius bathymetric LiDAR for measuring channel morphology in two distinct river environments. Earth Surf. Process. Landf. 41 (3), 344–363.

Legleiter, C.J., Roberts, D.A., Lawrence, R.L., 2009. Spectrally based remote sensing of river bathymetry. Earth Surf. Process. Landf. 34 (8), 1039–1059.

Lingua, A. M., Maschio, P., Spadaro, A., Vezza, P., & Negro, G. (2023). ITERATIVE REFRACTION-CORRECTION METHOD ON MVS-SFM FOR SHALLOW STREAM BATHYMETRY. The International Archives of the Photogrammetry, Remote Sensing and Spatial Information Sciences, XLVIII-1/W1-2023, 249–255. https://doi.org/10.5194/isprs-archives-XLVIII-1-W1-2023-249-2023

Lyzenga, D.R., Malinas, N.P., Tanis, F.J., 2006. Multispectral bathymetry using a simple physically based algorithm. IEEE Trans. Geosci. Remote Sens. 44 (8), 2251–2259.

M. Tranter, J.L Wadham, 7.5 - Geochemical Weathering in Glacial and Proglacial Environments, Editor(s): Heinrich D. Holland, Karl K. Turekian, Treatise on Geochemistry (Second Edition), Elsevier, 2014, Pages 157-173, ISBN 9780080983004

Ma, S., Tao, Z., Yang, X., Yu, Y., Zhou, X., Li, Z., 2. Bathymetry retrieval from hyperspectral remote sensing data in optical-shallow water. IEEE Trans. Geosci. Remote Sens. 52 (2), 1205–1212.

Macelloni, 2022, Drone, aerial and satellite photogrammetry for 4D glacier survey and monitoring

Matthews, J. A. (2019). Geomorphology of Proglacial Systems: Landform and Sediment Dynamics in Recently Deglaciated Alpine Landscapes. The Holocene, 29(7), 1249–1250. https://doi.org/10.1177/0959683619840576

Merwade, V., 2009. Effect of spatial trends on interpolation of river bathymetry. J. Hydrol. 371 (1–4), 169–181.

Monteys, X., Harris, P., Caloca, S., Cahalane, C., 2015. Spatial prediction of coastal bathymetry based on multispectral satellite imagery and multibeam data. Remote Sens. 7 (10)

Moriasi et al. (2007). Model Evaluation Guidelines for Systematic Quantification of Accuracy in Watershed Simulations. Trans. ASABE 50, 885–900. \Sexpr[results=rd]{tools:::Rd_expr_doi("10.13031/2013.23153")}

Ning Liu (2023). Geographically weighted regression (https://www.mathworks.com/matlabcentral/fileexchange/81011-geographically-weighted-regression), MATLAB Central File Exchange. Retrieved September 14, 2023.

NSIDC, 2015. http://nsidc.org/arcticseaicenews/2015/12/a-variable-rate-of-ice-growth/

of the Intergovernmental Panel on Climate Change Coordinating Lead Authors: Lead Authors, s.l.: s.n.

Orombelli Giuseppe. «Il Ghiacciaio del Rutor (Valle d'Aosta) nella Piccola Età Glaciale». In: Geografia Fisica e Dinamica Quaternaria Suppl. VII (2005), pp. 239–257 (cit. on p. 10).

Otto, JC. (2019). Proglacial Lakes in High Mountain Environments. In: Heckmann, T., Morche, D. (eds) Geomorphology of Proglacial Systems. Geography of the Physical Environment. Springer, Cham. https://doi-org.ezproxy.biblio.polito.it/10.1007/978-3-319-94184-4_14)

Painter, T. H., Seidel, F. C., Bryant, A. C., McKenzie Skiles, S., and Rittger, K. (2013), Imaging spectroscopy of albedo and radiative forcing by light-absorbing impurities in mountain snow, J. Geophys. Res. Atmos., 118, 9511–9523, doi:10.1002/jgrd.50520.

Paul F (2002) Changes in glacier area in Tyrol, Austria, between 1969 and 1992 derived from Landsat 5 TM and Austrian Glacier Inventory data. Int J Remote Sens 23(4):787–799

Paul F (2015) Kartierung von Gletschern mit Satellitendaten und das globale Gletscherinventar. In: Lozán JL, Grassl H, Kasang D, Notz D Escher-Vetter H (Hrsg.): Warnsignal Klima: Das Eis der Erde (Kap. 4.1):103– 110

Paul F. and Bolch T., 2019, Glacier Changes Since the Little Ice Age. In: Heckmann and D. Morche (eds.), Geomorphology of Proglacial Systems, Geography of the Physical Environment, https://doi.org/10.1007/978-3-319-94184-4_2

Paulo Ceppi, Simon C. Scherrer, Andreas M. Fischer, Christof Appenzeller, 2010, Revisiting Swiss temperature trends 1959–2008. International Journal of Climatology, RMetS

Philpot, W.D., 1989. Bathymetric mapping with passive multispectral imagery. Appl. Opt. 28 (8), 1569–1578.

Pontoglio Emanuele, Grasso Nives, Cagninei Andrea, Camporeale Carlo, Dabove Paolo, & Lingua Andrea Maria. (2020). Bathymetric Detection of Fluvial Environments through UASs and Machine Learning Systems. Remote Sensing, 12(24), 4148. https://doi.org/10.3390/rs12244148

Principal Component Analysis (PCA) Explained | Built In. (https://builtin.com/data-science/step-step-explanation-principal-component-analysis)

Rasul, G., Pasakhala, B., Mishra, A. & Pant, S., 2020. Adaptation to mountain cryosphere change: issues and challenges. In: s.l.:Taylor and Francis Ltd., pp. 297-309.

Rosnell T., Honkavaara E.; Point cloud generation from aerial image data acquired by a quadrocopter type micro unmanned aerial vehicle and a digital still camera. Sensors 12 (1), 453–480, 2012.

Shannon, S., Smith, R., Wiltshire, A., Payne, T., Huss, M., Betts, R., Caesar, J., Koutroulis, A., Jones, D., Harrison, S., 2019. Global glacier volume projections under high-end climate change scenarios. Cryosphere 13, 325–350.

Slaymaker O (2009) Proglacial, periglacial or paraglacial? In: Knight J, Harrison S (eds) Periglacial and Paraglacial Processes and Environments. The Geological Society Publishing House, London, pp 71–84

Slaymaker O (2011) Criteria to distinguish between periglacial, proglacial and paraglacial environments. Quaest Geogr 30:85–94

Stumpf, R.P., Holderied, K., Sinclair, M., 2003. Determination of water depth with highresolution satellite imagery over variable bottom types. Limnol. Oceanogr. 48 (1part2), 547–556.

Su, H., Liu, H., Heyman, W.D., 2008. Automated derivation of bathymetric information from multi-spectral satellite imagery using a non-linear inversion model. Mar. Geod. 31 (4), 281–298.

Su, H., Liu, H.,Wang, L., Filippi, A.M., Heyman,W.D., Beck, R.A., 2014. Geographically adaptiveinversion model for improving bathymetric retrieval from satellite multispectral imagery. IEEE Trans. Geosci. Remote Sens. 52 (1), 465–476.

Szymon Śledź, Marek W. Ewertowski, Jan Piekarczyk, 2021, Applications of unmanned aerial vehicle (UAV) surveys and Structure from Motion photogrammetry in glacial and periglacial geomorphology

Vallet J., Panissod F., Strecha C., Tracol M.; Photogrammetric performance of an ultra-light weight Swinglet ''UAV''. Int. Arch. Photogrammetric Remote Sensing 63, 253–258, 2011.

Vaughan, D. G. et al., 2013. Observations: Cryosphere. In: Climate Change 2013: The Physical Sci-ence Basis. Contribution of Working Group I to the Fifth Assessment Report

Vergnano A., C. Oggeri, and A. Godio. «Geophysical–geotechnical methodology for assessing the spatial distribution of glacio-lacustrine sediments: The case history of Lake Seracchi». In: Earth Surface Processes and Landforms (2023).

Viani Cristina and other. «Potential future lakes from continued glacier shrinkage in the Aosta Valley Region (Western Alps, Italy)». In: Geomorphology 69 (2020), pp. 1–15 (cit. on pp. 8–10).

Villa Fabio, Valter Maggi, and Mattia De Amicis. «GIS analysis of Rutor Glacier (Aosta Valley, Italy) volume and terminus variations». In: Supplementi di Geografia Fisica e Dinamica Quaternaria 30 (Jan. 2007), pp. 87–95 (cit. on pp. 10, 13, 14).

Vinayaraj, P., Raghavan, V., Masumoto, S., 2016. Satellite-derived bathymetry using adaptive geographically weighted regression model. Mar. Geod. 39 (6), 458–478.

Wang Qixiang, Mengben Wang, Xiaohui Fan, 2018, Seasonal patterns of warming amplification of high-elevation stations across the globe. International Journal of Climatology, RMetS

Wang, H.-J. and Chen, H.-P.: Understanding the recent trend of haze pollution in eastern China: roles of climate change, Atmos. Chem. Phys., 16, 4205–4211, https://doi.org/10.5194/acp-16-4205-2016, 2016.

WGMS (2008) Global glacier changes: facts and figures. UNEP, World Glacier Monitoring Service, Zurich, Switzerland WGMS (2015) Global Glacier Change Bulletin No. 1 (2012–2013). World Glacier Monitoring Service, Zurich, Switzerland

Zemp M, Frey H, Gärtner-Roer I, Nussbaumer SU, Hoelzle M, Paul F, Haeberli W, Denzinger F, Ahlstrøm AP, Anderson B, Bajracharya S, Baroni C, Braun LN, Cáceres BE, Casassa G, Cobos G, Dávila LR, Delgado Granados H, Demuth MN, Espizua L, Fischer A, Fujita K, Gadek B, Ghazanfar A, Hagen JO, Holmlund P, Karimi N, Li Z, Pelto M, Pitte P, Popovnin VV, Portocarrero CA, Prinz R, Sangewar CV, Severskiy I, Sigurðsson O, Soruco A, Usubaliev R, Vincent C 2015) Historically unprecedented global glacier decline in the early 21st century. J Glaciol 61(228):745–762

Zumbühl HJ, Holzhauser H (1988) Alpengletscher in der kleinen Eiszeit: Sonderheft zum 125jährigen Jubiläum des SAC. Die Alpen 64(3):129–322

List of Figures

List of Tables

Annex 1

Volo_DJI_9_luglio_2021

Volo_DJI_9_luglio_2021
13 December 2021

Survey Data

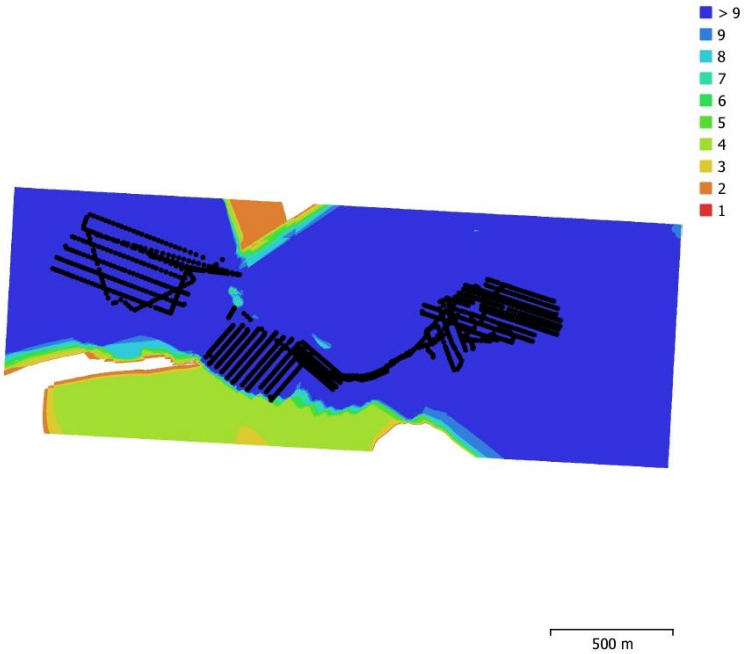

Fig. 1. Camera locations and image overlap.

Number of images:	1,480	Camera stations:	1,466
Flying altitude:	126 m	Tie points:	13,542,470
Ground resolution:	2.8 cm/pix	Projections:	51,769,409
Coverage area:	2.6 km²	Reprojection error:	0.627 pix

Camera Model	Resolution	Focal Length	Pixel Size	Precalibrated
FC6310R (8.8mm)	5472 x 3648	8.8 mm	2.41 x 2.41 µm	No

Table 1. Cameras.

Camera Calibration

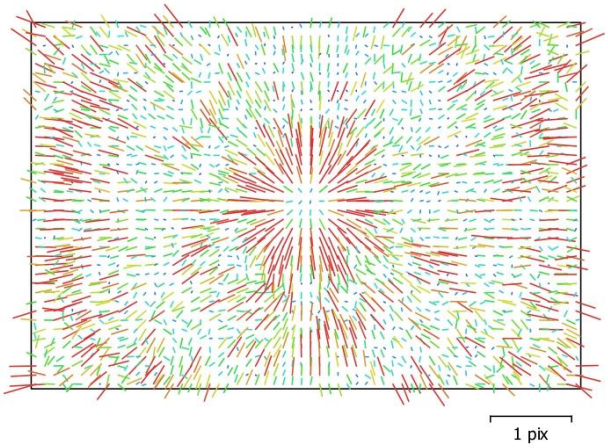

Fig. 2. Image residuals for FC6310R (8.8mm).

FC6310R (8.8mm)
1480 images

Type	Resolution	Focal Length	Pixel Size
Frame	**5472 x 3648**	**8.8 mm**	**2.41 x 2.41 µm**

	Value	Error	F	Cx	Cy	K1	K2	K3	P1	P2
F	**3629.12**	0.0056	1.00	-0.03	-0.19	-0.14	0.17	-0.15	-0.03	0.01
Cx	**-1.81417**	0.0043		1.00	0.01	-0.00	0.00	-0.00	0.72	-0.02
Cy	**5.31658**	0.0046			1.00	0.00	-0.00	0.00	-0.02	0.55
K1	**-0.00364791**	2.8e-06				1.00	-0.96	0.90	-0.01	-0.01
K2	**-0.0096122**	7.4e-06					1.00	-0.98	0.00	0.00
K3	**0.00808623**	6.1e-06						1.00	-0.00	-0.00
P1	**-0.00105358**	3.1e-07							1.00	-0.04
P2	**-0.000664527**	2.7e-07								1.00

Table 2. Calibration coefficients and correlation matrix.

Camera Locations

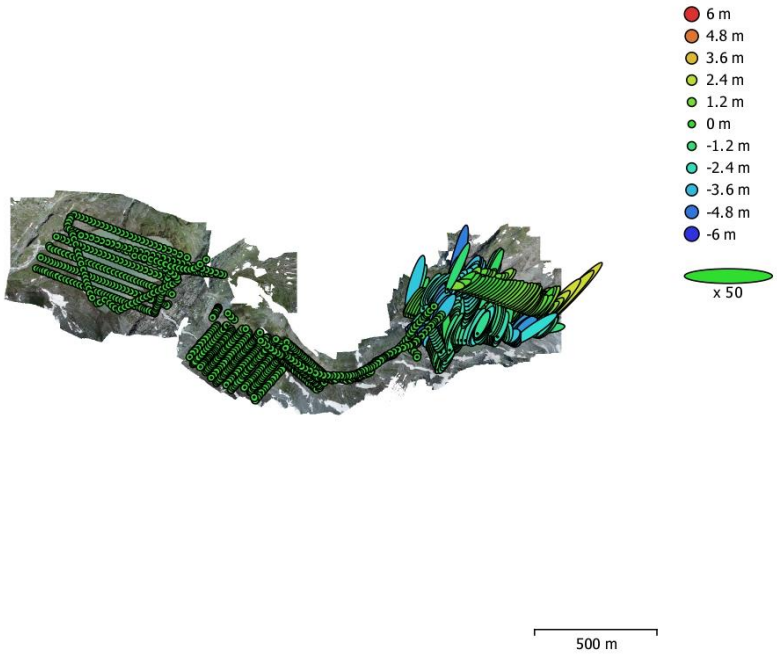

Fig. 3. Camera locations and error estimates.
Z error is represented by ellipse color. X,Y errors are represented by ellipse shape.
Estimated camera locations are marked with a black dot.

X error (m)	Y error (m)	Z error (m)	XY error (m)	Total error (m)
0.666762	0.943467	1.12531	1.15529	1.61277

Table 3. Average camera location error.
X - Longitude, Y - Latitude, Z - Altitude.

Ground Control Points

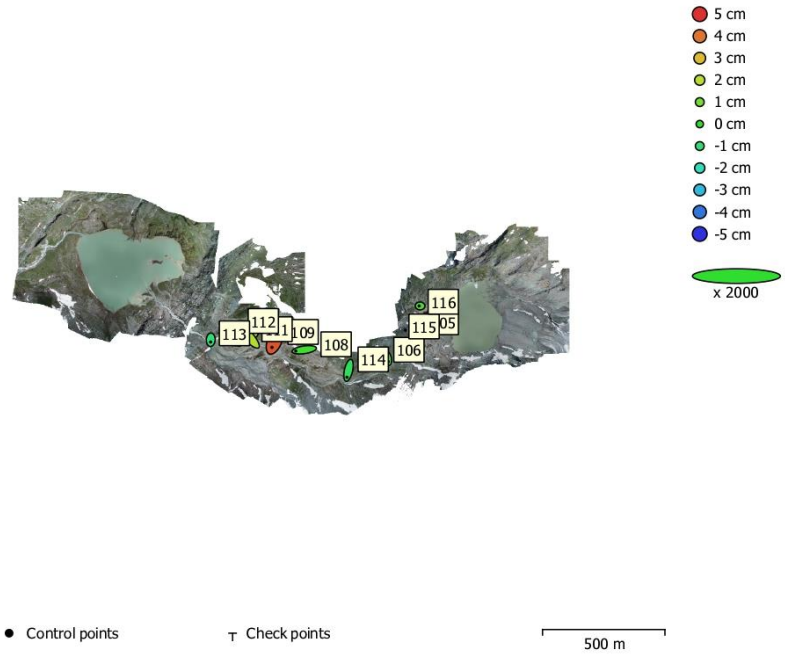

Fig. 4. GCP locations and error estimates.
Z error is represented by ellipse color. X,Y errors are represented by ellipse shape.
Estimated GCP locations are marked with a dot or crossing.

Count	X error (cm)	Y error (cm)	Z error (cm)	XY error (cm)	Total (cm)
9	1.67581	1.84923	1.78675	2.4956	3.06928

Table 4. Control points RMSE.
X - Longitude, Y - Latitude, Z - Altitude.

Label	X error (cm)	Y error (cm)	Z error (cm)	Total (cm)	Image (pix)
105	-0.0456315	-0.460755	-0.783816	0.910354	0.611 (16)
106	0.395462	-1.47998	0.337428	1.56862	0.561 (10)
108	-3.43692	-0.493061	0.218514	3.47897	0.618 (47)
109	-0.962022	-2.29062	4.493	5.13415	0.790 (28)
111	-0.556462	-0.221177	1.63084	1.7373	1.039 (15)
112	-3.39307	3.72103	1.88147	5.37577	1.161 (14)
113	-0.0498941	-0.92325	-1.04523	1.39549	0.621 (16)
114	-0.639871	-2.85249	-0.596873	2.98369	0.509 (28)
115					
116	-0.379914	0.0136704	0.34788	0.515307	0.667 (6)
Total	**1.67581**	**1.84923**	**1.78675**	**3.06928**	**0.729**

Table 5. Control points.
X - Longitude, Y - Latitude, Z - Altitude.

Digital Elevation Model

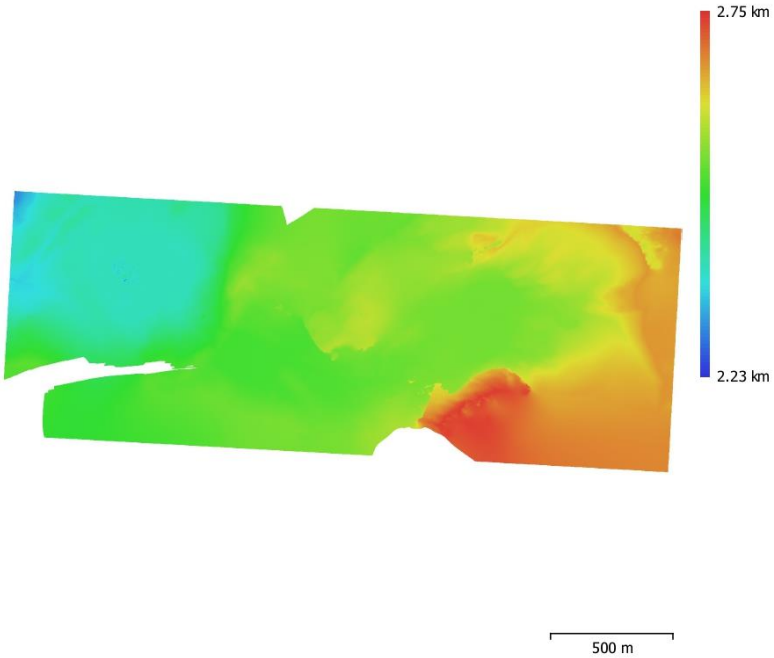

Fig. 5. Reconstructed digital elevation model.

Resolution:	5.61 cm/pix
Point density:	318 points/m²

Processing Parameters

General	
Cameras	1480
Aligned cameras	1466
Markers	12
Coordinate system	RDN2008 (EPSG::6706)
Rotation angles	Yaw, Pitch, Roll
Point Cloud	
Points	13,542,470 of 14,201,262
RMS reprojection error	0.150144 (0.627295 pix)
Max reprojection error	0.546917 (46.8481 pix)
Mean key point size	3.76862 pix
Point colors	3 bands, uint8
Key points	No
Average tie point multiplicity	4.1597
Alignment parameters	
Accuracy	High
Generic preselection	Yes
Reference preselection	Source
Key point limit	0
Tie point limit	0
Guided image matching	No
Adaptive camera model fitting	No
Matching time	31 minutes 33 seconds
Matching memory usage	2.75 GB
Alignment time	1 hours 31 minutes
Alignment memory usage	5.28 GB
Optimization parameters	
Parameters	f, cx, cy, k1-k3, p1, p2
Adaptive camera model fitting	No
Optimization time	3 minutes 18 seconds
Date created	2021:12:09 14:16:03
Software version	1.6.5.11249
File size	1.22 GB
Depth Maps	
Count	1462
Depth maps generation parameters	
Quality	High
Filtering mode	Mild
Processing time	3 hours 52 minutes
Memory usage	6.55 GB
Date created	2021:12:09 19:59:09
Software version	1.6.5.11249
File size	7.15 GB
Dense Point Cloud	
Points	523,331,228
Point colors	3 bands, uint8
Depth maps generation parameters	
Quality	High
Filtering mode	Mild
Processing time	3 hours 52 minutes

Memory usage	6.55 GB
Dense cloud generation parameters	
Processing time	4 hours 9 minutes
Memory usage	18.05 GB
Date created	2021:12:10 00:08:55
Software version	1.6.5.11249
File size	7.43 GB
Model	
Faces	104,476,868
Vertices	52,246,393
Vertex colors	3 bands, uint8
Depth maps generation parameters	
Quality	High
Filtering mode	Mild
Processing time	3 hours 52 minutes
Memory usage	6.55 GB
Reconstruction parameters	
Surface type	Height field
Source data	Dense cloud
Interpolation	Enabled
Strict volumetric masks	No
Processing time	47 minutes 43 seconds
Memory usage	17.09 GB
Date created	2021:12:10 00:08:58
Software version	1.6.5.11249
File size	2.34 GB
DEM	
Size	49,628 x 20,474
Coordinate system	RDN2008 (EPSG::6706)
Reconstruction parameters	
Source data	Dense cloud
Interpolation	Enabled
Processing time	6 minutes 34 seconds
Memory usage	336.33 MB
Date created	2021:12:10 04:23:47
Software version	1.6.5.11249
File size	2.65 GB
Orthomosaic	
Size	98,716 x 40,930
Coordinate system	RDN2008 (EPSG::6706)
Colors	3 bands, uint8
Reconstruction parameters	
Blending mode	Mosaic
Surface	Mesh
Enable hole filling	Yes
Processing time	3 hours 20 minutes
Memory usage	13.35 GB
Date created	2021:12:10 03:57:33
Software version	1.6.5.11249
File size	33.80 GB
System	
Software name	Agisoft Metashape Professional
Software version	1.7.4 build 13028
OS	Windows 64 bit
RAM	63.68 GB
CPU	Intel(R) Core(TM) i9-9900X CPU @ 3.50GHz

Report Rutor2023_MULTI_LagoMarginale

Processing Report
08 August 2023

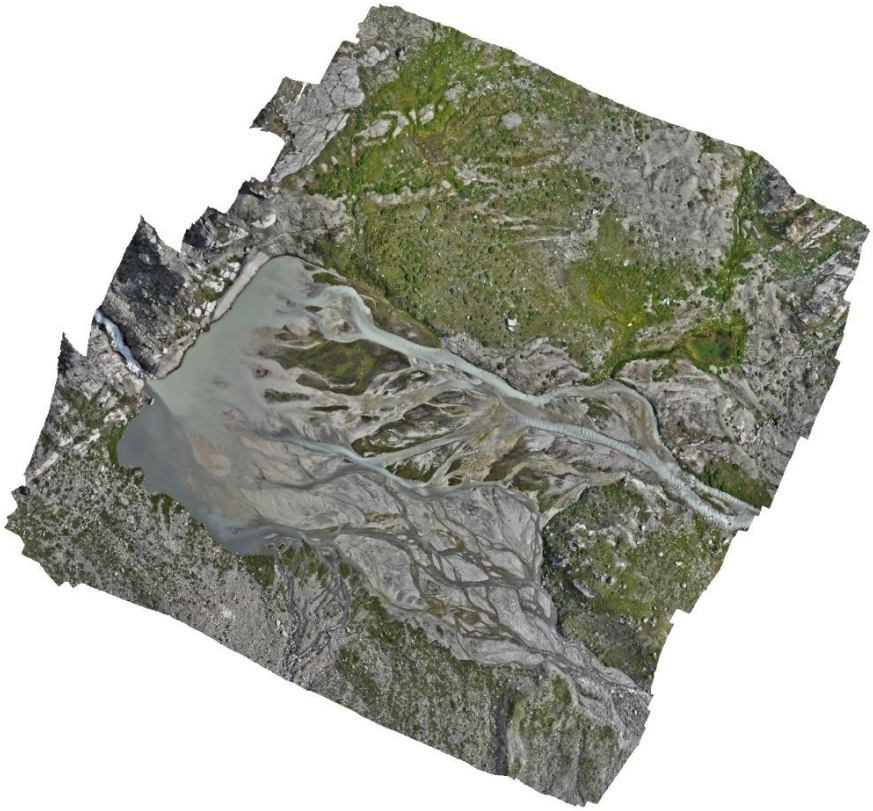

Survey Data

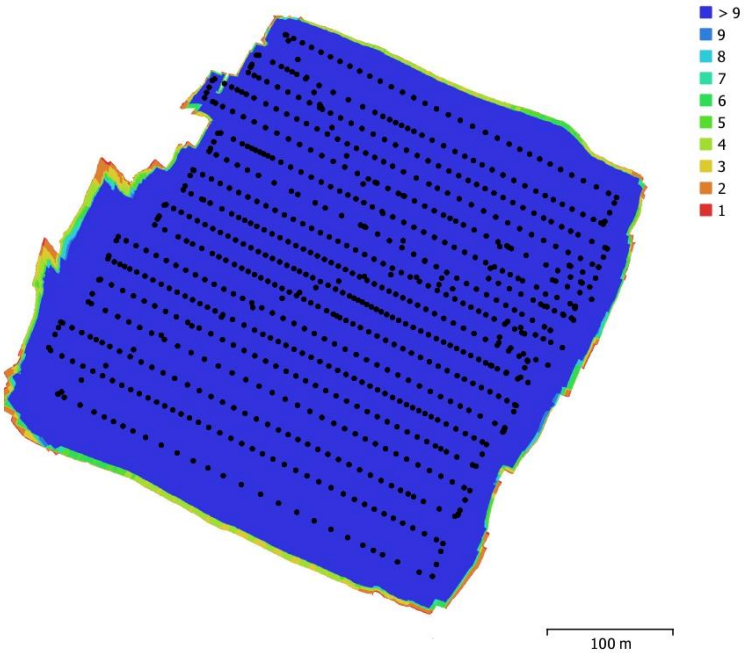

Fig. 1. Camera locations and image overlap.

Number of images:	4,220	Camera stations:	4,220
Flying altitude:	58.7 m	Tie points:	447,804
Ground resolution:	1.54 cm/pix	Projections:	3,151,559
Coverage area:	0.152 km²	Reprojection error:	1.78 pix

Camera Model	Resolution	Focal Length	Pixel Size	Precalibrated
M3M (12.29mm)	5280 x 3956	12.29 mm	3.36 x 3.36 µm	No
M3M (4.34mm)	2592 x 1944	4.34 mm	2 x 2 µm	Yes
M3M (4.34mm)	2592 x 1944	4.34 mm	2 x 2 µm	Yes
M3M (4.34mm)	2592 x 1944	4.34 mm	2 x 2 µm	Yes
M3M (4.34mm)	2592 x 1944	4.34 mm	2 x 2 µm	Yes

Table 1. Cameras.

Camera Calibration

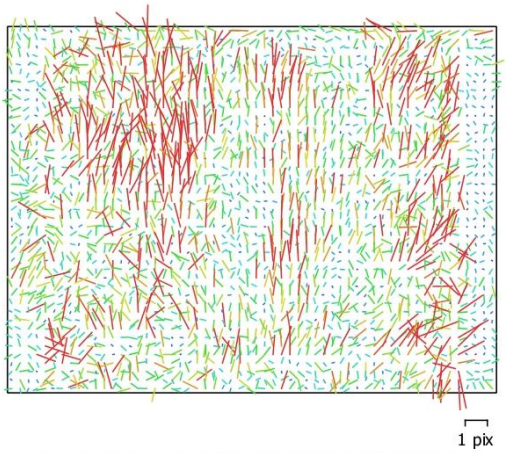

Fig. 2. Image residuals for M3M (12.29mm).

M3M (12.29mm)

844 images, additional corrections

Type	Resolution	Focal Length	Pixel Size
Frame	**5280 x 3956**	**12.29 mm**	**3.36 x 3.36 µm**

	Value	Error	F	Cx	Cy	K1	K2	K3	P1	P2
F	**3822.26**	1.1	1.00	0.00	-0.06	-0.76	0.76	-0.74	0.04	-0.05
Cx	**19.7138**	0.69		1.00	-0.05	-0.03	0.03	-0.03	0.97	-0.05
Cy	**-72.351**	0.88			1.00	-0.01	0.03	-0.05	-0.06	1.00
K1	**-0.0536805**	0.0014				1.00	-0.99	0.97	-0.05	-0.02
K2	**0.148702**	0.0027					1.00	-0.99	0.05	0.05
K3	**-0.0970995**	0.0018						1.00	-0.05	-0.07
P1	**-0.00171568**	0.00011							1.00	-0.07
P2	**-0.0048002**	0.00014								1.00

Table 2. Calibration coefficients and correlation matrix.

Camera Calibration

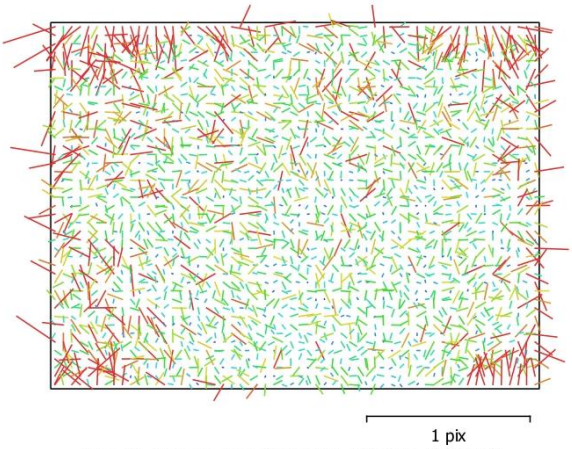

Fig. 3. Image residuals for M3M (4.34mm).

M3M (4.34mm)

844 images, precalibrated, additional corrections

Type	Resolution	Focal Length	Pixel Size
Frame	**2592 x 1944**	**4.34 mm**	**2 x 2 µm**

	Value	Error	F	Cx	Cy	K1	K2	K3	P1	P2
F	**2221.43**	0.5	1.00	-0.04	0.03	-0.57	0.55	-0.55	-0.02	-0.01
Cx	**16.0671**	0.21		1.00	0.01	0.04	-0.04	0.04	0.97	0.01
Cy	**9.96534**	0.22			1.00	0.02	-0.02	0.03	0.01	0.98
K1	**0.0176506**	0.0012				1.00	-1.00	0.98	0.05	0.02
K2	**-0.07417**	0.0036					1.00	-1.00	-0.05	-0.03
K3	**0.0120392**	0.0035						1.00	0.05	0.03
P1	**0.00086645**	4.3e-05							1.00	0.01
P2	**0.000288967**	4.7e-05								1.00

Table 3. Calibration coefficients and correlation matrix.

Camera Calibration

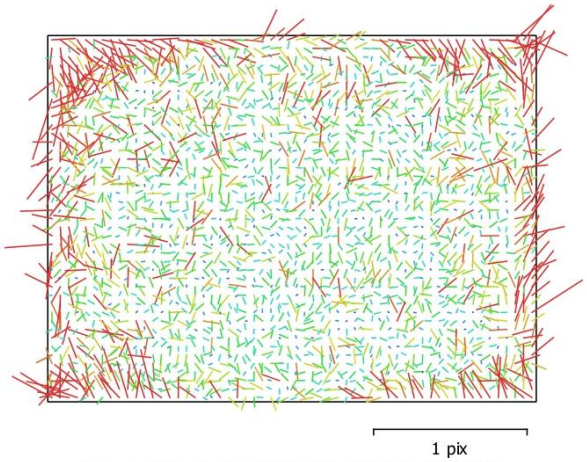

Fig. 4. Image residuals for M3M (4.34mm).

M3M (4.34mm)

844 images, precalibrated, additional corrections

Type	Resolution	Focal Length	Pixel Size
Frame	**2592 x 1944**	**4.34 mm**	**2 x 2 µm**

	Value	Error	F	Cx	Cy	K1	K2	K3	P1	P2
F	**2223.81**	0.51	1.00	-0.05	0.03	-0.59	0.58	-0.58	-0.04	-0.00
Cx	**27.0834**	0.22		1.00	0.02	0.07	-0.06	0.06	0.97	0.02
Cy	**-19.4451**	0.24			1.00	-0.02	0.03	-0.04	0.03	0.98
K1	**0.012235**	0.0013				1.00	-1.00	0.98	0.07	-0.02
K2	**-0.0631033**	0.0039					1.00	-1.00	-0.07	0.03
K3	**0.00161359**	0.0037						1.00	0.07	-0.04
P1	**0.00103384**	4.6e-05							1.00	0.03
P2	**-0.000175821**	5e-05								1.00

Table 4. Calibration coefficients and correlation matrix.

Camera Calibration

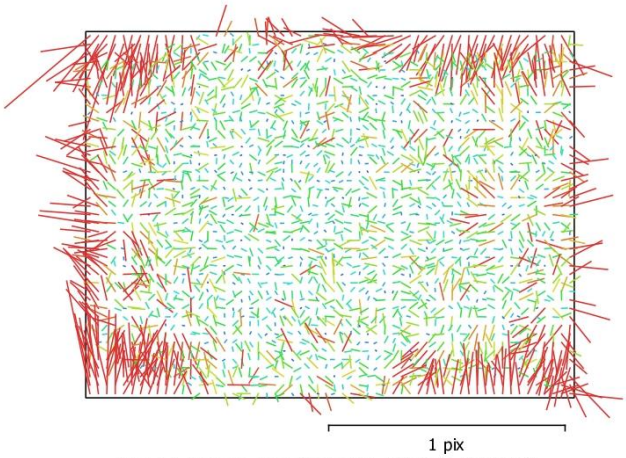

Fig. 5. Image residuals for M3M (4.34mm).

M3M (4.34mm)

844 images, precalibrated, additional corrections

Type	Resolution	Focal Length	Pixel Size
Frame	**2592 x 1944**	**4.34 mm**	**2 x 2 µm**

	Value	Error	F	Cx	Cy	K1	K2	K3	P1	P2
F	**2230.82**	0.45	1.00	-0.03	0.07	-0.39	0.37	-0.38	0.02	-0.02
Cx	**-14.71**	0.14		1.00	0.00	-0.03	0.03	-0.03	0.96	0.01
Cy	**7.40466**	0.14			1.00	0.03	-0.03	0.04	0.01	0.95
K1	**0.0123977**	0.00076				1.00	-0.99	0.98	-0.03	0.03
K2	**-0.0731137**	0.0023					1.00	-1.00	0.03	-0.03
K3	**0.0162117**	0.0022						1.00	-0.04	0.04
P1	**-0.000703071**	2.8e-05							1.00	0.01
P2	**1.79669e-05**	2.9e-05								1.00

Table 5. Calibration coefficients and correlation matrix.

Camera Calibration

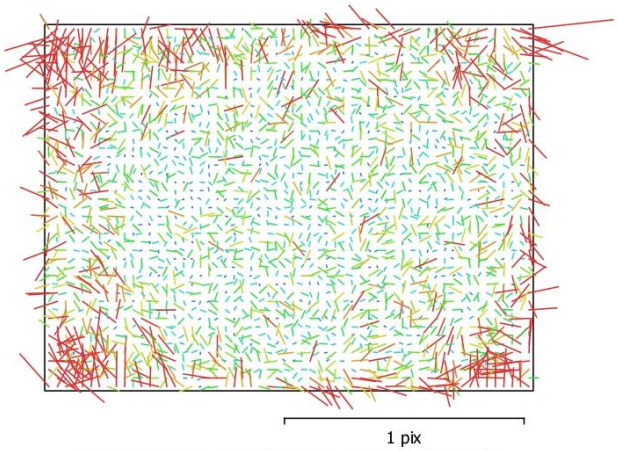

Fig. 6. Image residuals for M3M (4.34mm).

M3M (4.34mm)

844 images, precalibrated, additional corrections

Type	Resolution	Focal Length	Pixel Size
Frame	**2592 x 1944**	**4.34 mm**	**2 x 2 µm**

	Value	Error	F	Cx	Cy	K1	K2	K3	P1	P2
F	**2235.05**	0.45	1.00	-0.04	0.07	-0.40	0.38	-0.38	0.02	-0.01
Cx	**-7.57488**	0.14		1.00	-0.01	-0.01	0.02	-0.02	0.96	0.00
Cy	**-10.9712**	0.15			1.00	-0.00	0.00	-0.01	0.00	0.96
K1	**0.0203366**	0.00078				1.00	-0.99	0.98	-0.01	-0.00
K2	**-0.086766**	0.0024					1.00	-1.00	0.01	0.01
K3	**0.0289923**	0.0023						1.00	-0.02	-0.01
P1	**0.000883512**	3e-05							1.00	0.01
P2	**0.000366134**	3.1e-05								1.00

Table 6. Calibration coefficients and correlation matrix.

Camera Locations

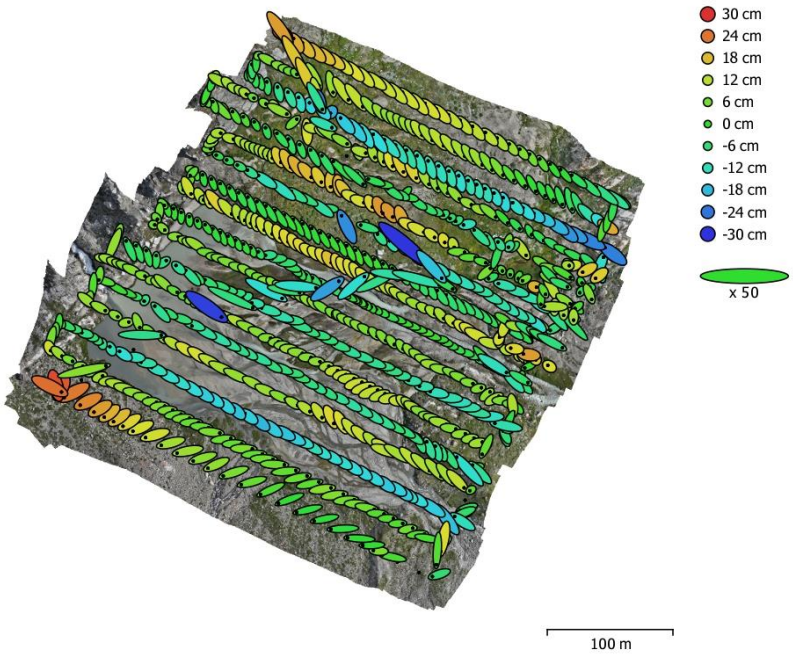

Fig. 7. Camera locations and error estimates.
Z error is represented by ellipse color. X,Y errors are represented by ellipse shape.
Estimated camera locations are marked with a black dot.

X error (cm)	Y error (cm)	Z error (cm)	XY error (cm)	Total error (cm)
16.5316	13.3876	9.96172	21.2726	23.4895

Table 7. Average camera location error.
X - Easting, Y - Northing, Z - Altitude.

Ground Control Points

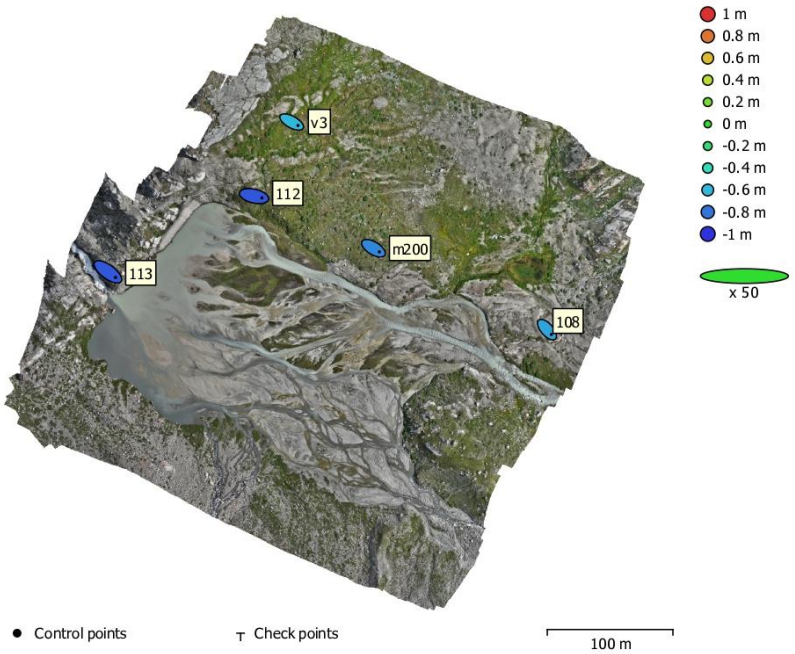

Fig. 8. GCP locations and error estimates.
Z error is represented by ellipse color. X,Y errors are represented by ellipse shape.
Estimated GCP locations are marked with a dot or crossing.

Count	X error (cm)	Y error (cm)	Z error (cm)	XY error (cm)	Total (cm)
5	20.7933	12.9964	76.6303	24.5208	80.4579

Table 8. Control points RMSE.
X - Easting, Y - Northing, Z - Altitude.

Label	X error (cm)	Y error (cm)	Z error (cm)	Total (cm)	Image (pix)
108	13.7094	-15.5039	-66.1734	69.3343	7.272 (5)
m200	18.8963	-11.4352	-74.4473	77.6546	6.160 (5)
v3	20.1124	-10.9951	-60.5209	64.7161	15.610 (10)
112	24.9808	-5.64896	-88.896	92.5119	12.769 (12)
113	24.2538	-17.9052	-88.7377	93.7188	11.261 (8)
Total	**20.7933**	**12.9964**	**76.6303**	**80.4579**	**12.106**

Table 9. Control points.
X - Easting, Y - Northing, Z - Altitude.

Digital Elevation Model

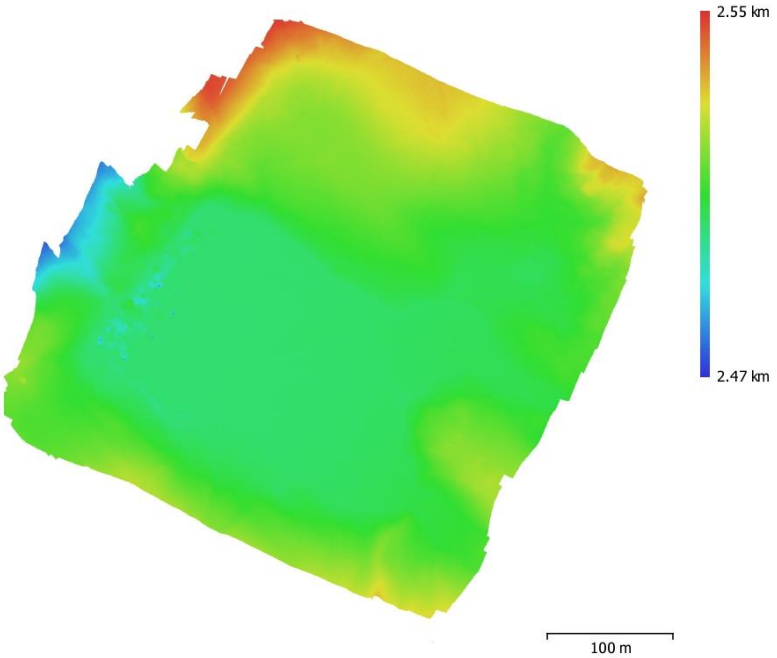

Fig. 9. Reconstructed digital elevation model.

Resolution:	2.51 cm/pix
Point density:	0.158 points/cm²

Processing Parameters

General	
Cameras	4220
Aligned cameras	4220
Markers	5
Coordinate system	RDN2008 / UTM zone 32N (N-E) (EPSG::6707)
Rotation angles	Yaw, Pitch, Roll
Point Cloud	
Points	447,804 of 1,876,333
RMS reprojection error	0.533705 (1.78344 pix)
Max reprojection error	4.54469 (90.3777 pix)
Mean key point size	2.03418 pix
Point colors	1 bands, uint8
Key points	No
Average tie point multiplicity	25.9785
Alignment parameters	
Accuracy	High
Generic preselection	Yes
Reference preselection	Source
Key point limit	80,000
Key point limit per Mpx	80,000
Tie point limit	8,000
Exclude stationary tie points	No
Guided image matching	Yes
Adaptive camera model fitting	No
Matching time	23 hours 19 minutes
Matching memory usage	21.46 GB
Alignment time	2 hours 2 minutes
Alignment memory usage	3.39 GB
Optimization parameters	
Parameters	f, cx, cy, k1-k3, p1, p2
Fit additional corrections	Yes
Adaptive camera model fitting	No
Optimization time	7 minutes 17 seconds
Date created	2023:08:05 09:09:19
Software version	1.8.5.15709
File size	756.37 MB
DEM	
Size	21,456 x 19,733
Coordinate system	RDN2008 / UTM zone 32N (N-E) (EPSG::6707)
File size	667.72 MB
Orthomosaic	
Size	10,788 x 9,921
Coordinate system	RDN2008 / UTM zone 32N (N-E) (EPSG::6707)
Colors	7 bands, uint16
Reconstruction parameters	
Blending mode	Mosaic
Surface	DEM
Enable hole filling	Yes
Enable ghosting filter	No
Processing time	1 hours 22 minutes

Memory usage	2.53 GB
Date created	2023:08:08 11:50:41
Software version	1.8.3.14331
File size	23.00 GB
System	
Software name	Agisoft Metashape Professional
Software version	1.8.3 build 14331
OS	Windows 64 bit
RAM	63.68 GB
CPU	Intel(R) Core(TM) i9-9900X CPU @ 3.50GHz
GPU(s)	Quadro RTX 4000